Radar Cross Section Reduction Using Electromagnetic Band-Gap Checkerboard Surfaces

by

Wengang Chen

A Dissertation Presented in Partial Fulfillment
of the Requirements for the Degree
Doctor of Philosophy

Approved November 2016 by the
Graduate Supervisory Committee:

Constantine A. Balanis, Chair
James T. Aberle
Hongbin Yu
Joseph C. Palais

ARIZONA STATE UNIVERSITY

December 2016

ABSTRACT

Electromagnetic band-gap (EBG) structures have noteworthy electromagnetic characteristics that include their phase variations with frequency. When combining perfect electric conductor (PEC) and EBG structures on the same ground plane, the scattering fields of the ground plane are altered because of the scattering properties of EBG structures. The scattering fields are cancelled along the principal planes because PEC and EBG structures are anti-phase at the resonant frequency. To make the scattered fields symmetrical under plane wave incidence, a square checkerboard surface is designed to form constructive and destructive interference scattering patterns to reduce the intensity of the scattered fields toward the observer; thus reducing the radar cross section (RCS). To increase the 10-dB RCS reduction (compared to a PEC surface) bandwidth, checkerboard surfaces of two different EBG structures on the same ground plane are designed. Thus, significant RCS reduction over a wider frequency bandwidth of about 63% is achieved.

Another design is a hexagonal checkerboard surface that achieves the same RCS reduction bandwidth because it combines the same EBG designs. The hexagonal checkerboard design further reduce the RCS than square checkerboard designs because the reflected energy is re-directed toward six directions and a null remains in the normal direction.

A dual frequency band checkerboard surface with 10-dB RCS reduction bandwidths of 61% and 24% is realized by utilizing two dual-band EBG structures, while the surfaces maintain scattering in four quadrants. The first RCS reduction bandwidth of the dual band is basically the same as in the square checkerboard design; however, the present surface exhibits a second frequency band of 10-dB RCS reduction.

Finally, cylindrically curved checkerboard surfaces are designed and examined for three different radii of curvature. Both narrow and wide band curved checkerboard surfaces are evaluated under normal incidence for both horizontal and vertical polarizations. Simulated bistatic RCS patterns of the cylindrical checkerboard surfaces are presented.

For all designs, bistatic and monostatic RCS of each checkerboard surface design are compared to that of the corresponding PEC surface. The monostatic simulations are also compared with measurements as a function of frequency and polarization. A very good agreement has been attained throughout.

To my wife, Ran

ACKNOWLEDGMENTS

I would like to express my gratitude to my advisor Prof. Constantine Balanis for his invaluable guidance throughout my studies. It has been an honor for me to have the opportunity to work with such a world-renowned professor. I believe that this will remain as one of the most important experiences of my life.

I also would like to thank to my committee members Prof. James Aberle, Prof. Hongbin Yu, and Prof. Joseph Palais for their helpful suggestions and constructive criticism.

It is a pleasure to acknowledge Craig Birtcher for his exceptional work and assistance to perform the measurements. I would not be at this point without his help. I have enjoyed the time when working with him and have learned a lot from him.

My special thanks go to my beloved wife for her continuing support and encouragement, and my family for their enormous understanding and patience. I would not be able to pursue my Ph.D. without their understanding, patience, and sacrifice.

In addition, I would like to thank to my labmates Ahmet Cemal Durgun, Alix Rivera-Albino, Nafati Aboserwal, Mikal Askarian-Amiri, Sivaseetharaman Pandi, Saud Saeed, Subramanian Ramalingam and Anuj Modi for the cheerful environment and joyful moments they shared with me.

I am also grateful to my friends who live in Arizona for being my family away from home. They have been extremely helpful and supportive in these years that I will never forget.

TABLE OF CONTENTS

CHAPTER Page

CHAPTER Page

LIST OF TABLES

LIST OF FIGURES

Figure Page

Figure Page

Figure Page

Figure Page

Figure Page

CHAPTER 1

INTRODUCTION

1.1. Background

EBG structures are synthesized surfaces that possesses unique characteristics [1–4]. They have emerged as one of the advances in modern antenna design. They have been extensively used in low-profile antenna designs because of their in-phase reflection characteristics in certain frequency band(s). The phase of the reflection coefficient of an EBG structure varies continuously from $+180^\circ$ to -180° as the frequency increases. An EBG structure is usually referred to as an artificial magnetic conductor (AMC) when the reflection phase is between $\pm 90^\circ$ [5]. This magnetic conductor property can be used as an alternative to a PEC ground plane [6–9]. However, a new research interest aims primarily at examining the application of EBG structures to alter the characteristics of scattered fields in order to reduce electromagnetic (EM) backscatter.

Two conventional methods to reduce the RCS of a structure is to change its shape so it redirects the scattered fields away from the observer, or to apply radar absorbing material (RAM) to absorb some of the power of the incident waves. Applying RAM on a surface is an efficient way to absorb incident waves to reduce the EM backscatter [10, 11]; RAM is lossy and forms an absorbent layer when applied to a surface [12–16]. A commonly used absorbing material is based on the Salisbury screen [12, 13]. The main advantages of applying RAM are convenience, flexibility and efficiency at the expense of overall thickness. Although the overall thickness can be reduced [14–16], the ground plane with RAM is frequency and angle sensitive, because most RAM is designed for a narrow frequency band [17, 18]. Re-directing the scattered fields is another efficient way to reduce

the RCS. In general, this is achieved by changing the shape of the target [19]. The drawback is the complexity of design.

A more recent alternate design to achieve the reduction of the RCS is to coat the radar target with checkerboard EBG designs of patches of different configurations [20–30]. Within its frequency band, the reflected fields from an EBG structure are in phase ($\pm 90^\circ$) with the incident fields, while those reflected from a PEC surface are 180° out of phase. This characteristic is used to alter the characteristics of the scattered fields without changing the shape of the underlying structure. Typically, checkerboard surfaces that combine PEC and EBG structures achieve a 10 dB RCS reduction (compared to a PEC surface) over a bandwidth of about 5% [20].

The incident waves on these checkerboard patches induce current densities whose amplitude and phase, especially the phase, are different as a function of frequency between the two sets of adjacent patch designs. These induced surface current densities act in a manner that is analogous to the elements of an antenna array. When the phases of these elements are judiciously designed, their re-radiated fields form constructive and destructive interference scattering patterns which reduce the intensity of the scattered fields toward the observer; thus reducing the RCS. Checkerboard surfaces with PEC and ideal PMC patches possess 180° phase difference between the scattered fields from adjacent checkerboard patches which result in cancellation of the scattered fields.

The main objective of this dissertation is to enhance the bandwidth of the RCS reduction of these checkerboard structures. This can be accomplished by replacing the PEC patches with patches comprised of a second EBG structure that is different from the first EBG

structure. For example, different sizes of square patches that resonate at two different frequencies were used in [21] and the bistatic RCS patterns of the resulting surface under normal incidence were simulated. In [22], two different sizes of Jerusalem Cross patches were used. The checkerboard surfaces that combine EBG structures with different sizes of patches realized bandwidths of about 40%. Although [24] and [25] consider checkerboard surfaces which have bandwidths of about 27% and 63%, respectively, only the simulated RCS under normal incidence of the surfaces are presented. The checkerboard surface in [26] has 10 dB RCS reductions over narrow bandwidths of 15%. While symmetric square-shaped checkerboard surfaces produce four redirected lobes of the bistatic scattered fields, a hexagonal design creates six redirected lobes, which further reduce the peak intensity of the redirected bistatic lobes. A wide bandwidth of up to about 63% has been realized by square and hexagonal checkerboard surface designs [27]. A dual frequency band checkerboard surface has been proposed in [28]. Although a fan-shape design increases the number of interfaces [29], the phase behavior does not apply very well in the normal direction.

Checkerboard surfaces have also recently been used at mm-waves [31], and as a part of low-profile antennas that result in low RCS [32–34], as well as gain enhancement [35]. With these benefits of low-profile and radiation improvement, conformal checkerboard surfaces can be an attractive technology for the design of conformal antennas [36–38]. In conformal applications, it is probable that checkerboard surfaces will be curved. As the radius of curvature decreases, the RCS reduction by checkerboard surfaces decreases compared to the corresponding curved PEC surfaces. This is evident for horizontal polarization (normal

to the axis of curvature) due to the presence and influence of array guided surface waves (AGSWs) [39]. However, for vertical polarization (parallel to the axis of curvature), the impact on RCS reduction is not as apparent because only Floquet currents exist [39].

1.2. Outline of the Dissertation

The remaining part of the dissertation is comprised of seven chapters.

In Chapter 2, conventional EBG structures, including their properties and analytical models are reviewed. The effects of parameters are briefly listed in this chapter. The performances of two examples of EBG structures are discussed at the end of this chapter.

Chapter 3 begins with the principle mechanism of checkerboard surfaces. Then, a semi-analytical method is developed for the characterization of checkerboard surfaces, including an expression that approximates the 10-dB RCS reduction of checkerboard surfaces compared to a PEC ground plane. Square checkerboard surfaces combining PEC and EBG structure, with and without vias, are simulated and compared with conventional PEC ground planes. Both normal incidence and oblique incidence are examined separately.

Chapter 4 extends checkerboard surfaces of PEC and EBG to checkerboard surfaces in which two different EBGs are combined. This combination realizes a wider frequency band for RCS reduction than the former. An expression that approximates the 10-dB RCS reduction is developed for this checkerboard surface. Both normal incidence and oblique incidence are also examined for this checkerboard surface. Also, the two different polarizations of oblique incidence are discussed in this chapter. The claims are verified with simulations and measurements.

A novel design of checkerboard surfaces is proposed in Chapter 5. Hexagonal checkerboard surfaces are designed to reduce the scattered fields more efficiently than square checkerboard surfaces. A hexagonal checkerboard surface is also simulated and measured for both normal incidence and oblique incidence. The simulation and measurement results prove that the expression also applies to this design of checkerboard surface.

Chapter 6 introduces a dual-frequency band checkerboard surface with two dual-band EBG structures. Given the reflection coefficients of the two EBGs, the expression can also predict the bandwidth of 10-dB RCS reduction. Both normal incidence and oblique incidence are simulated and measured for this checkerboard surface.

Cylindrically curved checkerboard surfaces are considered in Chapter 7. The RCS of cylindrical checkerboard surfaces are examined for three different radii of curvature. Both narrow and wide band curved checkerboard surfaces are evaluated under normal incidence for horizontal and vertical polarizations.

Finally in Chapter 8, all of the work performed during this study is summarized. The advantages and disadvantages of the methods and the structures suggested in this project are discussed, and concluding remarks are stated.

CHAPTER 2

EBG STRUCTURES

In this chapter the basic analysis and properties of EBG structures are introduced. The parameters of a unit cell of an EBG structure (such as the patch width, the gap between the patches, the substrate thickness and the substrate permittivity) mainly affect its resonant frequency. The effects of each parameter are briefly listed. Two examples, EBG structures with square patches and circular patches, are simulated and explained at the end of this chapter.

2.1. Introduction

EBG structures have been studied over the last decade because of their unique electromagnetic properties which do not exist in natural materials: they behave as Artificial Magnetic Conductor (AMC). Basically, an EBG structure entails a number of periodic metal patches printed on one side of a dielectric substrate with a metal ground plane on the other side. Vertical vias, normally located at the center of each patch, connect the patches to the ground plane, as illustrated in Fig. 2.1. The most common shapes of patches are squares, circles, hexagons, etc. The period of patches is very small in terms of wavelength. The gap between the neighbor patches introduces capacitance. The inductance is induced between the patches and ground plane by the substrate. The properties of a unit cell of an EBG structure can be modelled as lumped elements. An LC circuit is a simple way to describe the EBG structure. The equivalent parallel LC circuit of an unit cell is illustrated in the Fig. 2.2.

The capacitance and inductance [42] are given by the following equation:

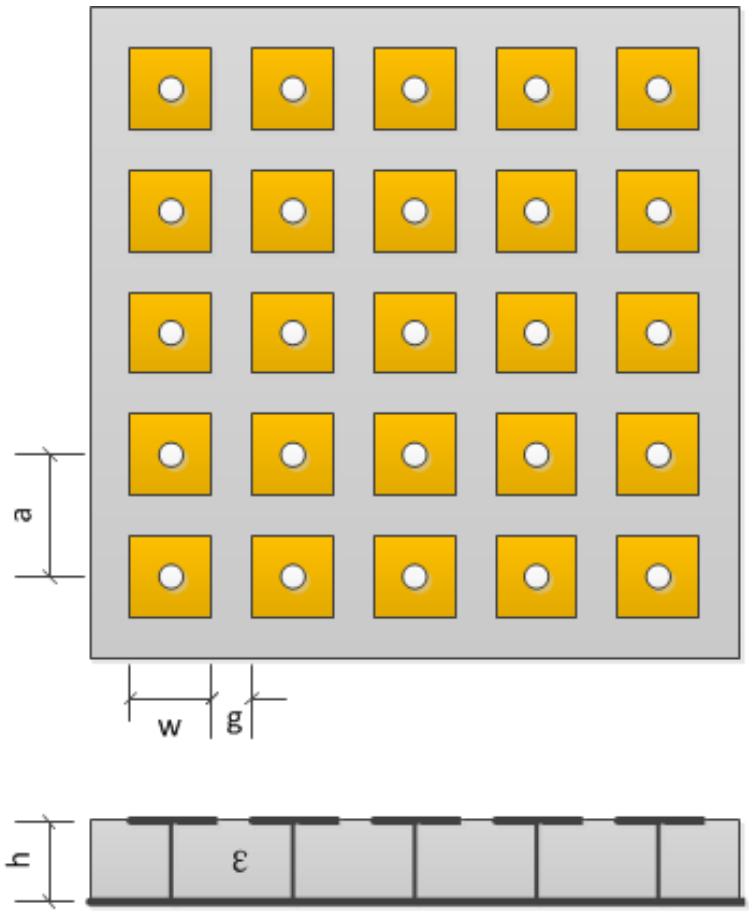

Fig. 2.1. EBG Structure with Square Patches.

$$C = \frac{w\varepsilon_0(1+\varepsilon_r)}{\pi}\cosh^{-1}\left(\frac{w+g}{g}\right) \tag{2.1}$$

$$L = \mu h \tag{2.2}$$

where w is the length of the patches, g is the gap between the neighbour patches, ε_r is the dielectric constant of the substrate, h is the thickness of the substrate.

The surface impedance is given by the following equation:

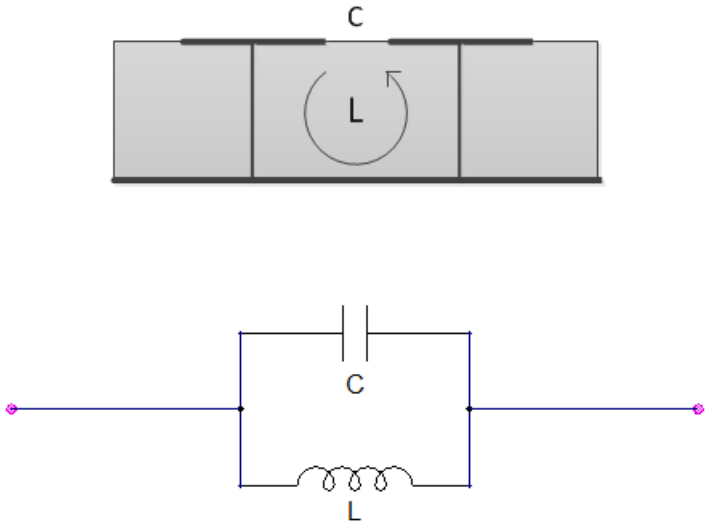

Fig. 2.2. Unit Cell of an EBG Structure and its Equivalent LC Circuit

$$Z_s = \frac{jwL}{1 - \omega^2 LC} \tag{2.3}$$

The resonant frequency is given by:

$$f_0 = \frac{1}{2\pi\sqrt{LC}} \tag{2.4}$$

The surface impedance is inductive below the resonant frequency. It supports TM surface waves.

$$Z_s^{TM} = \frac{j\alpha}{\omega\varepsilon} \tag{2.5}$$

The surface impedance is capacitive above the resonant frequency. It supports TE surface waves.

$$Z_s^{TE} = -\frac{j\omega\mu}{\alpha} \tag{2.6}$$

One of the important properties of an EBG structure is in-phase reflection, which means the phase of the reflection coefficient is 0° at the resonant frequency. The phase of the reflection coefficient is the phase difference between the reflected waves and the incident waves. Because the surface impedance varies as a function of frequency, the phase of the reflection coefficient also varies as a function of frequency. The phase of the reflection coefficient is also dependent on the incident waves. Different angles and polarizations of the incident waves result in different properties of the reflection phase. For oblique incidence, vias play a very important role in the EBG structure. Due to the presence of the vias, EBG structures exhibit the property of surface wave band gap which significantly affects the phase of the reflection coefficient. On the other hand, for normal incidence, the effect of the vias is negligible in terms of the reflection phase.

The surface impedance is equivalent to the parallel circuit of the capacitance within the gaps, $Z_{gap} = \frac{1}{j\omega C_g}$, and the inductance within the substrate, $Z_substrate = j\omega\mu h$.

$$Z_s = Z_{gap} \parallel Z_{substrate} = \frac{1}{j\omega C_g} \parallel j\omega\mu h \tag{2.7}$$

The surface impedance approaches zero at very low and high frequencies, so the reflection coefficient is -1, which has the same property as the PEC ground plane; the phase of the reflection coefficient is 180°. At the resonance frequency of the EBG structure, the surface impedance approaches infinity. This means the reflection coefficient is +1; the phase

of the reflection coefficient is 0°. From low frequency to resonance frequency, the surface wave is inductive; the phase varies from 180° to 0°. From resonance frequency to high frequency, the surface wave is capacitive; the phase varies from 0° to −180°. The range of the phase in ±90° is the so-called in-phase band gap. The reflection coefficient can be represented by a graph, which is illustrated in Fig. 2.3.

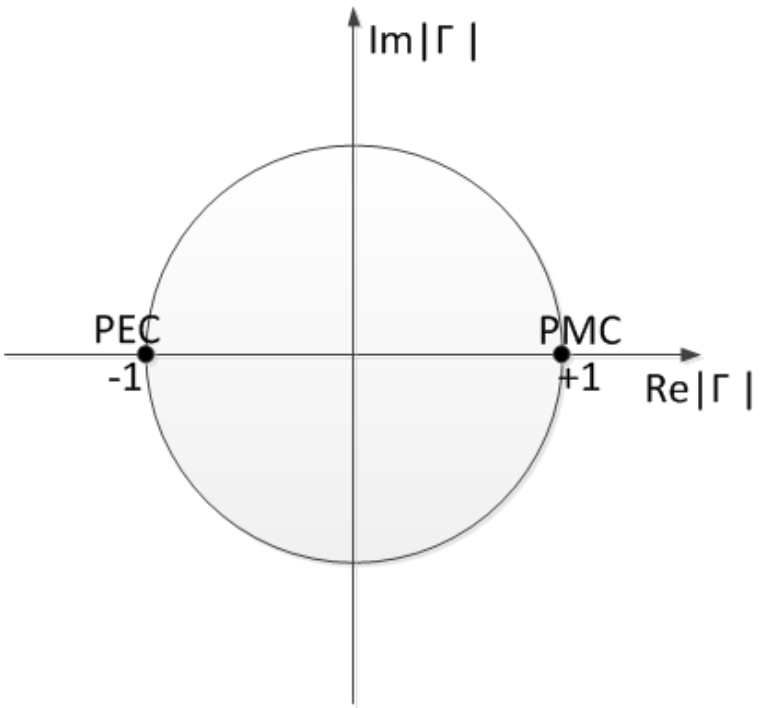

Fig. 2.3. Reflection Coefficient Circle

2.2. Parameters of an EBG Structure

The phase of the reflection coefficient can be controlled by adjusting the parameters of the EBG structure, such as the width of the patches (w), the gap between the patches (g), the thickness of the dielectric substrate (h), the dielectric constant of the substrate (ε_r) and the radius of the via (r). When the patch width (w) increases and the other param-

Parameters	Resonant Frequency	In-Phase Bandwidth
width (w) increases	f_0 decreases	BW decreases
gap (g) increases	f_0 increases	BW increases
thickness (h) increases	f_0 decreases	BW increases
dielectric constant (ε_r) increases	f_0 decreases	BW decreases
radius of the via (r) increases	Negligible	Negligible

Table 2.1. The Effects of the Parameters on the EBG Reflection Phase

eters remain fixed, the resonant frequency decreases and the slope of the curve near the resonant frequency becomes steep, which means a narrow bandwidth. When the patch gap (g) increases and the other parameters remain constant, the coupling between the patches decreases, so the resonant frequency increases and the bandwidth increases. When the substrate thickness (h) increases and the other parameters are unchanged, the inductance increases, so the resonant frequency decreases and the bandwidth increases. When the dielectric constant (ε_r) increases, the resonant frequency decreases and the bandwidth decreases. It can be observed that EBG cell size is reduced by using the substrate with a high dielectric constant. Although the effect of via radius (r) is negligible, the absence of via slightly decreases the resonant frequency. The effects on the phase of the reflection coefficient from adjusting the parameters of an EBG structure are listed in Table 2.1.

2.3. Modellings of EBG Structures

2.3.1. *EBG Structure with Square Patch*

The phase of the reflection coefficient is one of the noteworthy properties of an EBG structure, because the magnitude of the reflection coefficient of a ground plane will always be one (0 dB) for a lossless structure. In this section, EBG structures will be discussed and modelled using HFSS. The unit cell of the EBG structure with its square patch is illustrated in Fig. 2.4. By applying the proper boundary conditions, it can realize a periodic structure. The square metallic patch of the EBG structure with a width of 3.5 mm is located on the top surface of the substrate *RO*3006 with a thickness of 1.28 mm and a dielectric constant of 6.15. The bottom surface is metal. The gap between the patches is 0.5 mm. A pair of PEC boundary conditions are assigned on the front and rear walls, while another pair of PMC boundary conditions are assigned on the left and right walls, so that an infinite periodic EBG structure can be realized. The boundary conditions are dependant on the incident fields. The PEC boundary conditions should be perpendicular to the incident electric field, and the PMC boundary conditions should be perpendicular to the incidnet magnetic field. The simulation results of the unit cell are generated using HFSS and are illustrated in Fig. 2.5 and Fig. 2.6. The phase of the reflection coefficient of the unit cell varies from 180° to -180° as frequency increases. The reflection phase reaches 0° at the resonant frequency, which is 9.98 GHz. The magnitude of the reflection coefficient at the resonant frequency is -0.28 dB, which is attributed to the conductor loss, dielectric loss and radiation loss.

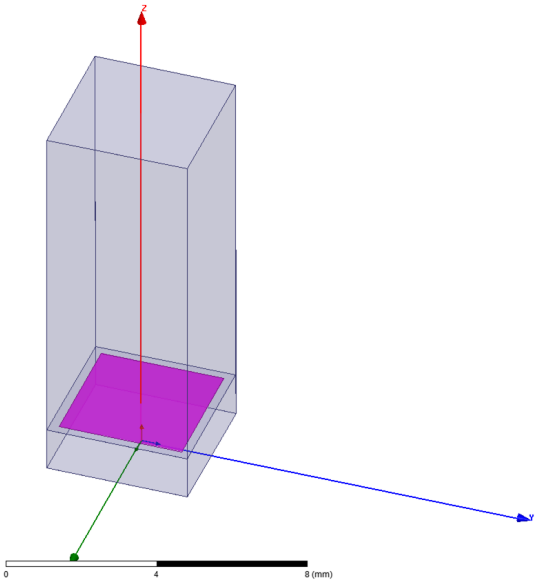

Fig. 2.4. Unit Cell of EBG structure with Square Patch

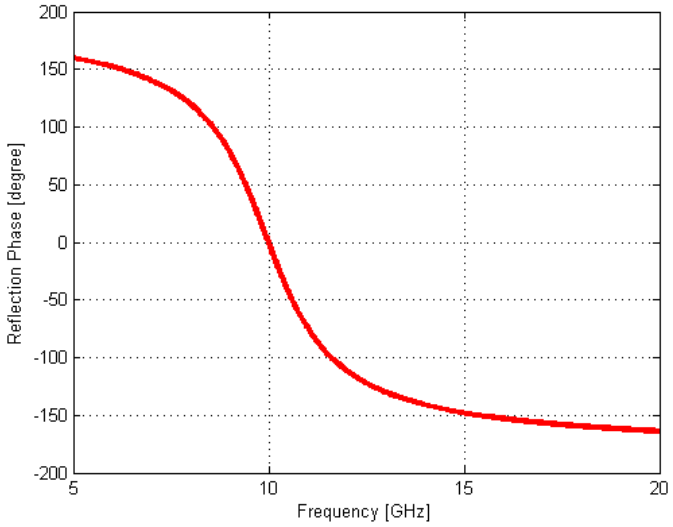

Fig. 2.5. Phase of Reflection Coefficient of the Unit Cell with Square Patch

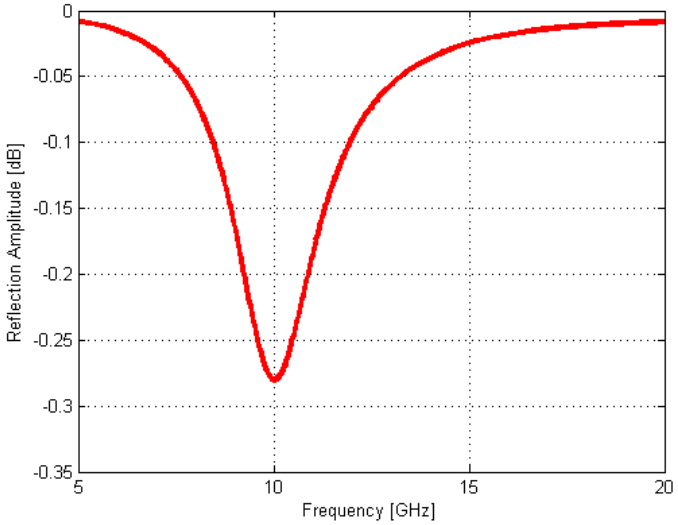

Fig. 2.6. Magnitude of Reflection Coefficient of the Unit Cell with Square Patch

2.3.2. *EBG Structure with Circular Patch*

Another popular patch shape for EBG structures is circular. The unit cell of the EBG structure with a cicular patch is illustrated in Fig. 2.7. By applying the proper boundary conditions, an infinite periodic structure can be simulated. The circular metallic patch of the EBG structure with its radius of 1.5 mm is located on the top surface of the substrate *RO*3006. The thickness is 1.28 mm and the dielectric constant is 6.15. The bottom surface is metal. The gap between the patches is 1.0 mm. The same boundary conditions as for the unit cell with the square patch are applied in this unit cell. The simulation results of the unit cell are also generated using HFSS and illustrated in Fig. 2.8 and Fig. 2.9. The phase of the reflection coefficient of the unit cell varies from 180° to -180° as frequency increases. The reflection phase reaches 0° at 14.76 GHz. The magnitude of the reflection coefficient at the resonant frequency is -0.14 dB, which is also attributed to the conductor, dielectric and radiation losses.

Although the diameter of the circular patch is slightly smaller than the width of the square patch, and the overall size of the square and circular unit cell and other parameters are the same, the resonant frequency of the unit cell with a circular patch is much higher than that of the unit cell with a square patch. This is due to the gap between the patches. The gap between the circular patch is not uniform and obviously larger than the gap between the square patch. This indicates that the capacitance between the patches is smaller. Thus, the resonant frequency is higher.

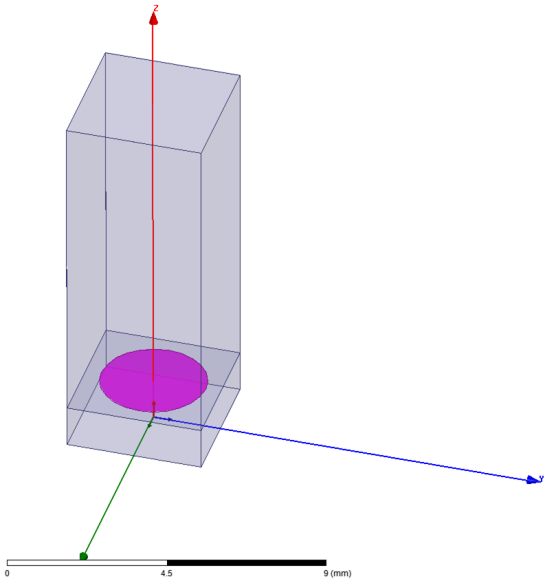

Fig. 2.7. Unit Cell of EBG Structure with Circular Patch

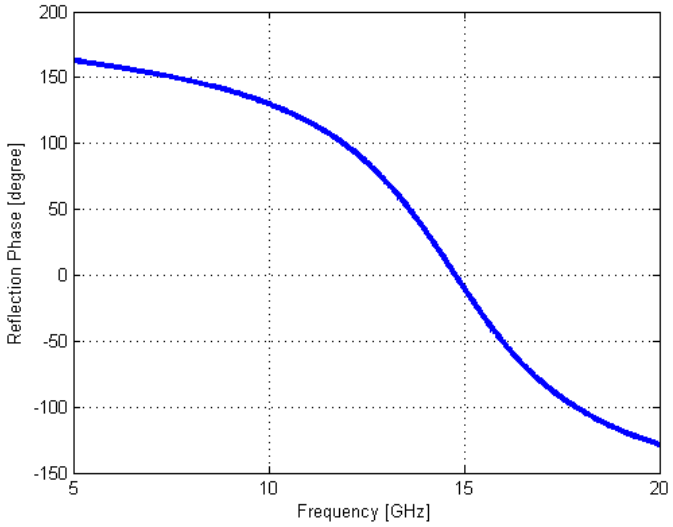

Fig. 2.8. Phase of Reflection Coefficient of the Unit Cell with Circular Patch

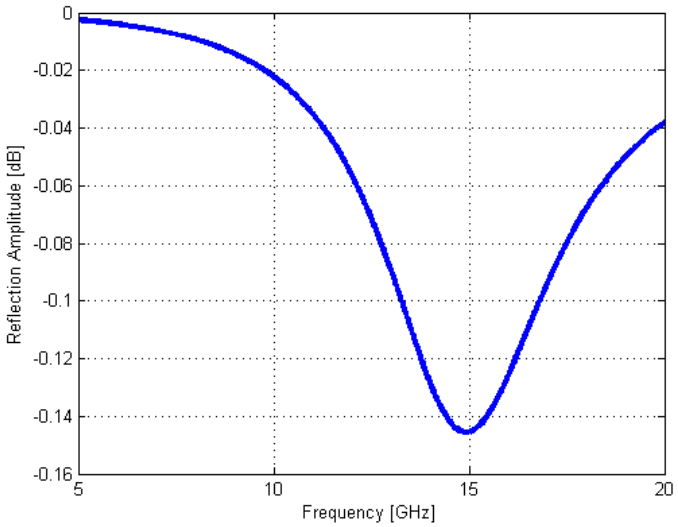

Fig. 2.9. Magnitude of Reflection Coefficient of the Unit Cell with Circular Patch

CHAPTER 3

NARROW BAND CHECKERBOARD SURFACES (PEC/EBG)

A basic narrow band checkerboard surface is analyzed and examined in this chapter. It begins with the principle mechanism of checkerboard surfaces, such as an expression that approximates the 10-dB RCS reduction of checkerboard surfaces. The checkerboard surfaces combining PEC and EBG structure, with and without vias, are simulated and compared with conventional PEC ground planes for both normal incidence and oblique incidence.

3.1. Introduction

It is well known that for PEC ground planes, the surface impedance is 0, the reflection coefficient is -1, and the phase of the reflection coefficient is 180°. For EBG ground plane at resonant frequency, the surface impedance is infinity, the reflection coefficient is +1, and the phase of the reflection coefficient is 0°. When the incident plane waves impinge on the PEC ground plane and on the EBG plane at resonance, individually, the phase difference of the reflected waves between both cases is 180°. When the PEC and EBG surfaces are combined on the same ground plane, the reflected fields cancel on another and the scattering pattern is altered from that of a uniform PEC ground plane.

3.2. Analysis of Checkerboard Surfaces

One of the important parameters in electromagnetic scattering is radar cross section (RCS). RCS is defined as *the area intercepting the amount of power that, when scattered isotropically, produces at the receiver a density that is equal to the density scattered by the actual target* [5].

The RCS can be represented as

$$\begin{aligned}\sigma_{3-D} &= \lim_{r\to\infty}\left[4\pi r^2\frac{|E^s|^2}{|E^i|^2}\right] \\ &= \lim_{r\to\infty}\left[4\pi r^2\frac{|H^s|^2}{|H^i|^2}\right]\end{aligned} \tag{3.1}$$

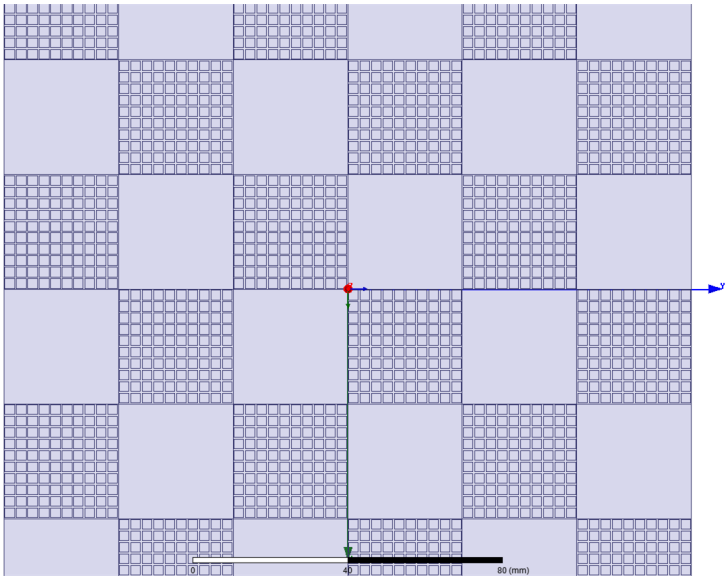

Fig. 3.1. Checkerboard Surface Combining PEC and EBG Structures

Fig. 3.1 illustrates that each period of the checkerboard surface consists of four elements: two PEC elements and two EBG structures. A checkerboard surface can be treated as a planar array with a progressive phase shift of 180°. For a large ground plane, the array factor [41] can be represented as

$$\begin{aligned}AF =& I_0 \cdot \sum_{m=1}^{M} e^{j(m-1)(kd_x\sin\theta\cos\phi+\beta_x)} \\ &\cdot \sum_{n=1}^{N} e^{j(n-1)(kd_y\sin\theta\sin\phi+\beta_y)}\end{aligned} \tag{3.2}$$

where β_x and β_y are the progressive phase shifts between the elements in the x- and y-directions, respectively. Both are about 180° out-of-phase at the resonant frequency. The distances d_x and d_y are the spacings between the elements along the x- and y-axis, respectively, while M and N are the number of elements in x- and y-directions, respectively.

The principal maximum can be located using Equation 3.3 and Equation 3.4.

$$\tan\phi_0 = \frac{\beta_y d_x}{\beta_x d_y} \tag{3.3}$$

$$\sin^2\theta_0 = \left(\frac{\beta_x}{kd_x}\right)^2 + \left(\frac{\beta_y}{kd_y}\right)^2 \tag{3.4}$$

The RCS reduction of the checkerboard surface compared to the RCS of the PEC ground plane can be approximated by Equation 3.5 and 3.6.

$$\begin{aligned}\text{RCS Reduction} &= 10\log\left[\frac{\lim\limits_{r\to\infty}\left[4\pi r^2\frac{|E^s|^2}{|E^i|^2}\right]}{\lim\limits_{r\to\infty}\left[4\pi r^2(1)^2\right]}\right] \\ &= 10\log\left[\frac{|E^s|^2}{|E^i|^2}\right]\end{aligned} \tag{3.5}$$

$$\text{RCS Reduction} = 10\log\left[\frac{-1+Ae^{jphase}}{2}\right]^2 \tag{3.6}$$

The RCS Reduction of Equation (3.6) is plotted as a function of EBG reflection phase in Fig. 3.2. This illustrates a key finding og this research, that an RCS reduction of 10-dB (or more) is achieved when the reflection phase of the EBG is within ±37°. Based on the EBG structure with and without vias, the RCS reduction as a function of frequency is

illustrated in Fig. 3.3 and Fig. 3.4, respectively. Although all the parameters are kept the same for both structures, excepting the absence of the vias, the resonant frequencies are slightly different. However, the RCS reduction behaviours for both cases remain the same, such as the bandwidth of 10-dB RCS reduction is 10.7%. The resonant frequencies are 12.5 GHz and 12.3 GHz for the checkerboard designs with and without vias, respectively.

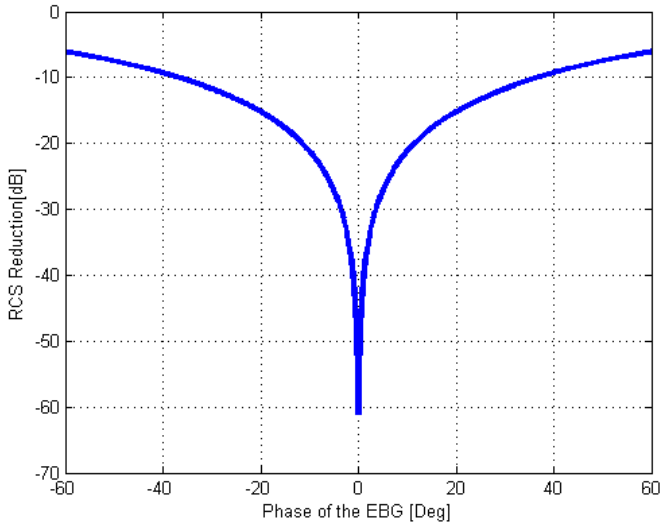

Fig. 3.2. RCS Reduction as a Function of the Reflection Phase of the EBG Structure

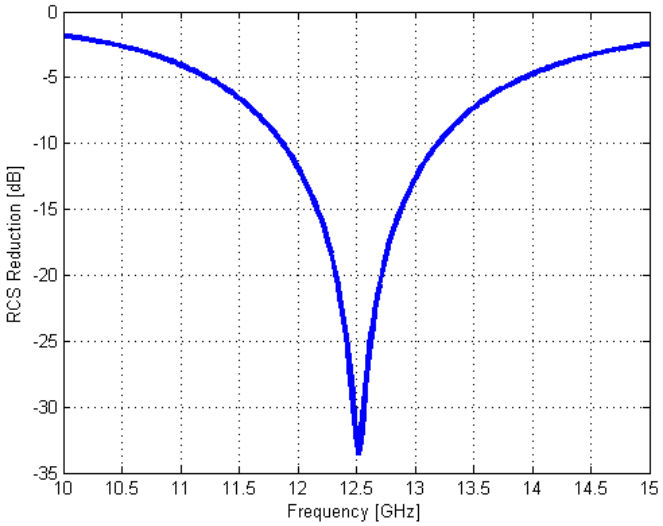

Fig. 3.3. RCS Reduction as a Function of Frequency for the Checkerboard Design with Vias

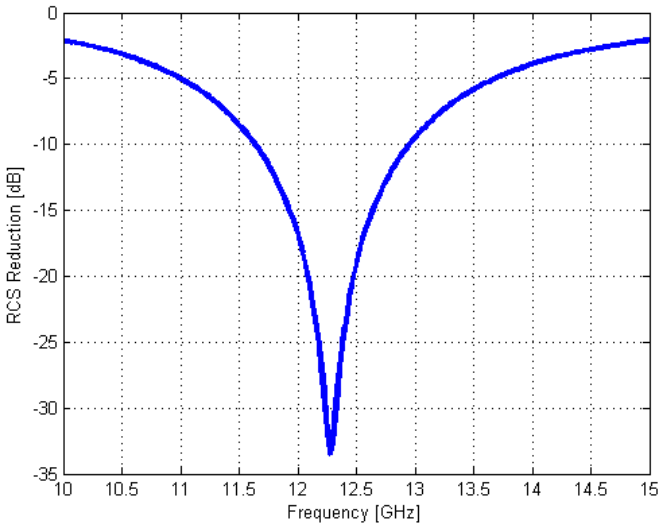

Fig. 3.4. RCS Reduction as a Function of Frequency for the Checkerboard Design without Vias

3.3. Normal Incidence

When normal incident waves impinge on a planar array, it can approximately be considered that the surface current that is induced on the surfaces is the same amplitude, but anti-phase, which means 180° phase difference.

3.3.1. *Conventional Ground Plane (PEC, EBG)*

Metal (PEC) ground plane is the most commonly used material for a ground plane. For a PEC ground plane, the tangential component of the E-field must vanish. For a PMC plane, the tangential component of the H-field must vanish. A PMC plane, does not exist in nature, can be realized with an EBG structure. Under normal incidence, the scattering patterns for the conventional ground planes are illustrated in Fig. 3.5 and Fig. 3.7, for a PEC ground plane and an EBG structure plane, respectively. The amplitude of the reflection coefficient of an EBG structure is about the same as that of a PEC ground plane. However, the phase of the reflection coefficient is 180° for a PEC ground plane while it varies from $+180°$ to $-180°$ for an EBG structure. Thus they are anti-phase at the resonant frequency, as illustrated in Fig. 3.6 and Fig. 3.8.

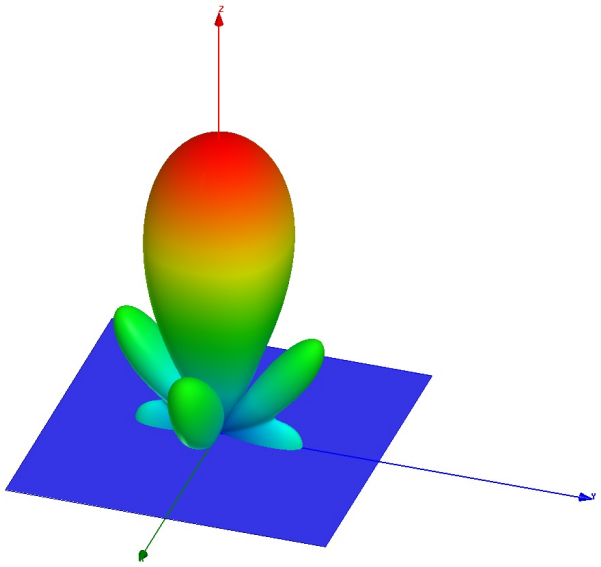

Fig. 3.5. Bistatic RCS Pattern for a PEC Ground Plane

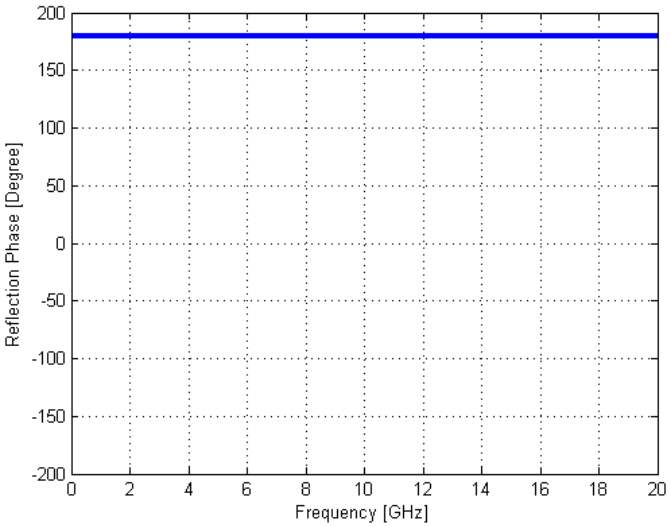

Fig. 3.6. Reflection Phase for a PEC Ground Plane

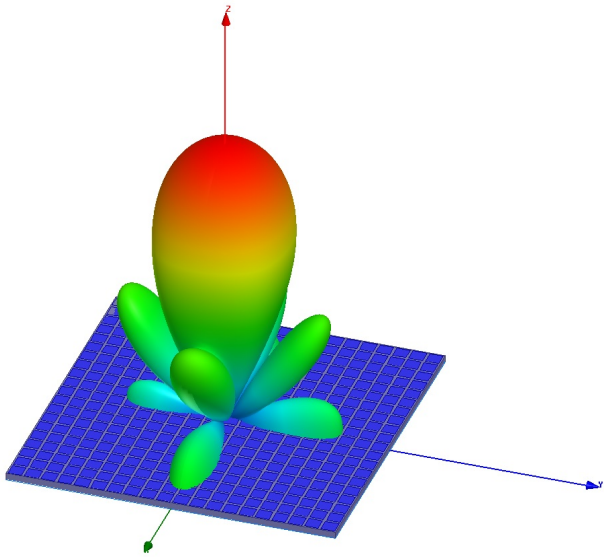

Fig. 3.7. Bistatic RCS Pattern for an EBG Structure Plane

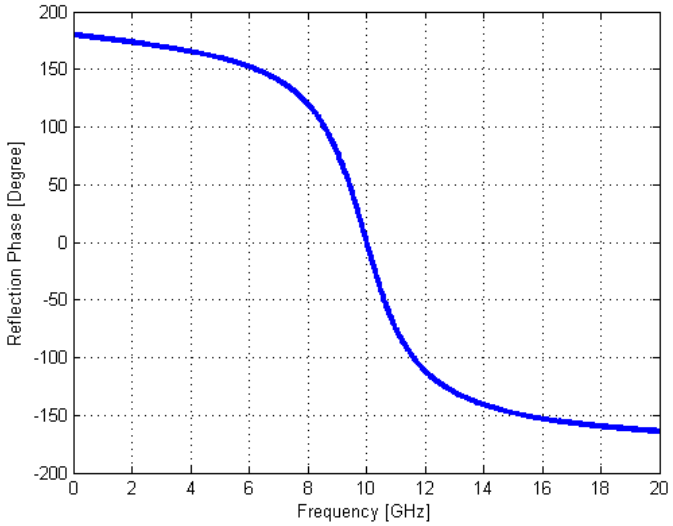

Fig. 3.8. Reflection Phase for an EBG Structure Plane

3.3.2. *Checkerboard Surface with Vias*

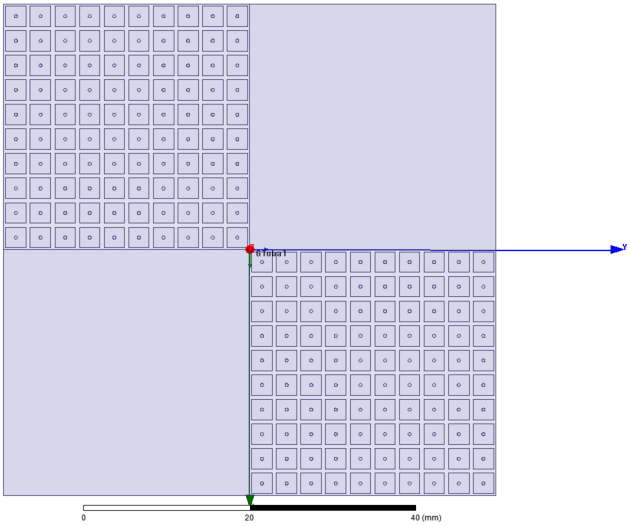

Fig. 3.9. Checkerboard Surface Combining PEC and EBG Structure with Vias

The checkerboard surface, as illustrated in Fig. 3.9, is designed and simulated with HFSS. The substrate used in the surface is Roger RO3006 for which the thickness is 1.28 mm and the dielectric constant is 6.15. Then the EBG structure is designed with a patch size of 2.5 mm x 2.5 mm, a gap between the patches of 0.5 mm and a radius of the via of 0.2 mm. It resonates at 12.5 GHz. To combine the PEC and EBG structure on the same ground plane, 10 x 10 unit cells are used for the EBG structures while the PEC uses a metallic surface. A checkerboard surface with 3 x 3 periods, placed on the XY plane, is simulated with HFSS. The overall dimension is 180 mm x 180 mm. Under normal incidence the solution frequency is swept from 9 GHz to 14 GHz. The monostatic RCS reduction at normal incidence, as a function of frequency, is illustrated in Fig. 3.10. This exhibits that the RCS is reduced for more than 10 dB within the frequency of 11.75 - 12.75 GHz. The

maximum reduction at 12.3 GHz is 16.4 dB. The resonant frequency is slightly shifted due to the effect of finite periodicity (e.g. the diffraction from the edges). The bandwidth is 8.2%.

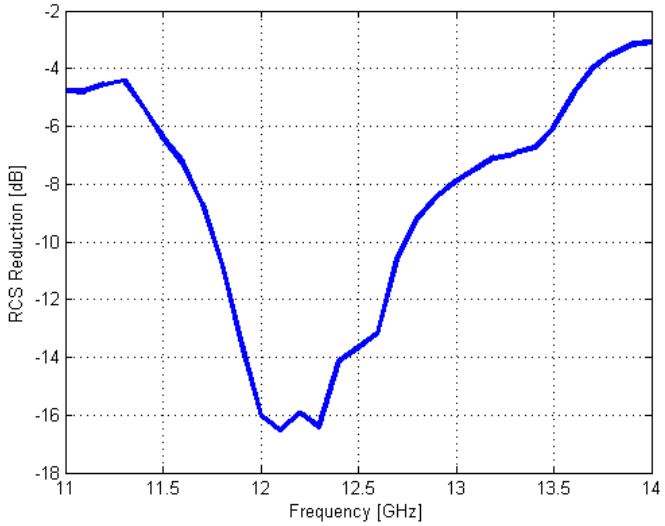

Fig. 3.10. Simulated Monostatic RCS Reduction as a Function of Frequency for the Checkerboard Surface with Vias

The bistatic RCS pattern at the resonance is illustrated in Fig. 3.11. When the normal incident waves impinge on the surface, which is located on the XY plane, the RCS is dramatically reduced in the principal planes (XZ and YZ planes). However, the main reflected lobes appear at the four quadrants, $\phi = 45°, 135°, 225°$ and $315°$.

The scattering fields in the $\phi = 0°$, $45°$, $90°$, $135°$, $180°$, $225°$, $270°$ and $315°$ planes as a function of theta are illustrated in Figs. 3.12 and 3.13, comparing the RCS for the checkerboard surface with the RCS for the PEC ground plane. As a reference, the PEC ground plane has its maximum scattering field in the normal direction, but the checkerboard

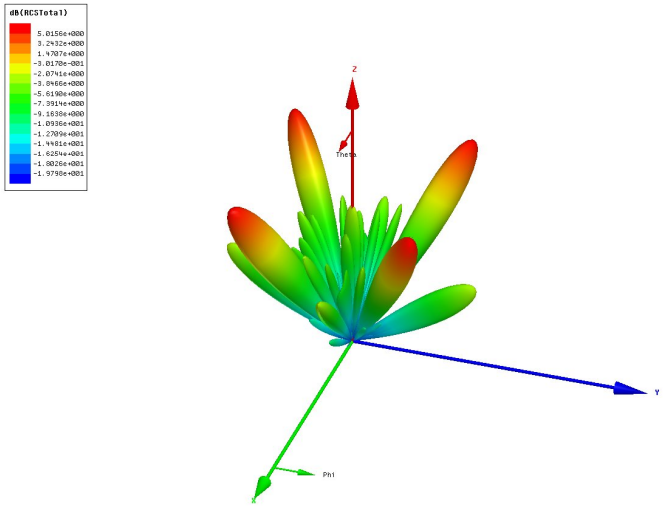

Fig. 3.11. Simulated Bistatic RCS Pattern for the Checkerboard Surface with Vias

surface has its maximum reduction in the normal direction. The RCS at the principal planes is 17.9 dB less than the RCS for the PEC ground plane. At the diagonal planes, the maxima of the RCS are at $\theta = 34°$, which is close to the expectation. By Equation 3.3 and Equation 3.4, the maxima are expected to be at $\phi = 45°$ and $\theta = 35.4°$. The difference can be attributed to the diffraction at the edges. The RCS at maxima is 8.5 dB less than that for the PEC ground plane, because the reflected fields are re-directed into four quadrants, instead of one in the normal direction.

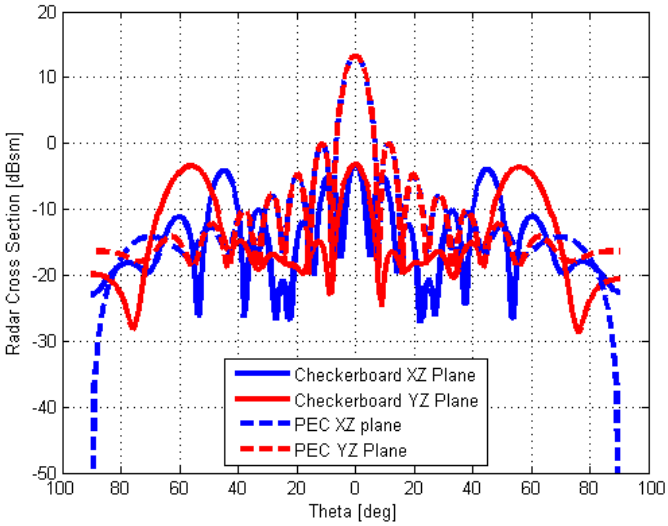

Fig. 3.12. Bistatic RCS Pattern in the Principal Planes for the Checkerboard Surface with Vias

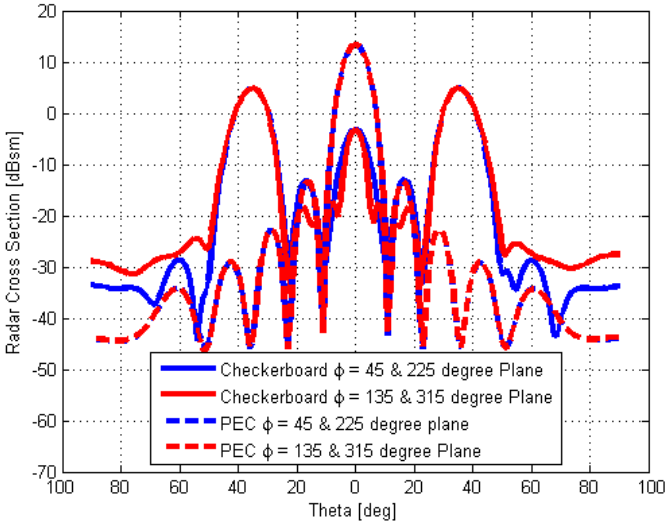

Fig. 3.13. Bistatic RCS Pattern in the Diagonal Planes for the Checkerboard Surface with Vias

3.3.3. *Checkerboard Surface without Vias*

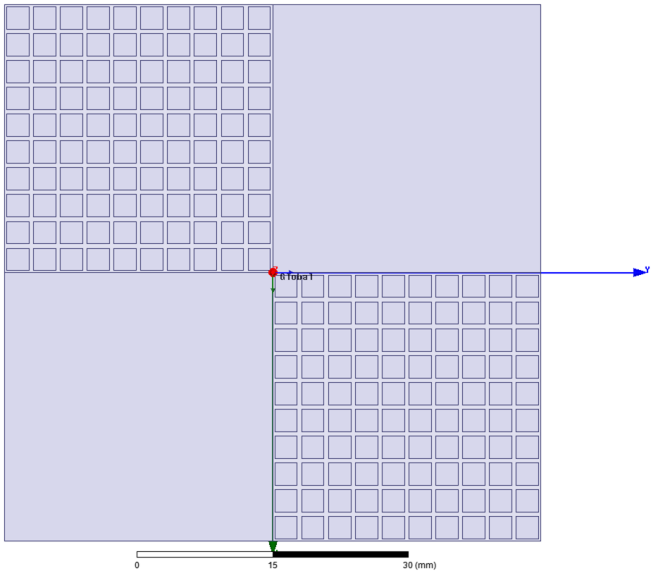

Fig. 3.14. Checkerboard Surface Combining PEC and EBG Structure without Vias

As discussed in the previous chapter, the absence of the via of the unit cell causes the resonant frequency to shift slightly. Thus, the unit cell of the EBG structure without via resonates at 12.3 GHz. The checkerboard surface without vias, as illustrated in Fig. 3.14, keeps all the other parameters the same as the checkerboard surface with vias. The only difference between them is the absence of the vias. The monostatic RCS reduction for normal incidence, as a function of frequency, is illustrated in Fig. 3.15. The RCS is reduced for more than 10 dB within the frequency of 11.50 - 12.45 GHz. The maximum reduction at 11.9 GHz is 37 dB. The resonant frequency is slightly shifted due to the diffraction from the edges. The bandwidth is 7.9%.

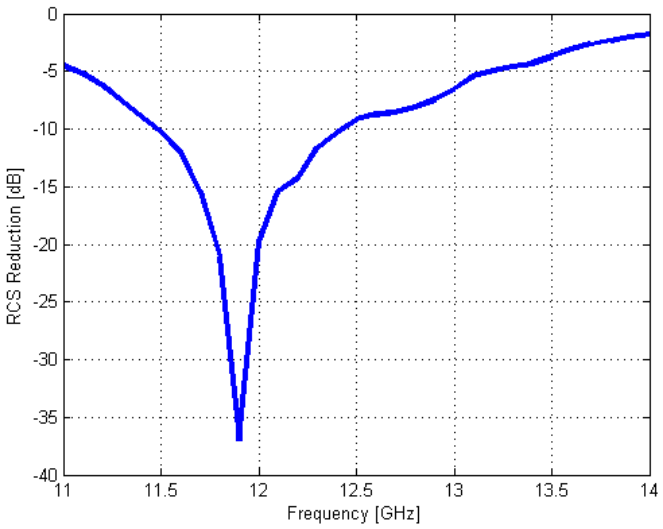

Fig. 3.15. Simulated Monostatic RCS Reduction as a Function of Frequency for the Checkerboard Surface without Vias

The bistatic RCS pattern at resonance is illustrated in Fig. 3.16. When the normal incident waves impinge on the surface, the RCS is dramatically reduced on the principal planes. However, the main reflected lobes appear at the four quadrants, $\phi = 45^\circ, 135^\circ, 225^\circ$ and 315°.

The scattering fields in the $\phi = 0^\circ$, 45°, 90°, 135°, 180°, 225°, 270° and 315° planes as a function of theta are illustrated in Figs. 3.17 and 3.18. The RCS, at the principal planes, is 18.8 dB less than the RCS for the PEC ground plane. At the diagonal planes, the maxima of the RCS are at $\theta = 35^\circ$, which is close to the expectation. By Equation 3.3 and 3.4, the maxima are expected to be at $\phi = 45^\circ$ and $\theta = 36.5^\circ$. The angle is slightly increased from the angle of the checkerboard surface with vias, because the resonant frequency is decreased or the electrical size of the PEC and EBG structures is decreased. The RCS

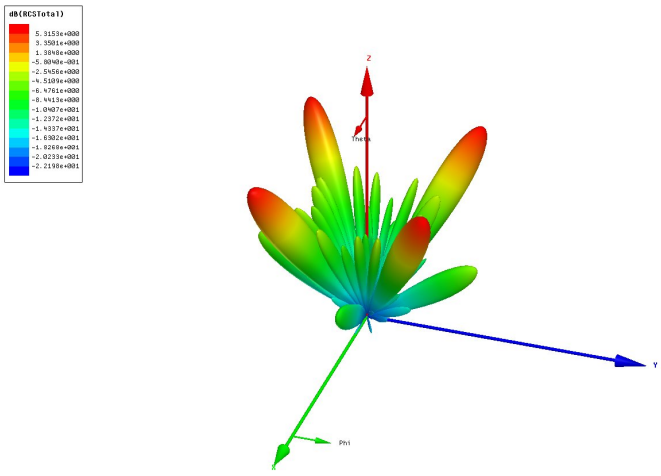

Fig. 3.16. Simulated Bistatic RCS Pattern for the Checkerboard Surface without Vias

at maxima is also 8.1 dB less than the maximum for the PEC ground plane, because the reflected fields are re-directed into four quadrants, instead of one in the normal direction.

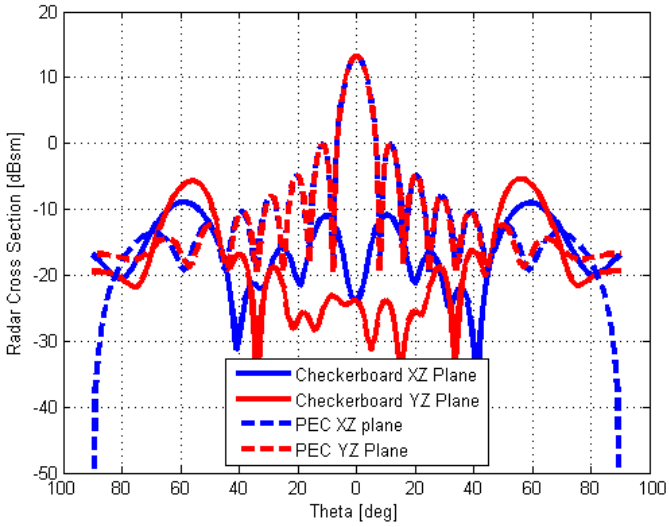

Fig. 3.17. Bistatic RCS Pattern in the Principal Planes for the Checkerboard Surface without Vias

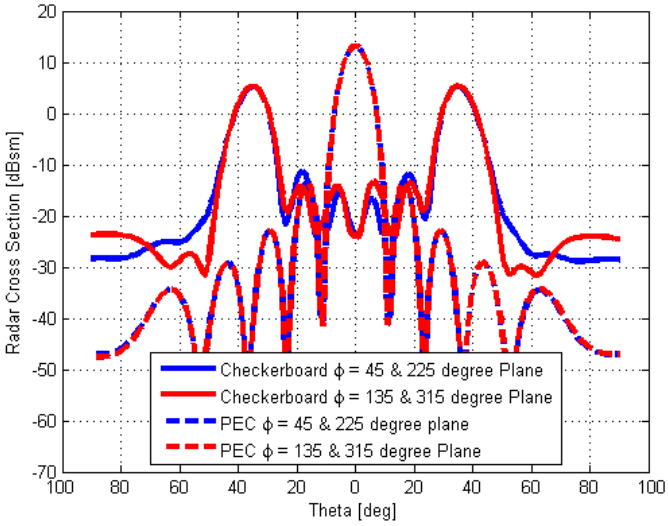

Fig. 3.18. Bistatic RCS Pattern in the Diagonal Planes for the Checkerboard Surface without Vias

3.4. Oblique Incidence

To analyze the scattering fields at oblique angles of incidence, it is easier to resolve the electric field into TE^z and TM^z polarizations, and then analyze each one individually. When the ground plane is placed on the XY plane and the electric field of the incidence wave is perpendicular to the Z-axis and parallel to the ground plane, the polarization of the incidence wave is defined to as TE^z polarization. When the ground plane is placed on the XY plane and the magnetic field of the incidence wave is perpendicular to the Z-axis and parallel to the ground plane, the polarization of the incidence wave is defined to as TM^z polarization. The polarization states are illustrated in Fig. 3.19.

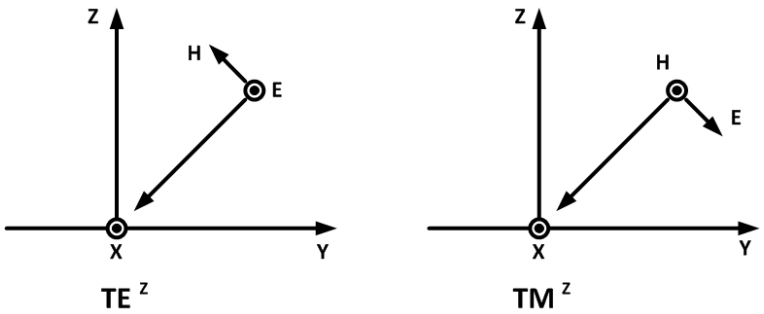

Fig. 3.19. TE^z and TM^z Polarized Plane Incident Wave at Oblique Angle

The phase of the reflection coefficient of an EBG structure is dependent on the incidence angle and the polarization of the incident wave [42]. The incident angle is defined as the angle of the propagation vector from the Z-axis. Thus, the incident angle varies from 0° to 90°. For TE^z incident wave, the electric field is parallel to the patches and perpendicular to the vias, so the effects of the vias on the phase of the reflection coefficient can be negligible. The current induced on the patches has no changes as a function of the incident angle. For

TM^z incident wave, the magnetic field is parallel to the patches and perpendicular to the vias. This means that the electric field has a vertical component parallel to the vias and a horizontal component parallel to the patches. The magnitudes of those components are dependent on the incident angle, so the current induced on the vias and the patches depends on the incident angle. Thus, the phase of the reflection coefficient is significantly affected by the incidence angle for TM^z incidence. The oblique wave incidences at angle $\phi = 90^\circ$ and $\theta = 30^\circ$ are examined in this section.

3.4.1. *Conventional Ground Plane (PEC, EBG)*

The bistatic RCS patterns of the PEC ground plane and the EBG structure plane for the oblique incident wave in both TE^z and TM^z cases are simulated with HFSS. For the PEC ground plane, the reflected fields, illustrated in Fig. 3.20 and Fig. 3.21, scatter along the specular direction. The magnitude of the reflected field for TM^z case is slightly less than that for TE^z case, because of a lesser amount of current induced on the plane. For the EBG structure plane, the reflected fields also scatter along the specular direction in both cases, which are illustrated in Fig. 3.22 and Fig. 3.23. However, the magnitude of the reflected field for TM^z case is also less than that of TE^z case, because of the oblique wave incidence effects.

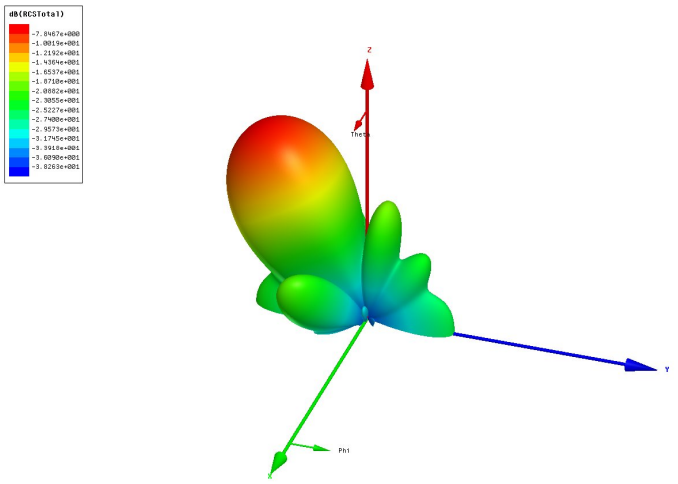

Fig. 3.20. Bistatic RCS Pattern of the PEC Ground Plane for TE^z Polarization at Oblique Incident Angle $\phi = 90^\circ$ and $\theta = 30^\circ$

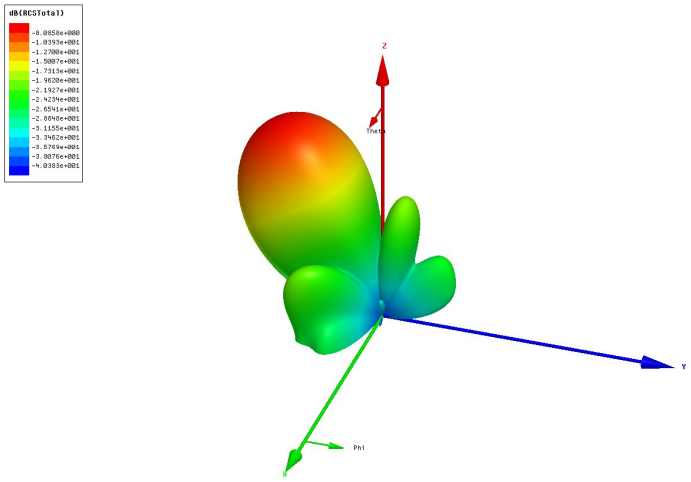

Fig. 3.21. Bistatic RCS Pattern of the PEC Ground Plane for TM^z Polarization at Oblique Incident Angle $\phi = 90^\circ$ and $\theta = 30^\circ$

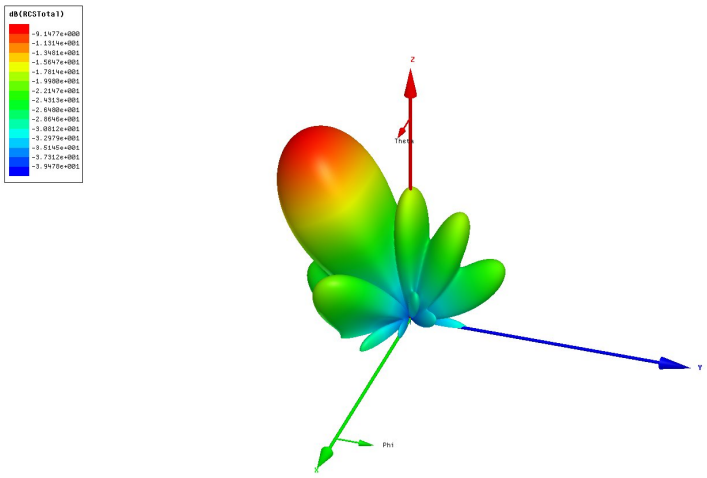

Fig. 3.22. Bistatic RCS Pattern of the EBG Ground Plane for TE^z Polarization at Oblique Incident Angle $\phi = 90^\circ$ and $\theta = 30^\circ$

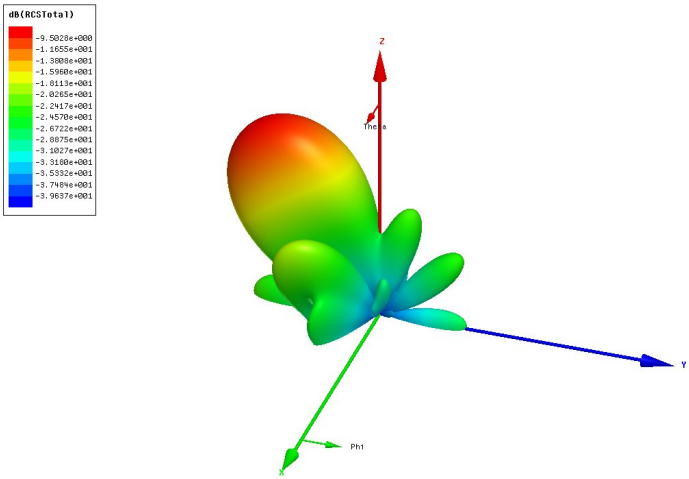

Fig. 3.23. Bistatic RCS Pattern of the EBG Ground Plane for TM^z Polarization at Oblique Incident Angle $\phi = 90^\circ$ and $\theta = 30^\circ$

3.4.2. *Checkerboard Surface with Vias*

The checkerboard surfaces with vias for TE^z and TM^z polarized oblique wave incidences indicates that the TM^z polarized oblique wave incidence has more significant effects, because the horizontal and vertical components of the electric fields are changed with the angle of the incidence. A significant lobe appears in the specular direction where a null is expected to be present. The bistatic RCS pattern for TE^z and TM^z polarization at oblique incident angle $\phi = 90^\circ$ and $\theta = 30^\circ$ is illustrated in Fig. 3.24 and Fig. 3.25, respectively.

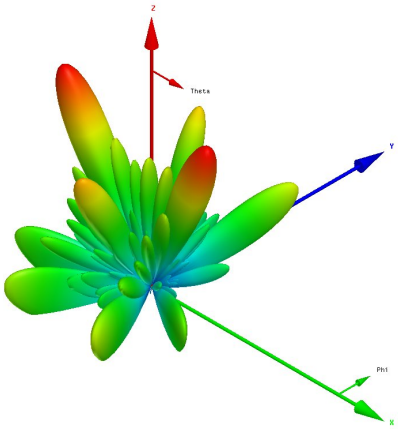

Fig. 3.24. Bistatic RCS Pattern of the Checkerboard Surface with Vias for TE^z Polarization at Oblique Incident Angle $\phi = 90^\circ$ and $\theta = 30^\circ$

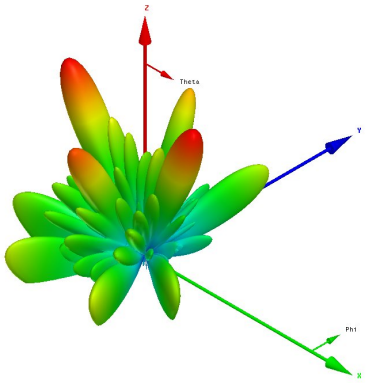

Fig. 3.25. Bistatic RCS Pattern of the Checkerboard Surface with Vias for TM^z Polarization at Oblique Incident Angle $\phi = 90^\circ$ and $\theta = 30^\circ$

3.4.3. *Checkerboard Surface without Vias*

The checkerboard surfaces without vias for TE^z and TM^z polarized oblique wave incidence are also simulated with HFSS. The results exhibit that the TM^z polarized oblique wave incidence has more significant effects than the TE^z polarized incidence. The results are the same as the checkerboard surface with vias. Although a null is expected to be present, a significant lobe appears in the specular direction. The TE^z polarized oblique wave incidence has less effects than the TM^z polarized incidence. The bistatic RCS pattern for TE^z and TM^z polarizations at oblique incident angle $\phi = 90^\circ$ and $\theta = 30^\circ$ is illustrated in Fig. 3.26 and Fig. 3.27, respectively.

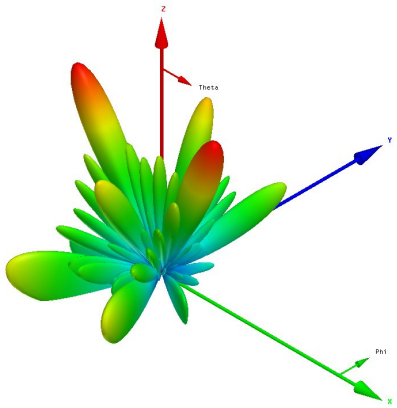

Fig. 3.26. Bistatic RCS Pattern of the Checkerboard Surface without Vias for TE^z Polarization at Oblique Incident Angle $\phi = 90^\circ$ and $\theta = 30^\circ$

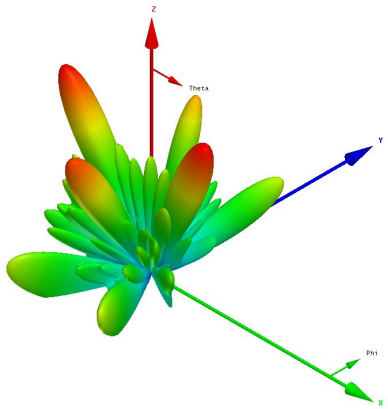

Fig. 3.27. Bistatic RCS Pattern of the Checkerboard Surface without Vias for TM^z Polarization at Oblique Incident Angle $\phi = 90^\circ$ and $\theta = 30^\circ$

CHAPTER 4

WIDE BAND CHECKERBOARD SURFACES (EBG1/EBG2)

This chapter extends the narrow band checkerboard surfaces to wider band checkerboard surfaces. An expression that approximates the 10-dB RCS reduction is developed for this wide band checkerboard surface. Both normal incidence and oblique incidence are also examined for this checkerboard design. Both TE and TM polarizations of oblique incidence are also discussed in this chapter.

4.1. Introduction

In Chapter 3, combining PEC and EBG structures on the same ground plane resulted in the cancellation of the reflected waves due to the 180° phase difference between their reflection phases. However, a significant RCS reduction occurs in a narrow frequency band. To reduce the RCS in a wider frequency band, two different kinds of EBG structures are designed to resonate at different frequencies. Thus, the 180° phase difference between the two different EBG structures can be realized over a wider frequency band, so that a significant RCS reduction occurs over a wider frequency band in comparison to that of combining PEC and EBG structures.

4.2. Analysis of Checkerboard Surfaces

To increase the frequency bandwidth of RCS reduction, two different EBG structures (EBG1 and EBG2) were designed to resonate at different frequencies so that there is a 180° phase difference between them. Fig. 4.1 illustrates a checkerboard surface which consists of four elements: two EBG1 with 4x4 square patches and two EBG2 with 4x4 circular patches. This surface can be treated as a planar array with a progressive phase shift of around 180°. For this ground plane, the array factor can also be represented by (3.2). The

phases of the two EBG structures, as well as the phase difference between them, are plotted in Fig. 4.2. The principal maximum, directed along ϕ_0, θ_0, can also be found using (3.3) and (3.4).

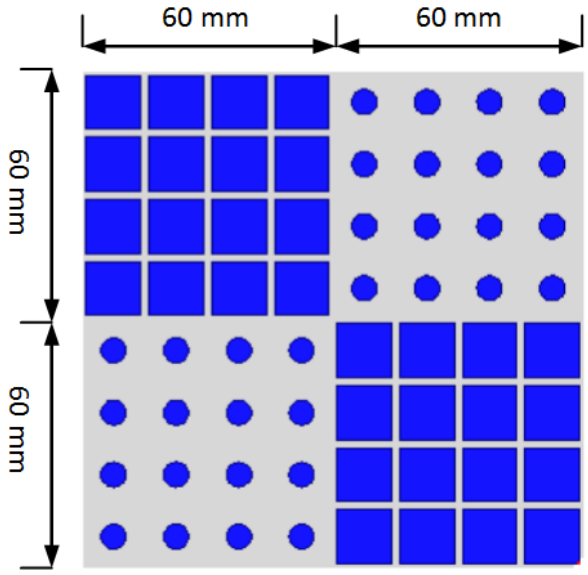

Fig. 4.1. One Period of a Square Checkerboard Surface that Combines EBG1 and EBG2 structures Alternately with their 4x4 Square Patches and 4x4 Circular Patches.

The RCS reduction of a scattering surface, compared to that of a PEC, can be represented by

$$\begin{aligned} \text{RCS Reduction} &= 10\log\left[\frac{\lim\limits_{r\to\infty}\left[4\pi r^2\frac{|E^s|^2}{|E^i|^2}\right]}{\lim\limits_{r\to\infty}\left[4\pi r^2(1)^2\right]}\right] \\ &= 10\log\left[\frac{|E^s|^2}{|E^i|^2}\right] \end{aligned} \tag{4.1}$$

which for a dual EBG checkerboard surface can be approximated by

$$\text{RCS Reduction} = 10\log\left[\frac{A_1 e^{jP_1} + A_2 e^{jP_2}}{2}\right]^2 \tag{4.2}$$

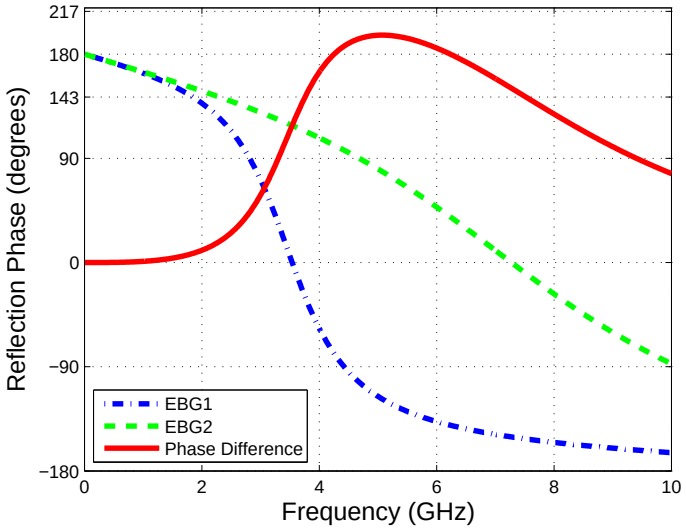

Fig. 4.2. Reflection Phases of EBG1 and EBG2 Structures and Phase Difference between the Two EBG Structures.

where A_1 and A_2 are the reflection coefficient amplitudes of the two EBG structures, and P_1 and P_2 are their reflection phases. In (4.1), the ratio of the scattered field and the incident field is equal to the reflection coefficient of the surface. Since the checkerboard surface consists of two EBG surfaces, each of the EBG surfaces occupies exactly half of the area of the entire checkerboard surface. Thus, the reflection coefficient of the entire surface can be expressed by the average reflection coefficient of the two EBG structures. Therefore, the RCS reduction can be approximated by (4.2), which does not include edge effects, but provides a good guideline for RCS reduction of a dual EBG surface compared to that of a PEC. This will be verified with the examples that follow.

By applying (4.2), the broadside RCS reduction of a checkerboard surface versus the phase difference of two EBG structures is displayed in Fig. 4.3. A 10 dB RCS reduction

occurs, in the ideal case of an infinite checkerboard surface, within $180^\circ \pm 37^\circ$ phase difference between the two EBG structures. The RCS reduction of the checkerboard surface, compared to the RCS of a PEC ground plane, can be approximated by (4.2). Thus, the predicted RCS reduction as a function of frequency is illustrated in Fig. 4.4, and it exhibits a 10 dB reduction over a wider frequency band of 3.76 - 7.51 GHz, which is 67%. This is about 4% greater than the RCS reduction bandwidth predicted using full-wave simulation (HFSS).

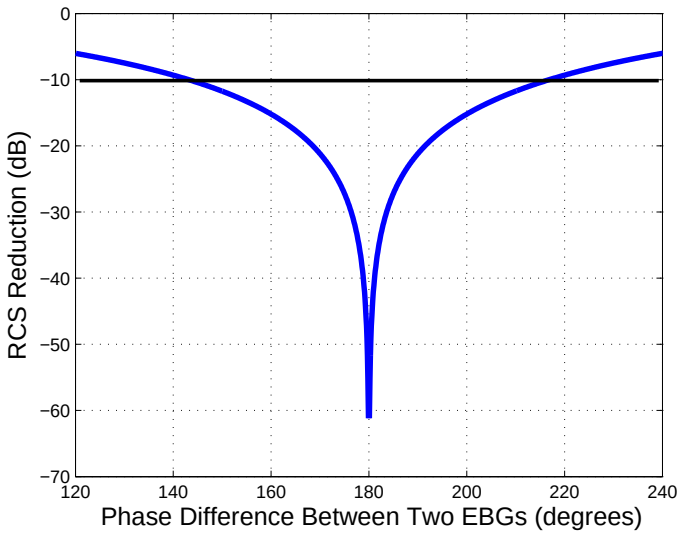

Fig. 4.3. Approximate RCS Reduction Completed with (4.2) Shows that a 10-dB RCS Reduction for the Ideal Case of an Infinite Checkerboard Surface Occurs within the $180^\circ \pm 37^\circ$ Phase Difference Region between two EBG Structures.

4.3. Normal Incidence

A surface combining the EBG1 and EBG2 structures is illustrated in Fig. 4.1. The equal-sized EBG structures (EBG1 and EBG2) are placed alternately one after another. The 2x60 mm period was selected to produce the four scattered beams whose maxima are

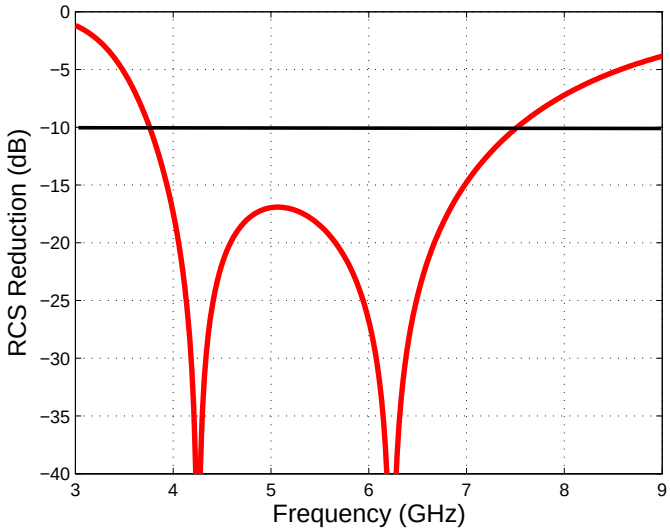

Fig. 4.4. Approximated RCS Reduction versus Frequency for the Checkerboard Design Combining EBG1 and EBG2 Structures. Predicted RCS Reduction Bandwidth using the Approximate Expression is 67%.

at approximately 45 degrees from the direction of incidence. If the period is increased, the maxima of scattered beams will occur in directions that are closer (less than 45 degrees) to the incidence direction. Simulations and measurements of the checkerboard surface are compared and presented in this section. The monostatic RCS patterns are discussed in detail, including the effects of polarization (TE^z and TM^z) under oblique wave incidence.

The substrate used for this checkerboard surface is Rogers RT/duroid 5880 with a thickness of 6.35 mm and a dielectric constant of 2.2 and overall dimension of 240 mm x 240 mm. The checkerboard (EBG1 + EBG2) surface design was simulated and fabricated, as illustrated in Fig. 4.5, and its scattering characteristics were measured at Arizona State University's (ASU) ElectroMagnetic Anechoic Chamber (EMAC) facility. The checkerboard plane was supported on top of an expanded polystyrene column. The measurements

were performed using a compact antenna test range, as shown in Fig. 4.6. An HP8510C Vector Network Analyzer is used as the instrumentation.

The RCS of the checkerboard surface was measured over the frequency band of 3.8 - 8.8 GHz. The RCS reduction maxima are more than 25 dB at 4.65 GHz and 6.85 GHz, while the RCS is reduced by more than 10 dB within the frequency band of 4.10 - 7.59 GHz. Thus, the measured RCS reduction bandwidth is 60%. Comparison of the measured and simulated RCS reduction, as illustrated in Fig. 4.7, results in an excellent agreement over the entire frequency band.

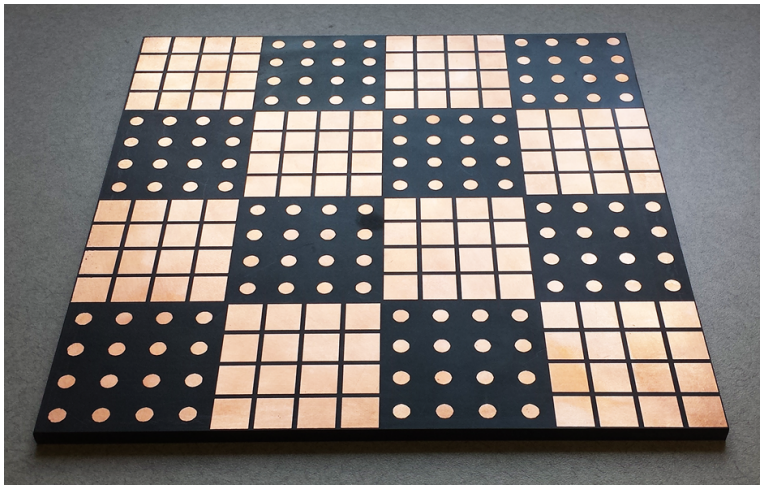

Fig. 4.5. Fabricated Square Checkerboard Surface Combining EBG1 and EBG2 Structures.

The 3-D bistatic RCS pattern at 4.7 GHz is illustrated in Fig. 4.8. Under normal incidence, the RCS is dramatically reduced along the principal planes (XZ, YZ) and the main reflected lobes appear at the four quadrants, $\phi = 45°$, 135°, 225° and 315°.

The scattered fields versus the elevation angle theta (θ) at 4.7 GHz, along the principal and diagonal planes, are illustrated in Figs. 4.9 and 4.10, respectively. The RCS for the

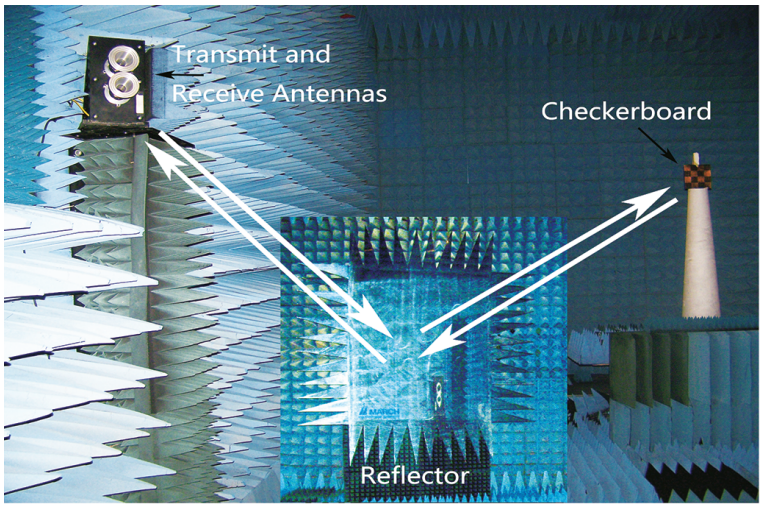

Fig. 4.6. Measurement Setup at the ASU EMAC Facility.

checkerboard surface is compared with the RCS for the PEC ground plane. The maximum RCS in the principal planes is 19.2 dB less than the maximum RCS for the PEC ground plane. In the diagonal planes, the maxima of the RCS are at $\theta = 47^\circ$, which is close to the angle ($\theta = 49^\circ$) predicted by (3.3) and (3.4). The difference may be due to the diffraction from the edges. The maximum RCS of the checkerboard surface is 8.1 dB less than that for the PEC ground plane. This reduction occurs because the reflected fields are re-directed into four main lobes, instead of the single main lobe of the PEC surface.

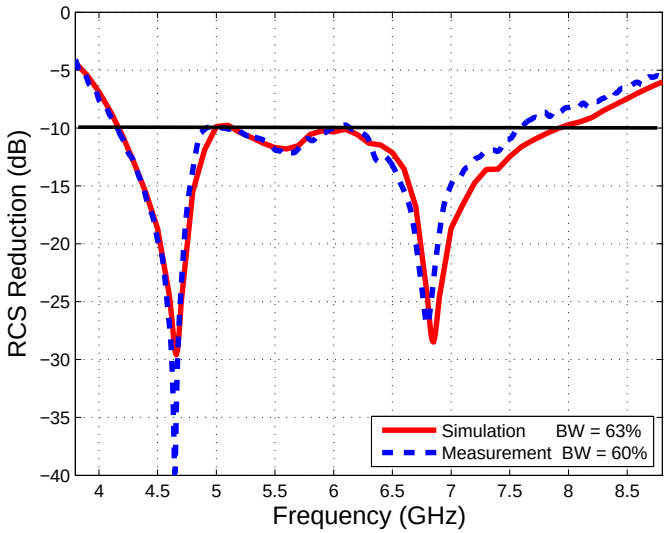

Fig. 4.7. Normal Incidence RCS Reduction versus Frequency for the Square Checkerboard Surface. A 10-dB RCS Reduction Bandwidth for the Checkerboard Surface is 63%. The Measured RCS Reduction, with a Bandwidth of 60%, is in Very Good Agreement with the Simulation.

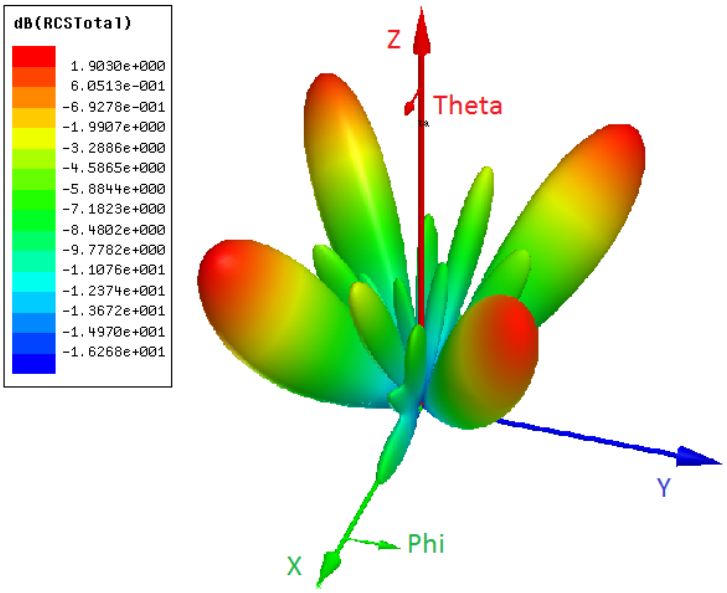

Fig. 4.8. 3-D Bistatic Scattered Fields at 4.7 GHz under Normal Incidence for the Square Checkerboard Surface.

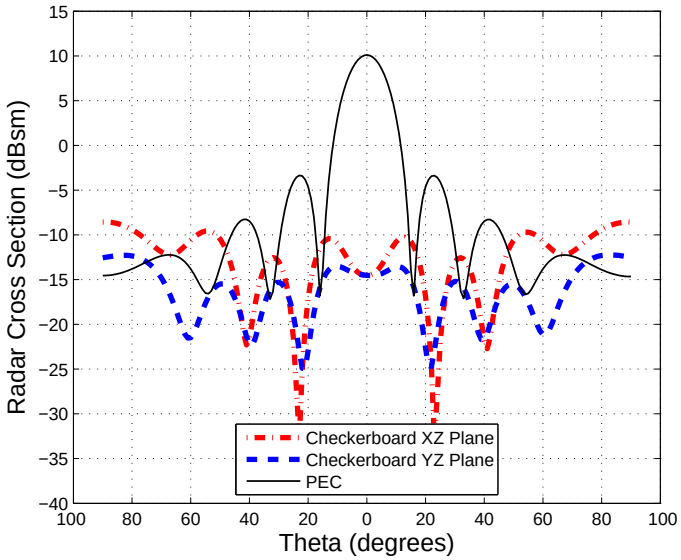

Fig. 4.9. Comparison of the Bistatic Scattered Fields at 4.7 GHz along the Principal Planes for the Square Checkerboard Surface and the PEC Ground Plane.

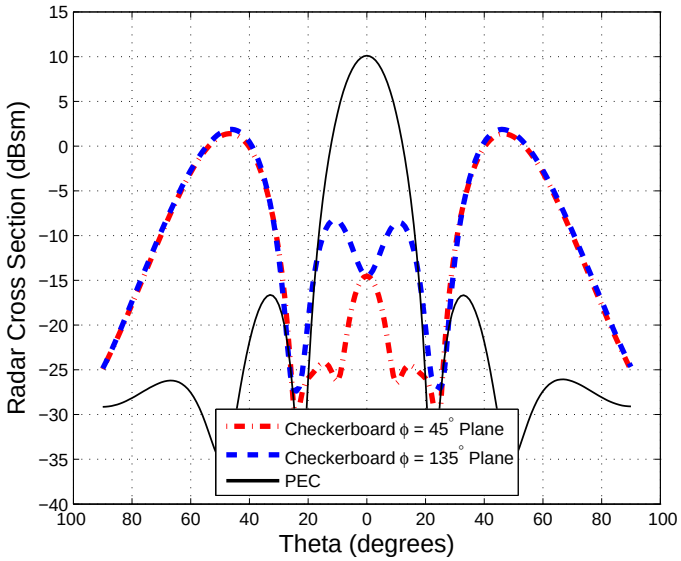

Fig. 4.10. Comparison of the Bistatic Scattered Fields at 4.7 GHz along the Diagonal Planes for the Square Checkerboard Surface and the PEC Ground Plane.

4.4. Oblique Incidence

The phase of the reflection coefficient of an EBG structure depends on the incident angle and polarization of the incident wave [42]; therefore oblique incidence for the TE^z and TM^z polarizations are investigated. The scattered fields at the oblique incident angle $\phi = 90°$, $\theta = 30°$ for both polarizations are examined. In addition, the monostatic RCS patterns at the resonant frequency for TE^z and TM^z polarized fields under oblique wave incidence are simulated, measured and compared with those for the equal-sized PEC ground planes.

4.4.1. *TE^z Polarized Wave Incidence*

The predicted 3-D bistatic RCS pattern for the TE^z polarization at the oblique incident angle of $\phi = 90°$, $\theta = 30°$ is illustrated in Fig. 4.11. Although an ideal null is expected at the specular direction ($\phi = 270°$, $\theta = 30°$), instead a minor lobe (-10.2 dB) appears in that direction. In addition, a minor lobe (-10.2 dB) is created along backscattered direction ($\phi = 90°$, $\theta = 30°$). These occur because the phase variations of the reflection coefficient of the EBG structure for the TE^z polarization are highly dependent on the incident angle [42].

The monostatic RCS patterns along the principal ($\phi = 0°$ and $90°$) and diagonal ($\phi = 45°$ and $135°$) planes at 4.7 GHz for the TE^z polarization are illustrated in Figs. 4.12 and 4.13, respectively. In the principal planes, the monostatic RCS patterns for the checkerboard surface are reduced by approximately 25 dB in the normal direction. The maxima of the minor lobes are 10.2 dB less than the maximum of the corresponding PEC ground plane. The measured patterns are in excellent agreement with the simulated data. In

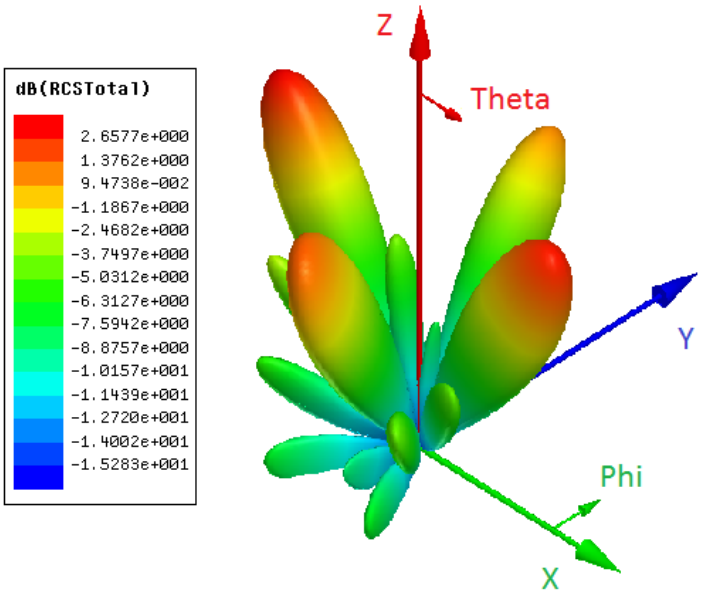

Fig. 4.11. 3-D Bistatic RCS at 4.7 GHz for TE^z Polarization at Incident Angle $\phi = 90°$, $\theta = 30°$.

the diagonal planes, the monostatic RCS patterns illustrate that the reflected lobes appear at $\theta = 21°$. This is expected because the checkerboard surface does not absorb energy, but rather redirects it. The minor lobes appear along $\theta = 50°$. However, the maxima for the checkerboard surface are 8.2 dB less than the maximum for the PEC ground plane. The patterns at the diagonal planes are not identical at large elevation angles because the physical layout of the EBG square and circular patches along those two plane cuts is different; thus the corresponding reflection phases are different. However, the measured patterns are in excellent agreement with the simulated ones.

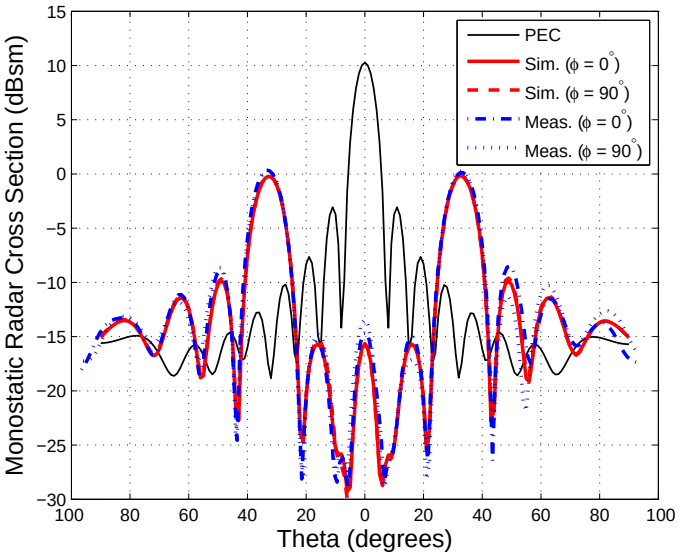

Fig. 4.12. Comparison of the Monostatic RCS at 4.7 GHz for TE^z Polarization along the Principal Planes for the Square Checkerboard Surface and the PEC Ground Plane.

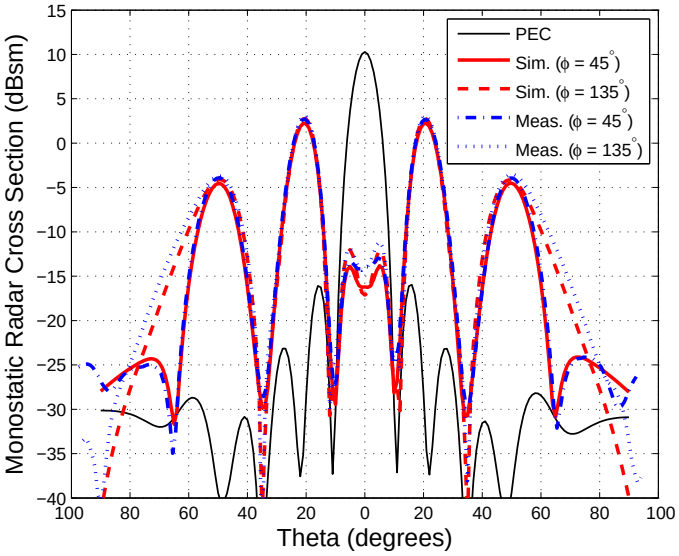

Fig. 4.13. Comparison of the Monostatic RCS at 4.7 GHz for TE^z Polarization along the Diagonal Planes for the Square Checkerboard Surface and the PEC Ground Plane.

4.4.2. *TM^z Polarized Wave Incidence*

The simulated 3-D bistatic RCS pattern at 4.7 GHz for the TM^z polarization oblique incident angle $\phi = 90°$, $\theta = 30°$ is illustrated in Fig. 4.14. In contrast to the TE^z polarization, the scattered lobe in the specular direction ($\phi = 270°$, $\theta = 30°$) and the backscattered lobe appear to be negligible. The induced current on the patches is not strongly dependent on the incident angle for the TM^z polarized fields [42]. Therefore, the reflection phase of the EBG structure is not significantly impacted by the incident angle.

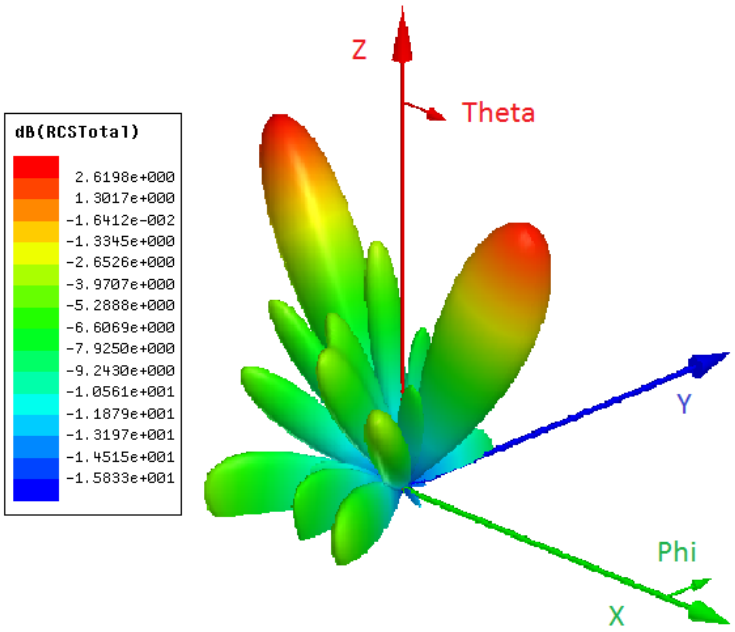

Fig. 4.14. 3-D Bistatic RCS at 4.7 GHz for TM^z Polarization at Incident Angle $\phi = 90°$, $\theta = 30°$.

The monostatic RCS patterns at 4.7 GHz for the TM^z polarization are illustrated in Figs. 4.15 and 4.16 for the principal and diagonal planes, respectively. In the principal planes, the monostatic RCS for the checkerboard surface is reduced by more than 23 dB along the

normal direction. The maximum is 17.6 dB less than the maximum for the PEC ground plane. In the diagonal planes, the monostatic RCS patterns illustrate that the reflected lobes appear at $\theta = 21^{\circ}$. While the minor lobes appear along $\theta = 50^{\circ}$. However, the maxima for the checkerboard surface are 9.8 dB less than the maximum of the corresponding PEC ground plane. The measured patterns along the principal and diagonal planes are in excellent agreement with the simulated ones.

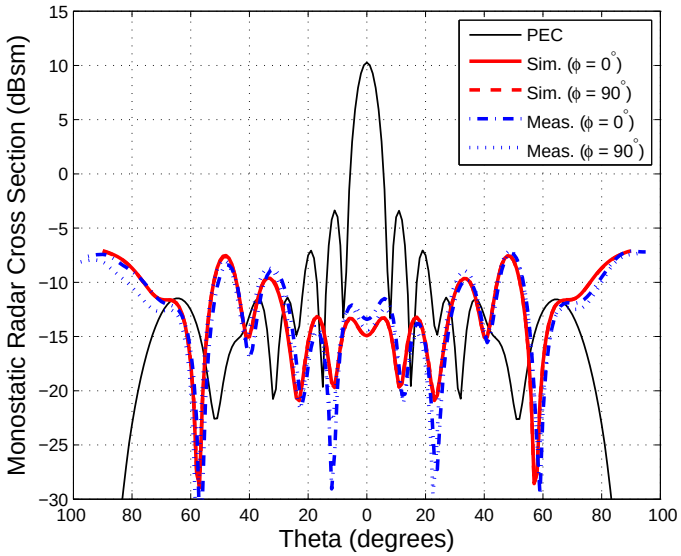

Fig. 4.15. Comparison of the Monostatic RCS at 4.7 GHz for TM^z Polarization along the Principal Planes for the Square Checkerboard Surface and the PEC Ground Plane.

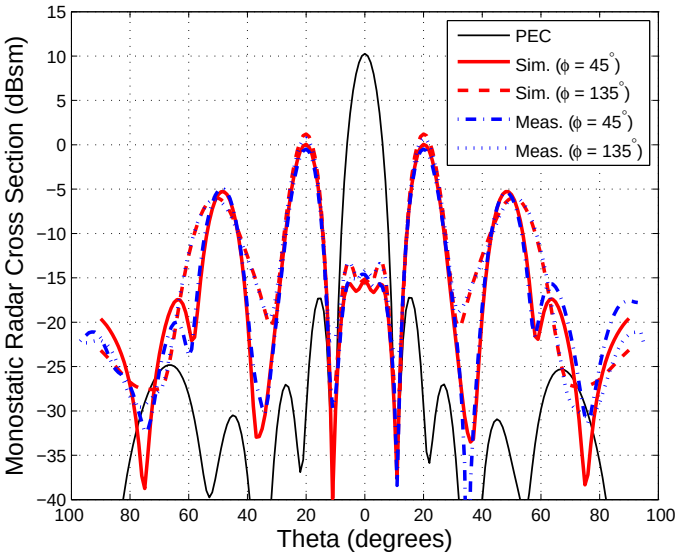

Fig. 4.16. Comparison of the Monostatic RCS at 4.7 GHz for TM^z Polarization along the Diagonal Planes for the Square Checkerboard Surface and the PEC Ground Plane.

Through simulations, the bandwidth of 10-dB RCS reduction versus frequency for TE polarization is shown in Fig. 4.17, and a summary is listed in Table 4.1. Both indicate a bandwidth reduction as the incidence angle increases. Nearly the same results, which are not included here to minimize duplication, were obtained for TM^z polarization.

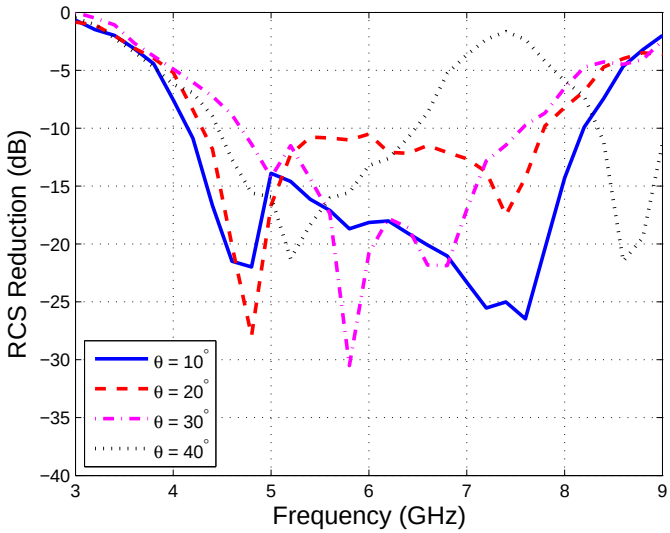

Fig. 4.17. TE^z Polarization RCS Reduction as Function of Frequency for Different Incident Angles.

Table 4.1. RCS Reduction Bandwidth for Different Incident Angles.

Incident Angle	-10-dB Bandwidth
0°	63%
10°	64%
20°	55%
30°	45%
40°	34%

CHAPTER 5

HEXAGONAL CHECKERBOARD SURFACES

A novel design of checkerboard surfaces in a hexagonal design is proposed in this chapter. The hexagonal checkerboard surface is simulated and measured for both normal incidence and oblique incidence. The simulation and measurement results prove that the expression also applies to this design of checkerboard surfaces.

5.1. Introduction

An alternate geometry that uses the dual EBG strategy is the hexagonal checkerboard surface. Since it also use the same two EBGs, it should have an RCS reduction bandwidth similar to that of the square checkerboard surface. Thus, a unique and first-of-its-shape hexagonal checkerboard surface is proposed in this section. One period of the hexagonal checkerboard is illustrated in Fig. 5.1. It consists of six elements: three EBG1 structures with square patches and three EBG2 structures with circular patches, but each EBG structure is skewed to form triangles in order to structure the hexagonal surface. The hexagonal surface, illustrated in Fig. 5.2, with the overall dimension of 300 mm x 240 mm, was simulated and fabricated on the same substrate as the square checkerboard surface. The period was selected, based on array theory, to create six bistatic main beams. Simulations and measurements are compared and discussed in this section.

5.2. Normal Incidence

The RCS reduction of the hexagonal checkerboard surface is the same as that of the square checkerboard surface because it consists of the same two EBG structures. As illustrated in Fig. 5.3, the 10-dB RCS reduction bandwidth is 61% (4.2 - 7.9 GHz) and 60% (4.2 - 7.8 GHz) from the simulation and measurement, respectively; an excellent agreement

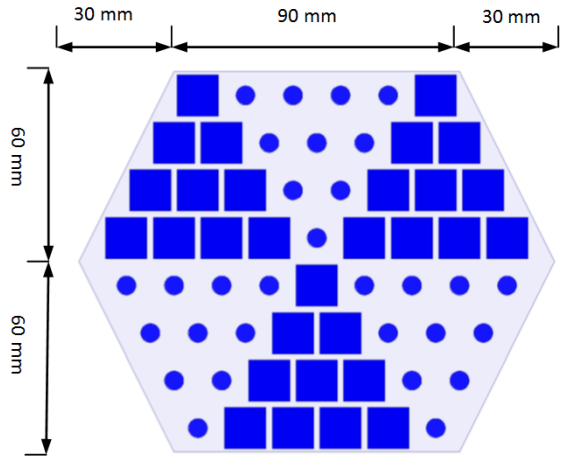

Fig. 5.1. One Period of a Hexagonal Checkerboard Surface that Combines EBG1 and EBG2 Structures Alternately with their Square Patches and Circular Patches.

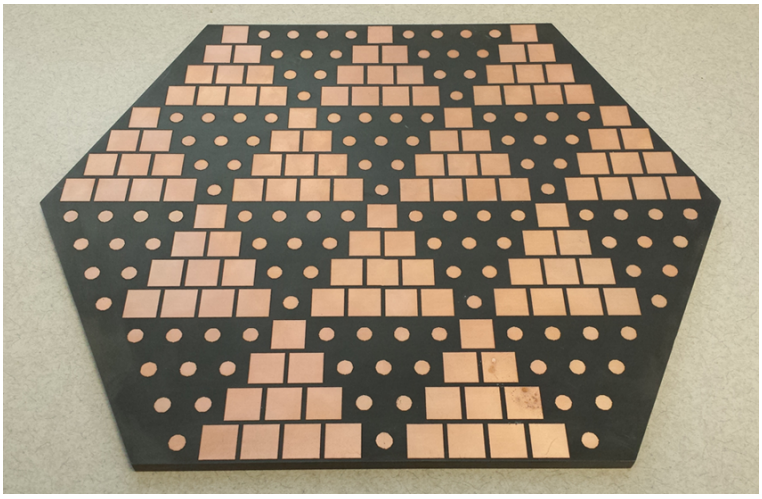

Fig. 5.2. Fabricated Hexagonal Checkerboard Surface Combining EBG1 and EBG2 Structures.

between the simulations and measurements. However, the hexagonal surface re-directs the reflected energy toward six directions, resulting in enhanced RCS reduction for each of its maxima.

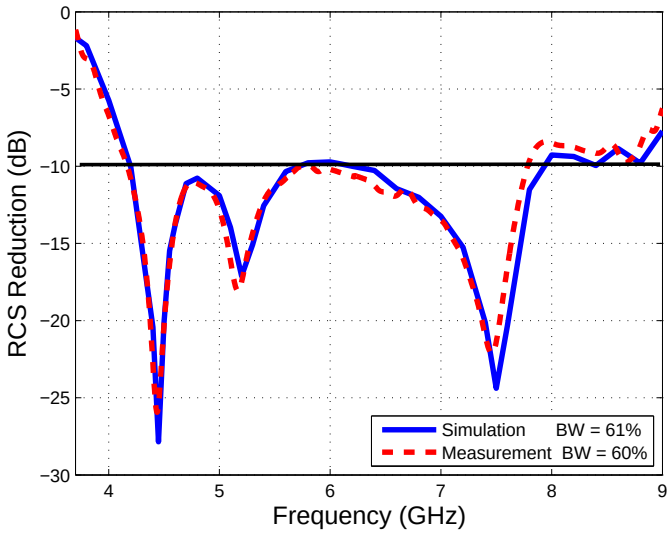

Fig. 5.3. Normal Incidence RCS Reduction versus Frequency for the Square Checkerboard Surface. A 10-dB RCS Reduction Bandwidth for the Checkerboard Surface is 63%. The Measured RCS Reduction, with a Bandwidth of 60%, is in Very Good Agreement with the Simulation.

The bistatic RCS pattern at the resonance is illustrated in Fig 5.4. When the normal incident waves impinge on the surface, the RCS is dramatically small in the $\phi = 30^\circ, 90^\circ, 150^\circ, 210^\circ, 270^\circ$ and 330° planes and the main reflected lobes appear at the six quadrants, $\phi = 0^\circ, 60^\circ, 120^\circ, 180^\circ, 240^\circ$ and 300°.

The scattering fields as a function of theta at 4.5 GHz in the $\phi = 0^\circ$, 30°, 60°, 90°, 120°, 150°, 180°, 210°, 240°, 270°, 300° and 330° planes are illustrated in Figs. 5.5 and 5.6. The RCS for the hexagonal checkerboard surface is compared with the RCS for the PEC ground plane. The RCS at the $\phi = 30^\circ, 90^\circ, 150^\circ, 210^\circ, 270^\circ$ and 330° planes is 21.5 dB less than the RCS for the PEC ground plane. In the other planes, two of the maxima are 9.1 dB less than the maximum for the PEC ground plane; the other four maxima are 12.6 dB less than

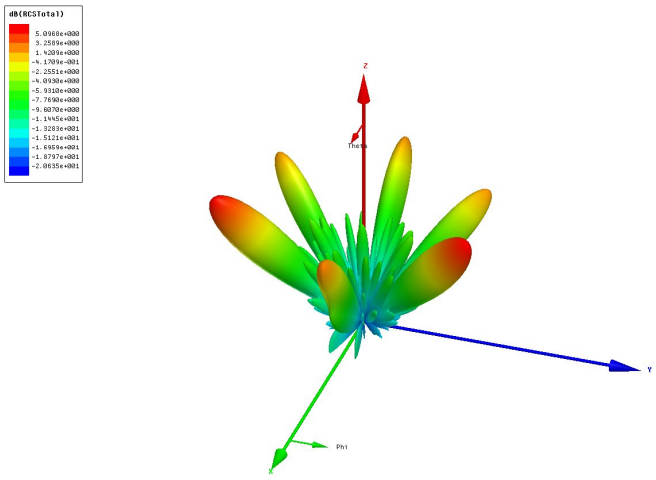

Fig. 5.4. 3-D Bistatic Scattered Fields at 4.5 GHz under Normal Incidence for the Hexagonal Checkerboard Surface.

the maximum for the PEC ground plane. The RCS of the hexagonal checkerboard exhibits maxima between $\theta = 43^\circ - 44^\circ$, because the hexagon is not equilateral.

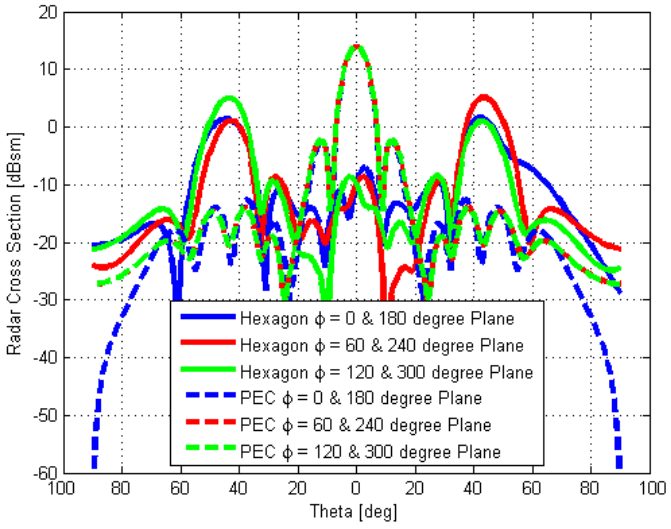

Fig. 5.5. Bistatic RCS Pattern at 4.5 GHz in $\phi = 0^\circ$, 60°, 120°, 180°, 240° and 300° Planes for the Hexagon Configuration.

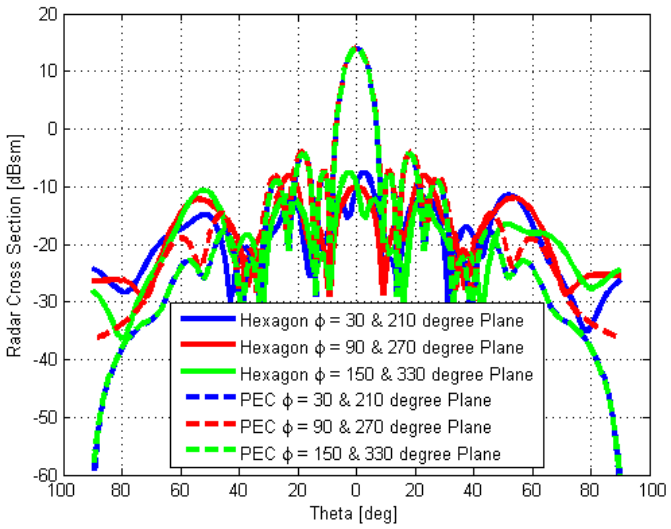

Fig. 5.6. Bistatic RCS Pattern at 4.5 GHz in $\phi = 30°$, $90°$, $150°$, $210°$, $270°$ and $330°$ Planes for the Hexagon Configuration.

The 3D pattern of the scattering fields at 7.5 GHz is illustrated in Fig. 5.7. The scattering fields as a function of theta in the $\phi = 0°$, $30°$, $60°$, $90°$, $120°$, $150°$, $180°$, $210°$, $240°$, $270°$, $300°$ and $330°$ planes are illustrated in Figs. 5.8 and 5.9. The RCS for the hexagonal checkerboard surface is compared with the RCS for the PEC ground plane. The RCS at the $\phi = 30°, 90°, 150°, 210°, 270°$ and $330°$ planes is 23.6 dB less than the RCS for the PEC ground plane. At the other planes, two of the maxima are 8.35 dB less than the maximum for the PEC ground plane. The other four maxima are about 12 dB less than the maximum for the PEC plane. The RCS reaches the maximum at $\theta = 35° - 36°$ because the hexagon is not equilateral. Also, the maxima are at a lower angle theta than those at a lower frequency. This can be attributed to the increase in the solution frequency or the increase in the electrical size of the plane.

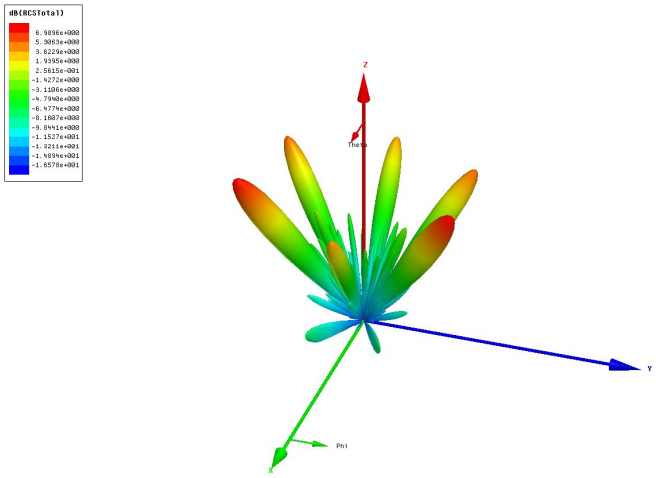

Fig. 5.7. 3-D Bistatic Scattered Fields at 7.5 GHz under Normal Incidence for the Hexagonal Checkerboard Surface.

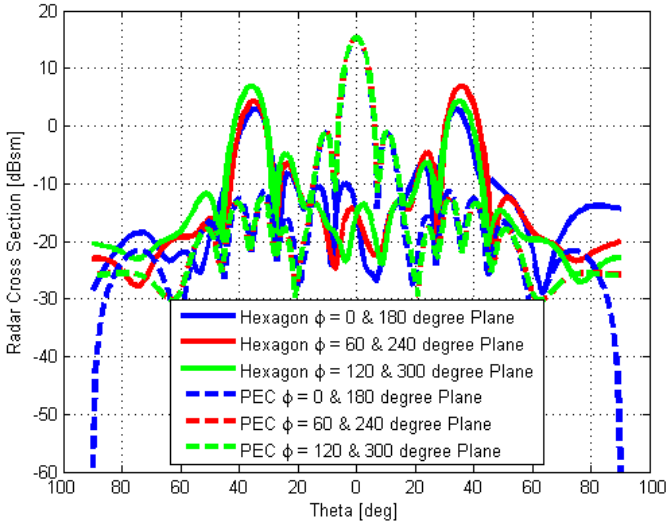

Fig. 5.8. Bistatic RCS Pattern at 7.5 GHz in $\phi = 0°$, $60°$, $120°$, $180°$, $240°$ and $300°$ Planes for the Hexagon Configuration.

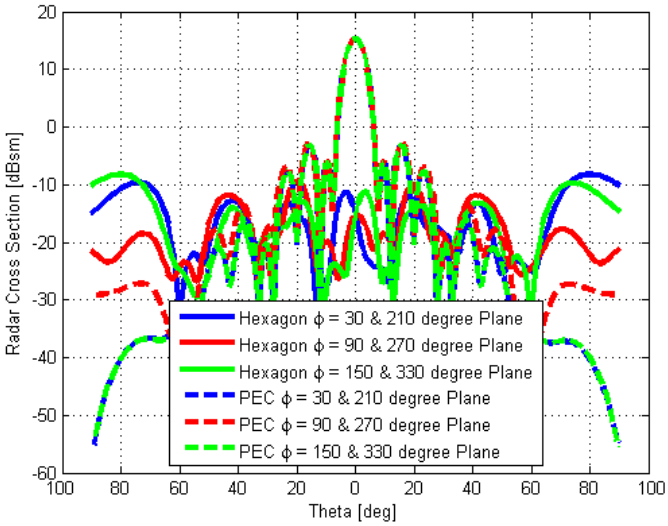

Fig. 5.9. Bistatic RCS Pattern at 7.5 GHz in $\phi = 30°$, $90°$, $150°$, $210°$, $270°$ and $330°$ Planes for the Hexagon Configuration.

5.3. Oblique Incidence

As stated before, it is also important to discuss the scattering characteristics under oblique incidence. The monostatic RCS patterns of the hexagonal checkerboard surface for both the TE^z and TM^z polarized fields are simulated, measured and compared with those of the equal-sized PEC ground plane.

5.3.1. *TE^z Polarized Wave Incidence*

The monostatic RCS patterns in the $\phi = 0^\circ, 60^\circ$ and 120° planes, where the main lobes appear, at 7.5 GHz for the TE^z polarization are illustrated in Figs. 5.10, 5.11 and 5.12, respectively. In the $\phi = 0^\circ$ plane, the maximum RCS is 9.5 dB less than the maximum for the PEC ground plane. The pattern in the $\phi = 60^\circ$ plane is symmetrically identical to the pattern in the $\phi = 120^\circ$ plane because the hexagonal checkerboard surface is symmetrical. In those planes, the RCS maxima of the checkerboard surface are 9.1 dB less than those for the PEC ground plane. The difference between the reductions at different planes can be attributed to the finite size of the surface and its inequilateral hexagonal structure. The measured patterns are in excellent agreement with the simulated patterns.

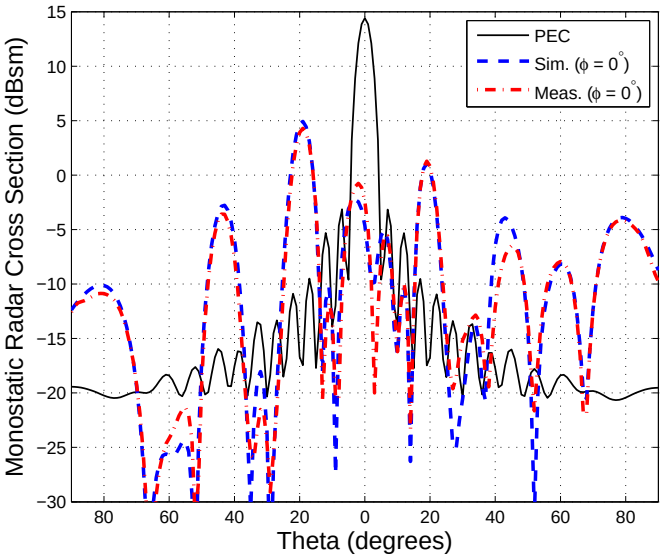

Fig. 5.10. Comparison of the Monostatic RCS at 7.5 GHz for TE^z Polarization along $\phi = 0^\circ$ Plane for the Hexagonal Checkerboard Surface and the PEC Ground Plane.

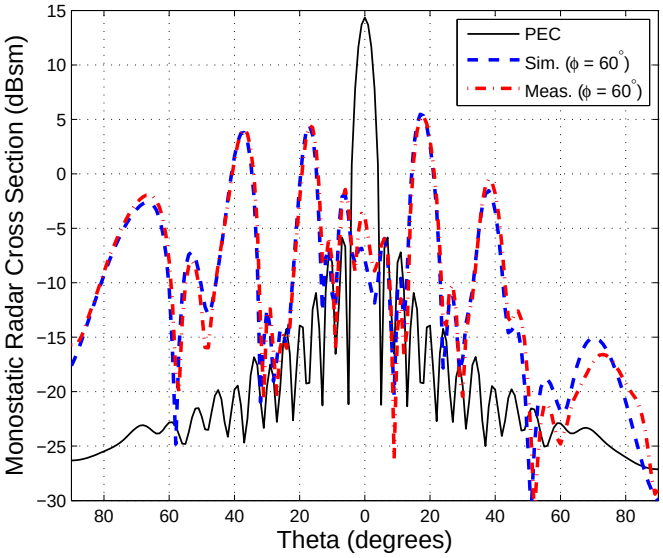

Fig. 5.11. Comparison of the Monostatic RCS at 7.5 GHz for TE^z Polarization along $\phi = 60^\circ$ Plane for the Hexagonal Checkerboard Surface and the PEC Ground Plane.

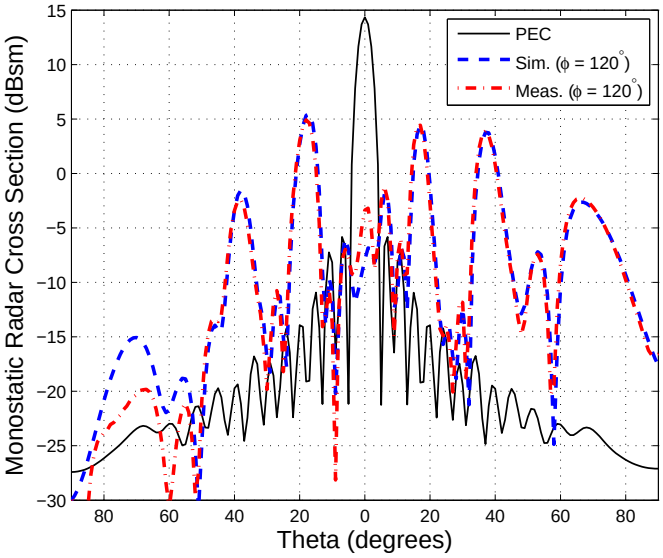

Fig. 5.12. Comparison of the Monostatic RCS at 7.5 GHz for TE^z Polarization along $\phi = 120^\circ$ Plane for the Hexagonal Checkerboard Surface and the PEC Ground Plane.

5.3.2. *TM^z Polarized Wave Incidence*

The monostatic RCS patterns in $\phi = 0^\circ, 60^\circ$ and 120° planes at 7.5 GHz for the TM^z polarization are illustrated in Figs. 5.13, 5.14 and 5.15, respectively. The maximum RCS is 8.0 dB less than the maximum for the PEC ground plane in the $\phi = 0^\circ$ plane. In the $\phi = 60^\circ$ and 120° planes, the maxima RCS of the checkerboard surface are 7.1 dB less than those for the PEC ground plane. Due to the finite size of the surface, the main lobes at $\theta = 18^\circ$ in each plane do not evenly distribute at the same value. The larger size of the surface, the closer the values of the maxima RCS. It will result in more reduction for the hexagonal checkerboard surface than the square checkerboard surface. Excellent agreement between the simulations and measurements is obtained.

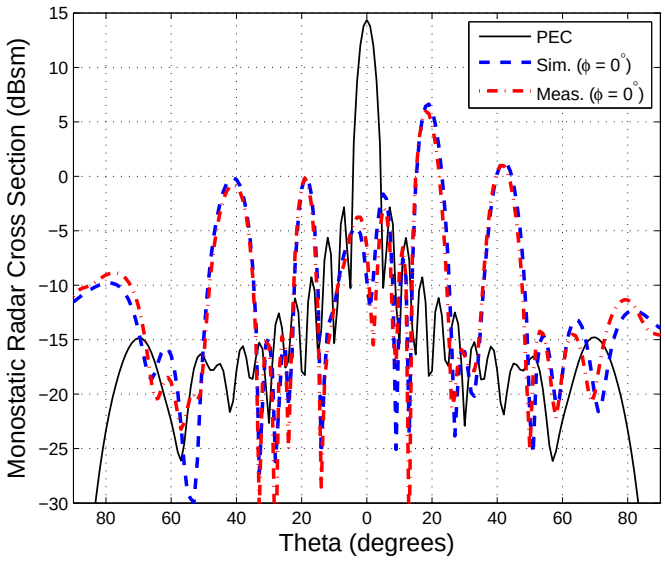

Fig. 5.13. Comparison of the Monostatic RCS at 7.5 GHz for TM^z Polarization along $\phi = 0^\circ$ Plane for the Hexagonal Checkerboard Surface and the PEC Ground Plane.

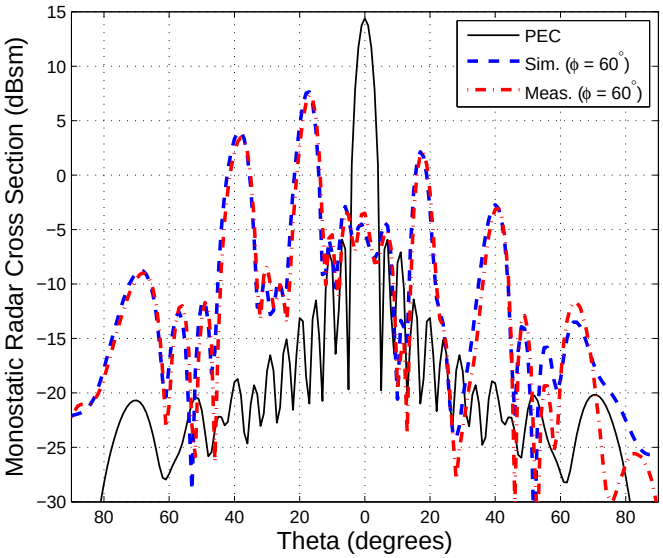

Fig. 5.14. Comparison of the Monostatic RCS at 7.5 GHz for TM^z Polarization along $\phi = 60^\circ$ Plane for the Hexagonal Checkerboard Surface and the PEC Ground Plane.

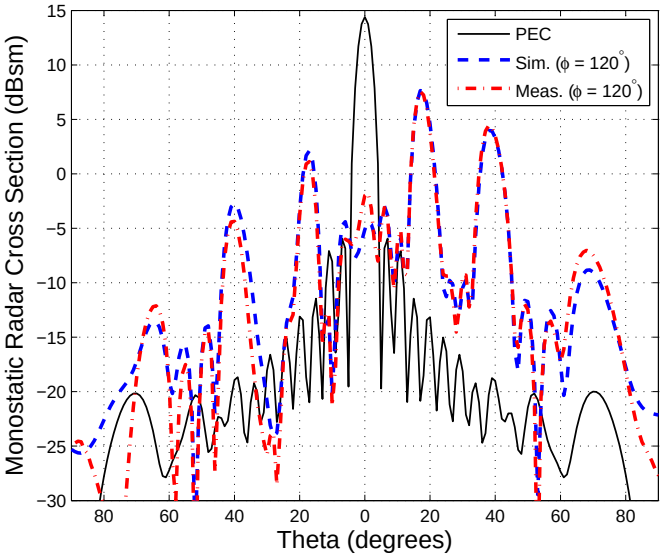

Fig. 5.15. Comparison of the Monostatic RCS at 7.5 GHz for TM^z Polarization along $\phi = 120^\circ$ Plane for the Hexagonal Checkerboard Surface and the PEC Ground Plane.

CHAPTER 6

DUAL BAND CHECKERBOARD SURFACES

This chapter introduces a dual-frequency band checkerboard surface with two dual-band EBG structures. It proves that the expression can also predict the 10-dB RCS reduction bandwidth for this more complex structure. Both normal incidence and oblique incidence are simulated and measured for this checkerboard surface design.

6.1. Introduction

Dual-band EBG structures, resonating at two different frequencies, are designed and demonstrated in this section. The first design (EBG1) consists of square loops and patches and the second design (EBG2) has circular loops and patches. This combination design of two different dual-band EBG structures on the same surface results in dual-band RCS reduction. In the EBG/PEC checkerboard surface, the reflection phase of the PEC is constant at 180° and the reflection phase of only one EBG structure can be controlled to optimize the overall frequency response of the entire surface. In contrast to the narrow band checkerboard surfaces combining EBG and PEC structures on the same ground plane, the proposed checkerboard surface of this paper obtains wider bandwidth because the reflection phase of each EBG structure can be adjusted/shifted, relative to each other, to optimize the bandwidth of the RCS reduction for the entire surface. Therefore, two different EBG surfaces, placed on the same ground plane, provide more degrees of freedom to optimize the resonant frequencies of the entire surface to yield wider RCS reduction bandwidth.

The unit cell of EBG1 is illustrated in Fig. 6.1. An infinite structure can be modelled and simulated by applying the proper symmetry planes around the unit cell [5]. The dimensions of the square loop of EBG1 are 12.0 mm x 12.0 mm with the strip width of 1.0

mm, while the square patch is 6.3 mm x 6.3 mm. Rogers RT/duroid 5880, with 2.2 dielectric constant and 6.35 mm thickness, is the selected substrate. The reflection magnitude and phase of the infinite array, as illustrated in Fig. 6.2, was simulated with Ansys HFSS. The phase of the reflection coefficient varies continuously from positive 180° to negative 180° in two frequency bands, which exhibit the resonant frequencies of 3.4 and 9.4 GHz, respectively.

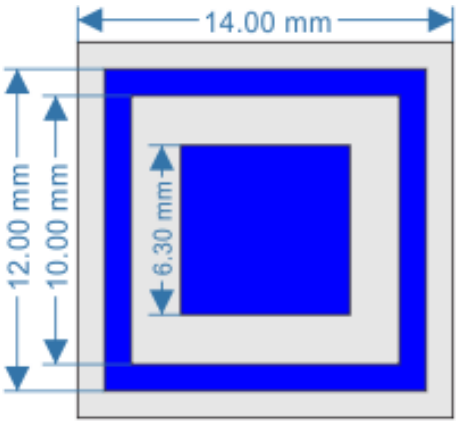

Fig. 6.1. Unit Cell of the EBG Structure with its Square Loop and Patch (EBG1).

The other EBG structure (EBG2) is shown in Fig. 6.3, and it consists of a circular patch inside a circular loop. The strip width of the circular loop is 0.5 mm with an outer radius of 4.5 mm, while the patch is 3.25 mm in radius. Thus, the gap between adjacent dual-band elements is 5.0 mm. The simulation approach is the same as that used for EBG1. The respective resonant frequencies of the corresponding patch are 5.9 and 10.9 GHz, as illustrated in Fig. 6.4.

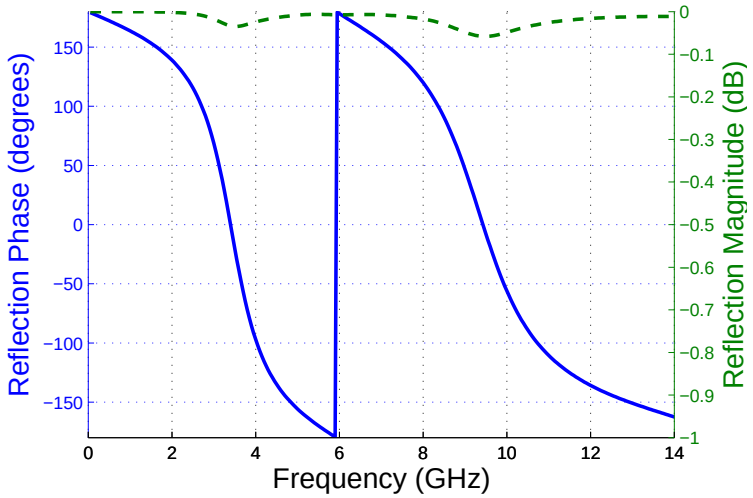

Fig. 6.2. Simulated Reflection Magnitude and Phase of EBG1 with its Square Loop and Patch.

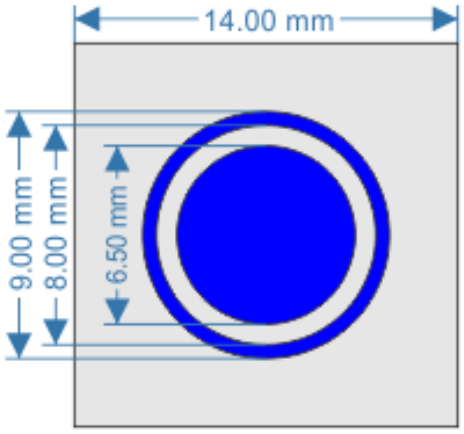

Fig. 6.3. Unit Cell of the EBG Structure with its Circular Loop and Patch (EBG2).

6.2. Analysis of Checkerboard Surfaces

The fields reflected from EBG1 are out-of-phase from those reflected by EBG2 at two frequencies, 4.6 GHz and 9.9 GHz, as shown in Fig. 6.6. At those two frequencies, the scattered fields are cancelled along the normal direction. This square checkerboard design cancels the scattered fields along the principal planes and redirects them towards the four

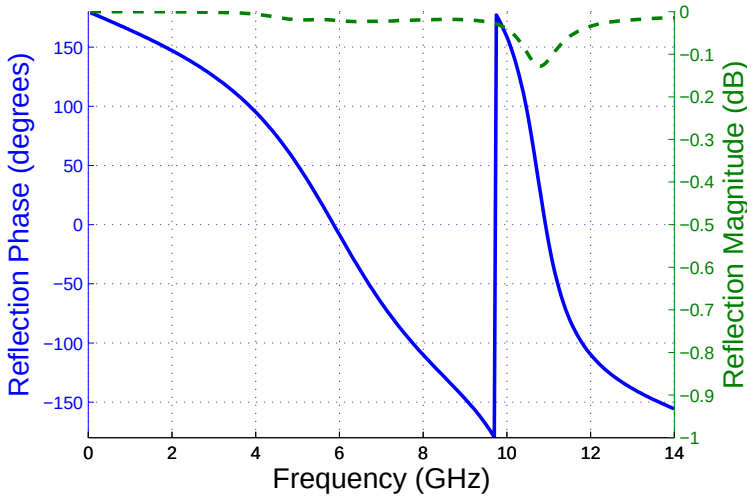

Fig. 6.4. Simulated Reflection Magnitude and Phase of EBG2 with its Circular Loop and Patch.

principal quadrants. The angle of the maximum bistatic scattering fields can be approximated by array theory [41]. Two dual-band EBG structures were designed to realize a four-quadrant dual-frequency band checkerboard surface, which is illustrated in Fig. 6.5. Patches of other geometries could be used to achieve the same RCS reduction performance, as long as they have the same reflection responses as EBG1 and EBG2. In those cases, the checkerboard surface ideally provides the same RCS reduction, which mainly depends on the phase difference between the reflection phases of the two EBGs.

An expression that approximates the 10-dB RCS reduction of a checkerboard surface, which was introduced in Chapter 4, is

$$\text{RCS Reduction} = 10\log\left[\frac{A_1 e^{jP_1} + A_2 e^{jP_2}}{2}\right]^2 \tag{6.1}$$

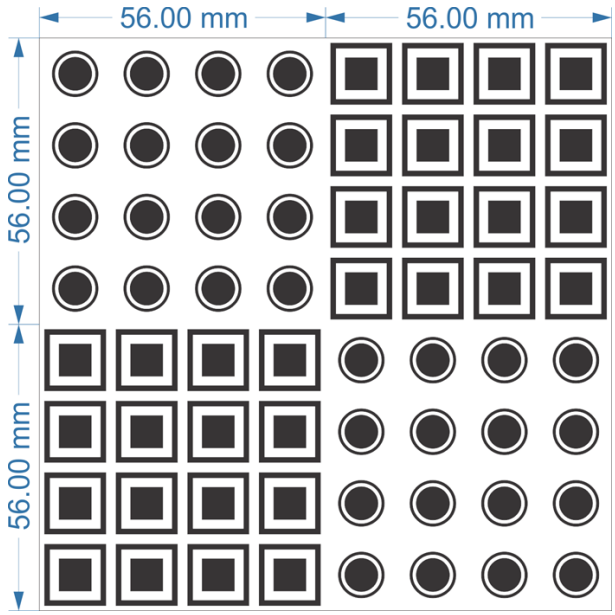

Fig. 6.5. Dual-Band Checkerboard Surface with 4x4 EBG1 and 4x4 EBG2.

where A_1 and A_2 are the reflection magnitudes of the two EBGs, and P_1 and P_2 are their reflection phases. Equation (6.1) serves as a guideline for predicting the 10-dB RCS reduction bandwidth of a checkerboard surface.

The predicted RCS reduction of the dual-band checkerboard surface of Fig. 6.5, using the analytical expression (6.1), is plotted in Fig. 6.8. It agrees well with measurements and simulations, and it predicts 10-dB RCS reductions of 63% and 23%, respectively, for the two frequency bands of 3.58 - 6.85 GHz and 8.56 - 10.73 GHz. These two bands correspond to 180 ± 37 degrees phase difference between EBG1 and EBG2, as shown in Fig. 6.6, and they match well with our simulations and measurements.

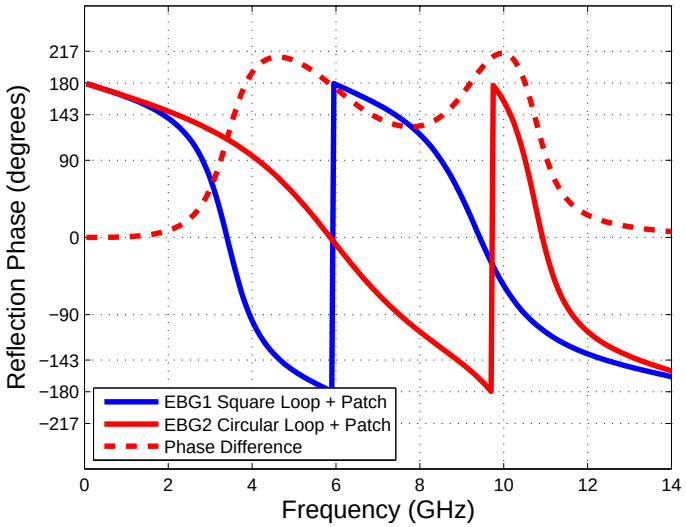

Fig. 6.6. Simulated Reflection Coefficient Phases of EBG1, EBG2 and Phase Difference between them.

6.3. Measurements and Simulations

A dual-band checkerboard surface of the design shown in Fig. 6.5 was designed, simulated and fabricated as depicted in Fig. 6.7; the overall dimensions are 112 mm x 112 mm. Its scattering patterns were measured at ASU's EMAC facility; the measurement setup is illustrated and discussed in [25]. Simulated and measured data of the dual-band checkerboard EBG surface of Fig. 6.7 are discussed in this section. Two-dimensional monostatic RCS patterns for both TE^z and TM^z polarization, as a function of frequency, are discussed in detail in subsection B. Since the magnitude of the reflection coefficient of a PEC surface is unity and the magnitude of the reflection coefficient of an EBG surface is also nearly unity, the predictions and comparisons of both designs are based on (6.1), which has been shown to predict the 10-dB RCS reduction quite accurately [25].

The checkerboard surface ground plane was simulated and measured, in terms of RCS reduction, over the frequencies from 2.0 to 14.0 GHz. The 10-dB RCS reduction, in the frequency bands of 3.94 - 7.40 GHz and 8.41 - 10.72 GHz, is of 61% and 24% bandwidths, respectively. Comparison between the simulation and measurement indicates a very good agreement, as illustrated in Fig. 6.8.

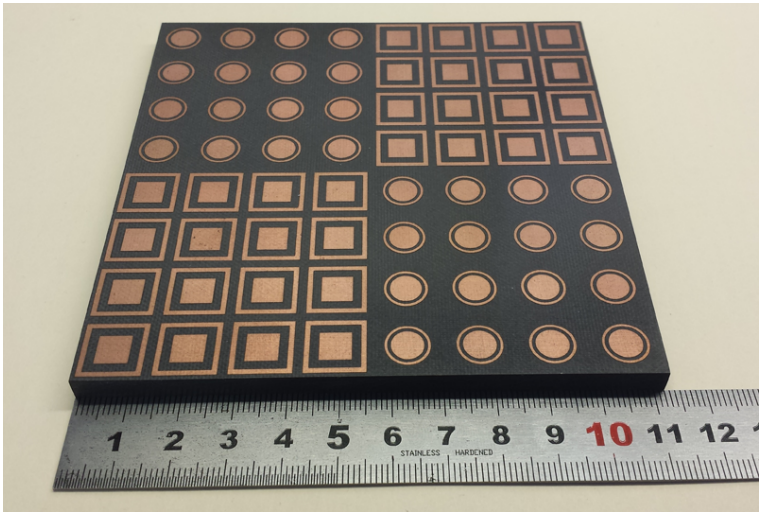

Fig. 6.7. Fabricated Dual-Band Checkerboard Surface.

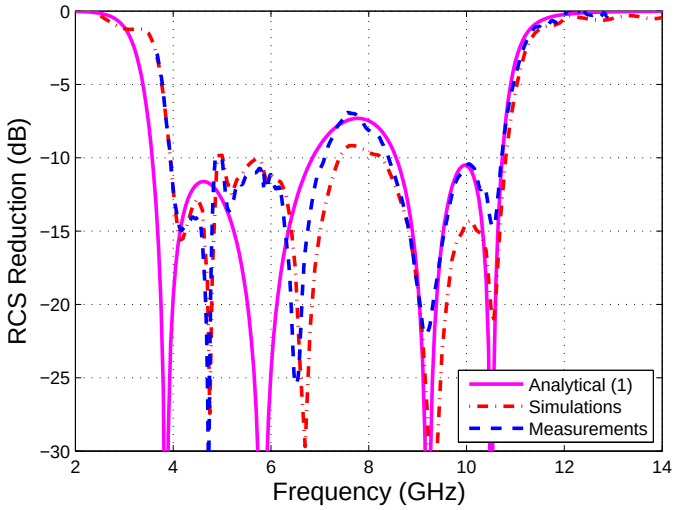

Fig. 6.8. RCS Reduction at Broadside Incidence for the Checkerboard Surface. Predicted 10-dB RCS Reduction Bandwidths using (6.1) are 63% and 23%. The Simulated RCS Reduction Bandwidths are 61% and 24%, and they are in Excellent Agreement with the Measured Ones of 57% and 24%.

6.3.1. *Bistatic RCS*

Under normal incidence at 6.5 GHz, the three dimensional bistatic RCS pattern of the checkerboard EBG surface of Fig. 6.7 is illustrated in Fig. 6.9, and exhibits main reflected lobes at $\phi = 45^\circ$, 135°, 225° and 315°. Comparison of the RCS between the checkerboard EBG surface and an equal-sized PEC surface were then performed. In the principal planes (*xz* and *yz* planes), the maximum RCS is reduced by 16.8 dB compared to the maximum of the corresponding PEC surface. The maxima of the RCS in the diagonal planes ($\phi = 45^\circ$ and 135°) are at $\theta = 24^\circ$. Due to the diffraction from the edges, the maximum is not exactly located at the angle of $\theta = 26^\circ$ predicted by array theory [41]. The maximum RCS of the four lobes in the diagonal planes is reduced by 5.2 dB compared to the maximum of the PEC surface. This is due to the redirection of the reflected fields in four directions along the diagonal planes, instead of a single lobe in the normal direction for the PEC surface. The two-dimensional comparison of the PEC and checkerboard surface is better illustrated by their bistatic patterns of Figs. 6.10 and 6.11, where the scattered fields are plotted versus the elevation angle.

Simulated three-dimensional bistatic scattering pattern of the checkerboard EBG surface of Fig. 6.7 at 5.2 GHz is shown in Fig. 6.12. Its two-dimensional patterns, as exhibited in Figs. 6.13 and 6.14, illustrate the comparison between the PEC surface and checkerboard EBG surface along the *xz*, *yz* planes and $\phi = 45^\circ$, 135° planes, respectively. Along the *xz* and *yz* planes, the maximum RCS is reduced by 11.5 dB compared to the maximum of the PEC surface. The maxima of the RCS are located at $\theta = 27^\circ, 35^\circ$ along the $\phi = 45^\circ$

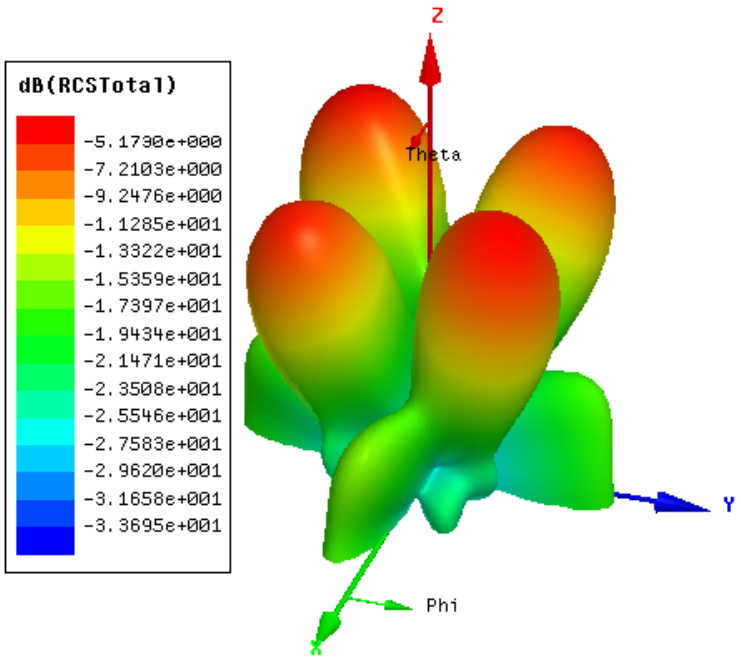

Fig. 6.9. Simulated Three-dimensional Bistatic RCS Pattern of the Checkerboard EBG Surface of Fig. 6.7 at 6.5 GHz at Broadside Incidence.

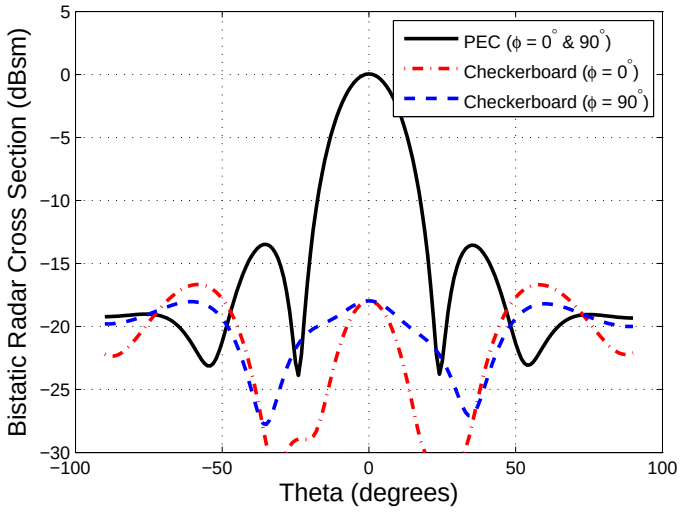

Fig. 6.10. Simulated Two-dimensional Bistatic RCS Patterns at 6.5 GHz along the *xz* and *yz* Planes for the PEC and Checkerboard EBG Surfaces.

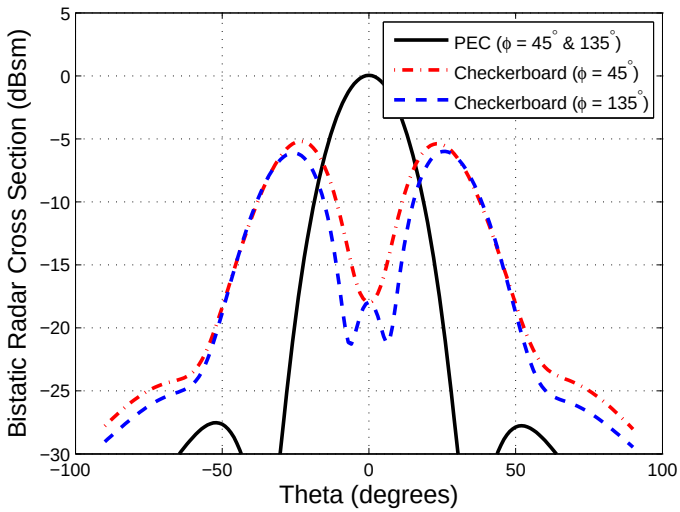

Fig. 6.11. Simulated Two-dimensional Bistatic RCS Patterns at 6.5 GHz along the $\phi = 45^\circ$ and 135° Planes for the PEC and Checkerboard EBG Surfaces.

and 135° planes, and are reduced by 5.1 dB and 7.1 dB compared to the maximum of the related PEC surface. The four main lobes do not divide perfectly into the same amplitude because the physical design geometry is not symmetrical along those two planes and also because of edge diffractions.

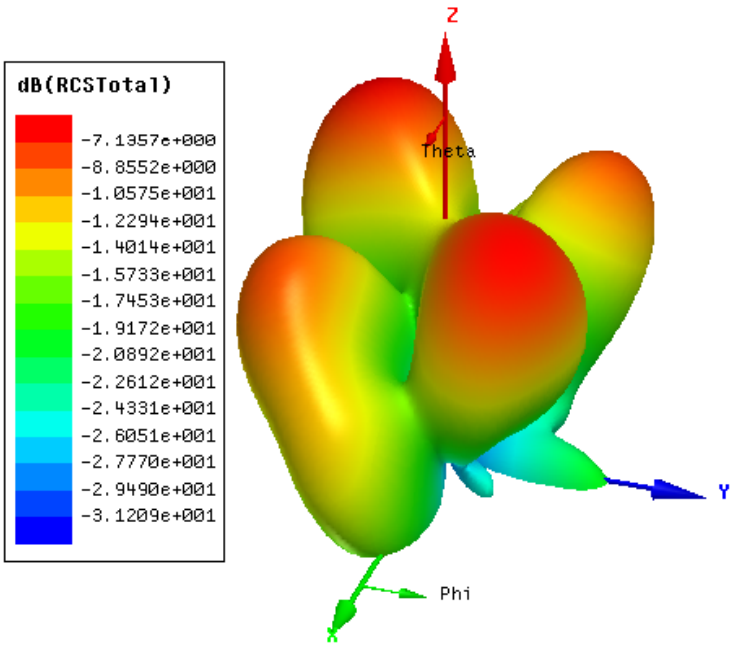

Fig. 6.12. Simulated Three-dimensional Bistatic RCS Pattern of the Checkerboard EBG Surface at 5.2 GHz at Broadside Incidence.

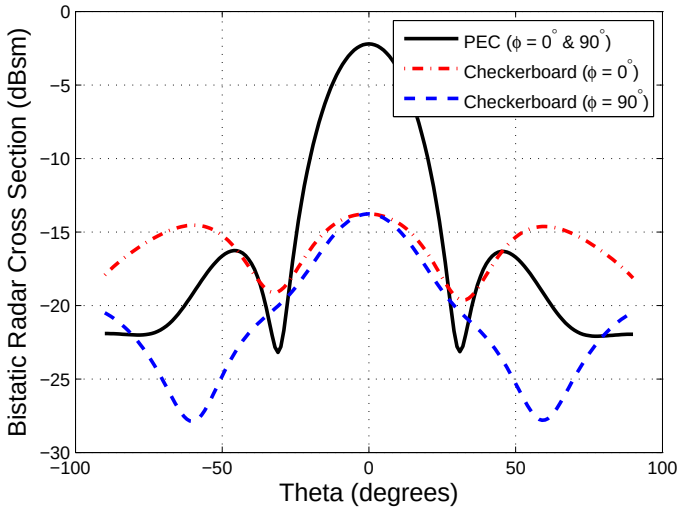

Fig. 6.13. Simulated Two-dimensional Bistatic RCS Patterns at 5.2 GHz along the *xz* and *yz* Planes for the PEC and Checkerboard EBG Surfaces.

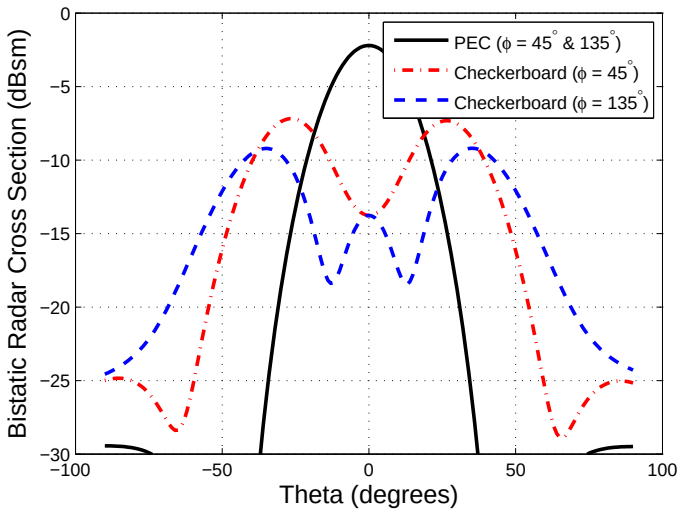

Fig. 6.14. Simulated Two-dimensional Bistatic RCS Patterns at 5.2 GHz along the $\phi = 45^\circ$ and 135° Planes for the PEC and Checkerboard EBG Surfaces.

6.3.2. *Monostatic RCS*

Because the reflection coefficient of an EBG structure varies with polarization and incident angle [42], it is advisable to investigate the performance under oblique incidence for the TE^z and TM^z polarizations. The two-dimensional monostatic RCS patterns of the checkerboard EBG surface of Fig. 6.7 at two different frequencies, 6.5 and 5.2 GHz, were simulated and measured for both TE^z and TM^z polarized fields. They are also compared with the monostatic RCS for the corresponding PEC surfaces. Those RCS patterns are illustrated and discussed in the sections that follow.

- TE^z Polarization

TE^z polarization two-dimensional monostatic RCS patterns at 6.5 GHz in the *xz* and *yz* planes, as illustrated in Fig. 6.15, indicate that the RCS in the normal direction is reduced by 22 dB compared to the maximum of the corresponding PEC surface. The maxima of the side lobes are reduced by 16.9 dB compared to the maximum of the corresponding PEC surface. The monostatic RCS patterns in the $\phi = 45^\circ$ and 135° planes, as illustrated in Fig. 6.16, show that the maxima of the four main scattered beams are directed at $\theta = 12^\circ$; this is due to the wave redirection by the checkerboard surface. Thus, the maxima of the four beams for the checkerboard surface are reduced by 5.8 dB compared to the maximum of the related PEC surface.

Similarly, the maxima of the scattered lobes at 5.2 GHz appear at $\theta = 18^\circ$ along the $\phi = 45^\circ$ and 135° planes, and the maxima for the checkerboard surface are reduced by 5.3 dB. The RCS maxima in the *xz* and *yz* planes are reduced by 10.9 dB compared to the

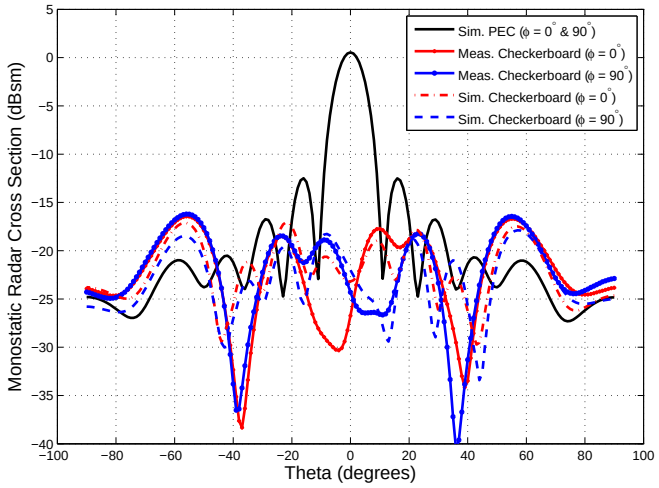

Fig. 6.15. TE^z Polarization Two-dimensional Simulated and Measured Monostatic RCS Patterns along the *xz* and *yz* Planes for the PEC and Checkerboard EBG Surfaces at 6.5 GHz.

maximum of the related PEC surface. The two-dimensional monostatic RCS patterns along the *xz*, *yz* planes and $\phi = 45^\circ$, 135° planes are shown in Figs. 6.17 and 6.18, respectively.

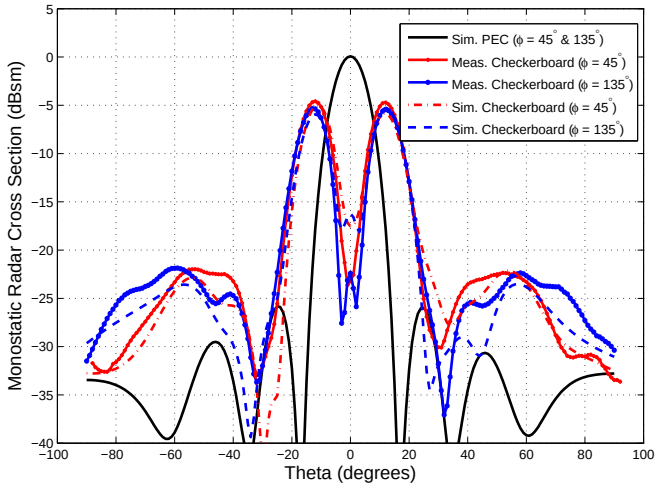

Fig. 6.16. TE^z Polarization Two-dimensional Simulated and Measured Monostatic RCS Patterns along the $\phi = 45°$ and 135° Planes for the PEC and Checkerboard EBG Surfaces at 6.5 GHz.

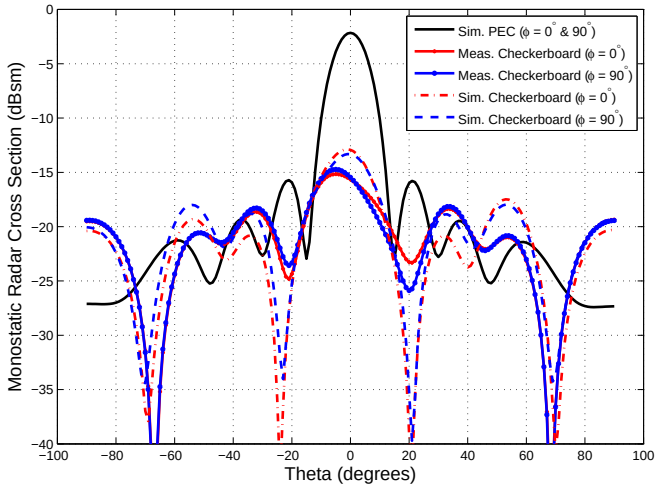

Fig. 6.17. TE^z Polarization Two-dimensional Simulated and Measured Monostatic RCS Patterns along the *xz* and *yz* Planes for the PEC and Checkerboard EBG Surfaces at 5.2 GHz.

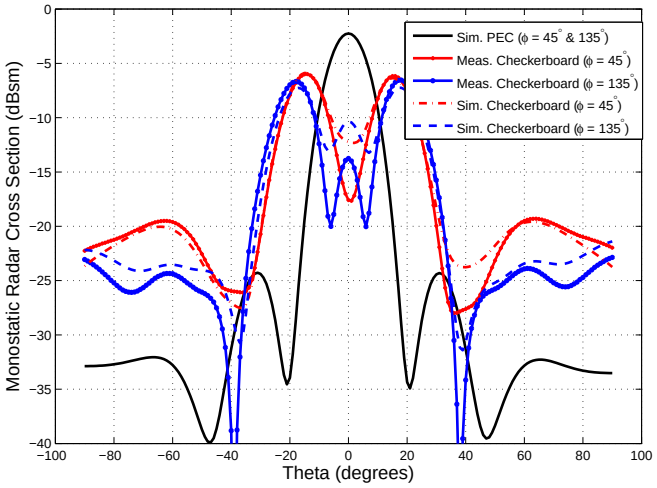

Fig. 6.18. TE^z Polarization Two-dimensional Simulated and Measured Monostatic RCS Patterns along the $\phi = 45^\circ$ and 135° Planes for the PEC and Checkerboard EBG Surfaces at 5.2 GHz.

- TM^z Polarization

Two-dimensional monostatic RCS patterns for the TM^z polarization at 6.5 GHz, for the xz and yz planes and $\phi = 45^\circ$ and 135° planes, are displayed in Figs. 6.19 and 6.20, respectively. The patterns illustrate that the maxima of the scattered fields are reduced by 14.2 dB compared to the maximum of the corresponding PEC surface along the xz and yz planes, while the four main reflected lobes are directed at $\theta = 12^\circ$ in the $\phi = 45^\circ$ and 135° planes. In addition, the maxima for the checkerboard surface are reduced by 5.0 dB compared to the maximum of the related PEC surface.

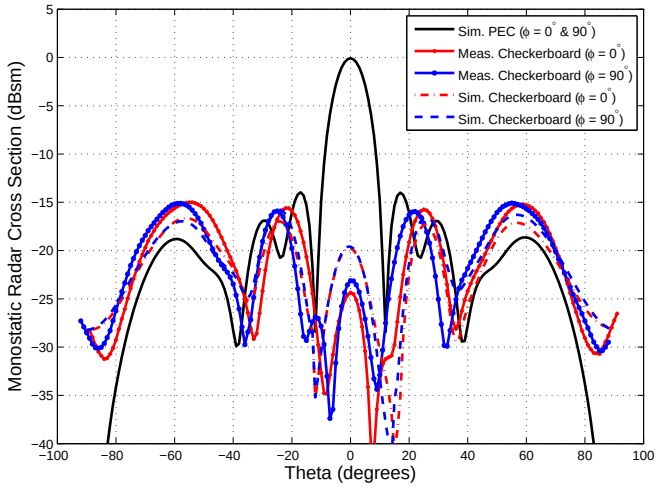

Fig. 6.19. TM^z Polarization Two-dimensional Simulated and Measured Monostatic RCS Patterns along the xz and yz Planes for the PEC and Checkerboard EBG Surfaces at 6.5 GHz.

From the two-dimensional monostatic RCS patterns at 5.2 GHz, as illustrated in Figs. 6.21 and 6.22, it is observed that the RCS maximum is reduced by 13.0 dB compared to the maximum of the related PEC surface along the xz and yz planes. The four main scattered

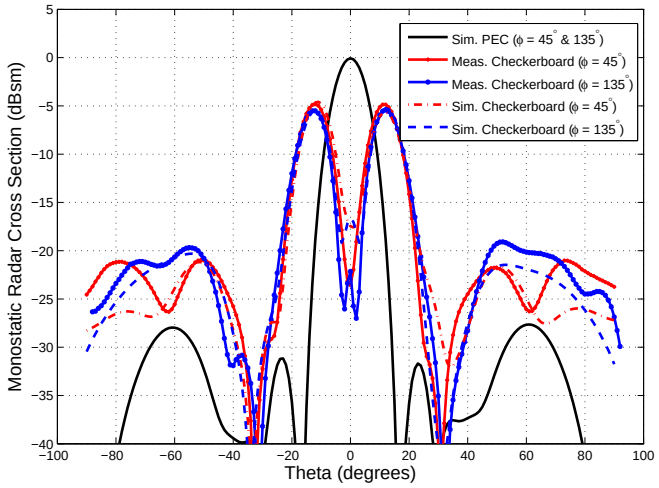

Fig. 6.20. TM^z Polarization Two-dimensional Simulated and Measured Monostatic RCS Patterns along the $\phi = 45^\circ$ and 135° Planes for the PEC and Checkerboard EBG Surfaces at 6.5 GHz.

lobes are directed at $\theta = 18^\circ$ along the $\phi = 45^\circ$ and 135° planes, while the RCS maxima are reduced by 5.1 dB compared to the maximum of the corresponding PEC surface.

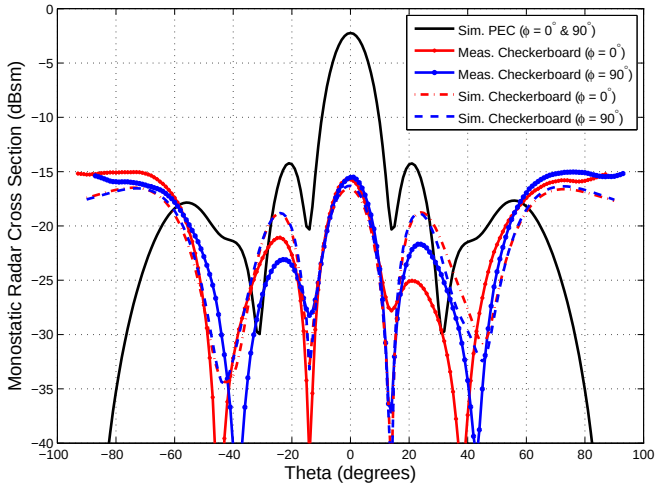

Fig. 6.21. TM^z Polarization Two-dimensional Simulated and Measured Monostatic RCS Patterns along the *xz* and *yz* Planes for the PEC and Checkerboard EBG Surfaces at 5.2 GHz.

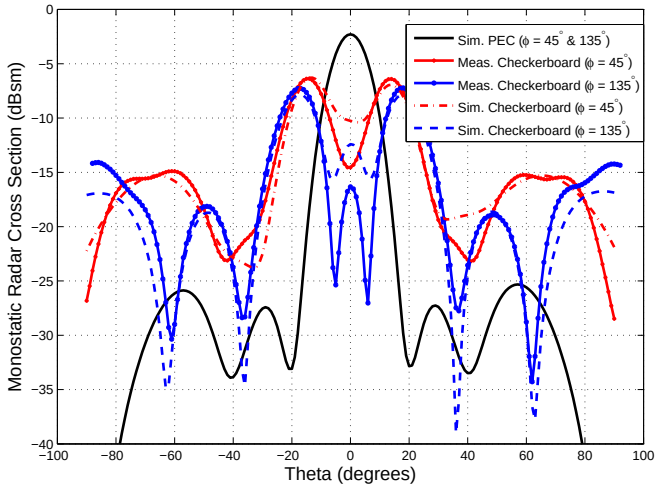

Fig. 6.22. TM^z Polarization Two-dimensional Simulated and Measured Monostatic RCS Patterns along the $\phi = 45^\circ$ and 135° Planes for the PEC and Checkerboard EBG Surfaces at 5.2 GHz.

CHAPTER 7

CYLINDRICALLY CURVED CHECKERBOARD SURFACES

This chapter proposes cylindrically curved checkerboard surfaces on cylindrically curved ground planes. The RCS of cylindrical checkerboard surfaces are examined for three different radii of curvature. Both narrow and wide band curved checkerboard surfaces are evaluated by simulations and measurements under normal incidence for horizontal and vertical polarizations.

7.1. Introduction

This chapter extends and applies checkerboard surfaces for RCS reduction on cylindrically curved ground planes. Design, fabricate, simulate, measure and compare the performance of narrow and wide band cylindrical checkerboard surfaces are performed. A physical interpretation of the bistatic scattering patterns is provided, and the simulated monostatic scattering frequency responses are compared with measurements.

The cylindrically curved checkerboard surfaces are designed using the following procedure. First, each EBG structure is designed on a flat surface. Then, combining different EBG/PEC structures on the same surface completes the flat checkerboard design. The flat checkerboard surfaces are then imported to the curved surface of cylinders with different radii of curvature to realize cylindrically curved checkerboard surfaces. The curved checkerboard surfaces are simulated and measured for monostatic, and simulated for bistatic, scattering. Finally, the bandwidth of the monostatic RCS reduction is examined and compared, and it is based on the corresponding cylindrical PEC surfaces. The same procedure applies to both narrow and wide band checkerboard surfaces.

A narrow band checkerboard surface is designed by combining PEC and EBG structures on the same surface. The EBG structure is designed with periodic square patches on Rogers RO3003 substrate, with the bottom surface of the substrate being PEC. The period of the EBG structure is 10.0 mm x 10.0 mm, which includes a patch of 9.0 mm x 9.0 mm and a gap of 1.0 mm. The substrate thickness is 1.52 mm and the dielectric constant is 3.0. The phase and magnitude of the reflection coefficient of the infinite unit cell array were simulated using Ansys HFSS and are illustrated in Fig. 7.1. The 0° reflection phase occurs at the resonant frequency of 7.1 GHz. The magnitude of the reflection coefficient at the resonant frequency is -0.1 dB due to dielectric and radiation losses.

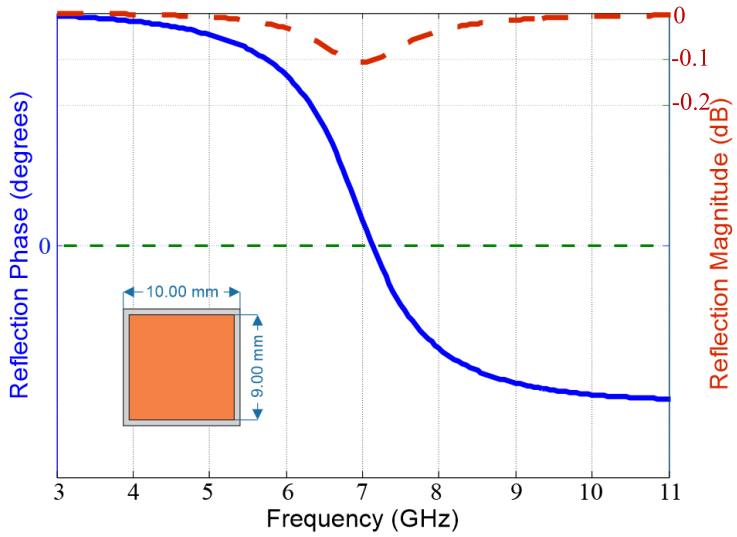

Fig. 7.1. Reflection Coefficient of the EBG Structure with its Square Patches.

After the reflection coefficient is simulated, the RCS reduction of the checkerboard surface can be predicted by (7.1), as detailed in [25], over the frequency band of 5 - 9 GHz. The RCS reduction maximum is more than 30 dB at 7.1 GHz, while the RCS is reduced by

more than 10 dB in the frequency band of 6.8 - 7.4 GHz; thus, the 10-dB RCS reduction bandwidth is 8% and it is illustrated in Fig. 7.2.

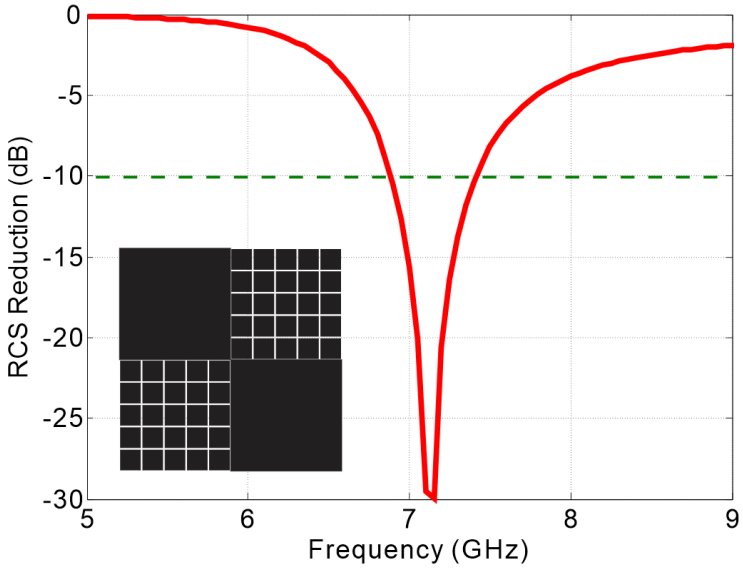

Fig. 7.2. Predicted RCS Reduction Bandwidth is 8% for the Narrow Band Checkerboard Surface.

$$\text{RCS Reduction} = 10\log\left[\frac{A_1 e^{jP_1} + A_2 e^{jP_2}}{2}\right]^2 \tag{7.1}$$

where A_1 and A_2 are the reflection coefficient magnitudes of the two EBG structures, and P_1 and P_2 are their reflection phases.

Another design, a wide band checkerboard surface, consisting of two alternating EBG structures (EBG1 and EBG2) is also considered. When the PEC fields of the narrow band checkerboard are replaced with a judiciously designed EBG structure, the bandwidth of the resulting checkerboard is significantly enhanced. The EBG structure with square patches is the same design as the one for the narrow band checkerboard surface. The second EBG

structure is designed with circular patches of 4.5 mm radius and 1.0 mm gap between the adjacent patches. The substrate is also the same, Rogers RO3003. The reflection phase and magnitude were simulated, and they are displayed in Fig. 7.3 which indicates a resonant frequency of 9.5 GHz and an associated reflection magnitude of -0.08 dB.

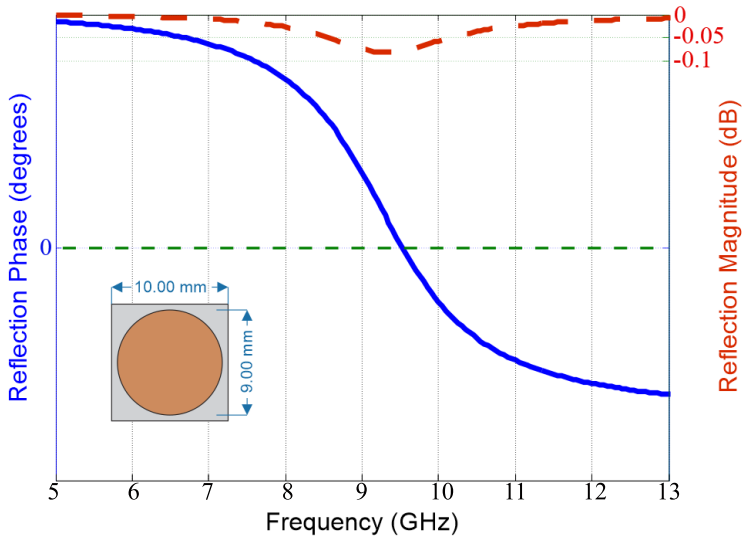

Fig. 7.3. Reflection Coefficient of the EBG Structure with its Circular Patches.

The RCS reduction of this wide band checkerboard surface has also been predicted by (7.1) over 5 - 11 GHz, once the reflection coefficients of the two EBGs are simulated, and it is illustrated in Fig. 7.4. The RCS reduction maximum is more than 30 dB at 7.3 and 8.9 GHz, while the bandwidth of 10-dB RCS reduction is about 27% (7.0 - 9.2 GHz).

For simplicity of fabrication, both narrow band and wide band checkerboard surfaces are designed to contain 4 x 4 EBG sections, as introduced in [25]. Each EBG section contains 5 x 5 unit cells. The design principle is based on array theory [41]. The equal-sized EBG structures are placed alternately one after another. The dimensions of the entire

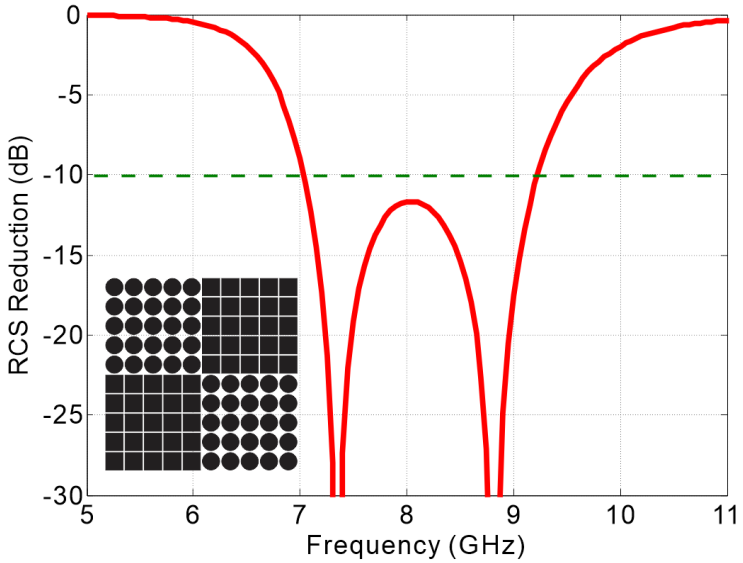

Fig. 7.4. Predicted RCS Reduction Bandwidth is 27% for the Narrow Band Checkerboard Surface.

checkerboard surfaces are 200 mm x 200 mm. The substrate of RO3003 was chosen because of its flexibility and availability. The fabricated checkerboard surfaces are used for measurements of three different radii of curvature, 10λ, 5λ and 3λ; the measurement setup is detailed in [25]. The geometries of the cylindrical checkerboard surfaces are shown within the 3-D RCS pattern figures in the next section, for their corresponding radii of curvature.

7.2. Performance of Cylindrically Curved Checkerboard Surfaces

Simulations and measurements of the narrow and wide band cylindrically curved checkerboard surfaces are compared with the corresponding cylindrically curved PEC surfaces and presented in this section. The monostatic backscattering under normal incidence is discussed for HH and VV polarizations. The simulated 3-D bistatic RCS patterns are also

illustrated. It is noted that for the HH polarization the electric field of the incident wave is along the x-axis (parallel to the plane of curvature, XY) while for the VV polarization the electric field is along the z-axis (perpendicular to the plane of curvature, XY), referring to the coordinate system of Fig. 7.7.

7.2.1. *Narrow Band Design*

The narrow band cylindrically curved checkerboard surface with a radius of curvature of 10λ (radius = 420 mm) is simulated and measured. A fabricated prototype is depicted in Fig. 7.5. Comparisons of the measured and simulated monostatic RCS reduction are illustrated in Figs. 7.6 and 7.8, for HH and VV polarizations, respectively. A good agreement is obtained for both polarizations. The RCS reduction is based on the corresponding curved PEC surfaces, and the 10-dB reduction bandwidth is 8%. The 3-D bistatic simulated RCS patterns at 7.0 GHz for HH and VV polarizations are displayed in Figs. 7.7 and 7.9, respectively. Under normal incidence, the RCS is dramatically reduced along the principal planes (YZ and XY planes). Eight main reflected lobes appear (four on each side of the XY plane), because the axis of the cylindrically curved checkerboard surface is along the z-axis. The separation angle between the two adjacent inner most lobes along the plane of curvature (XY plane) is 36°.

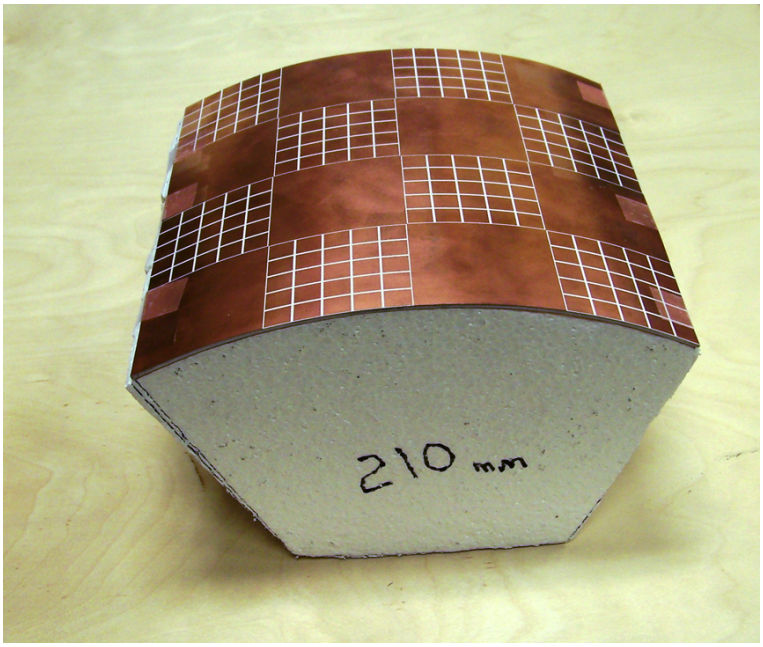

Fig. 7.5. Fabricated Narrow Band Cylindrically Curved Checkerboard EBG Surface.

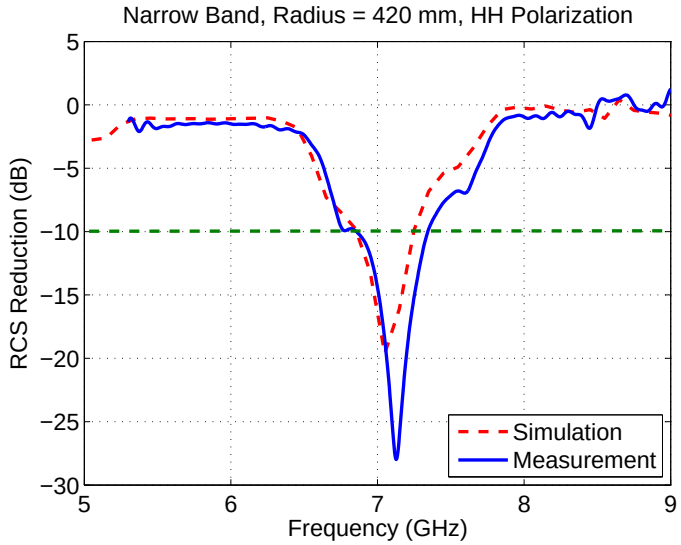

Fig. 7.6. Simulated and Measured Narrow Band RCS Reduction for HH Polarization under Normal Incidence. The Radius of Curvature is 10λ.

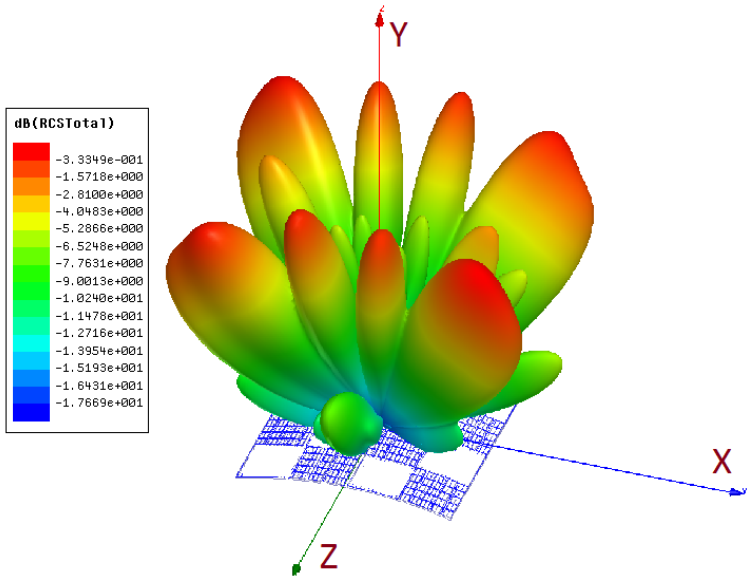

Fig. 7.7. 3-D Bistatic Simulated RCS Pattern at 7.0 GHz for HH Polarization under Normal Incidence. The Radius of Curvature is 10λ. The Separation Angle between the Center Two Lobes along the Plane of Curvature (XY Plane) is 36°.

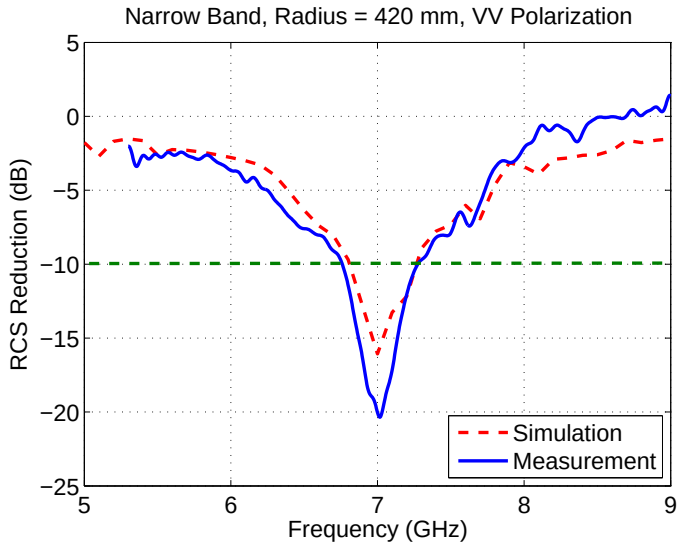

Fig. 7.8. Simulated and Measured Narrow Band RCS Reduction for VV Polarization under Normal Incidence. The Radius of Curvature is 10λ.

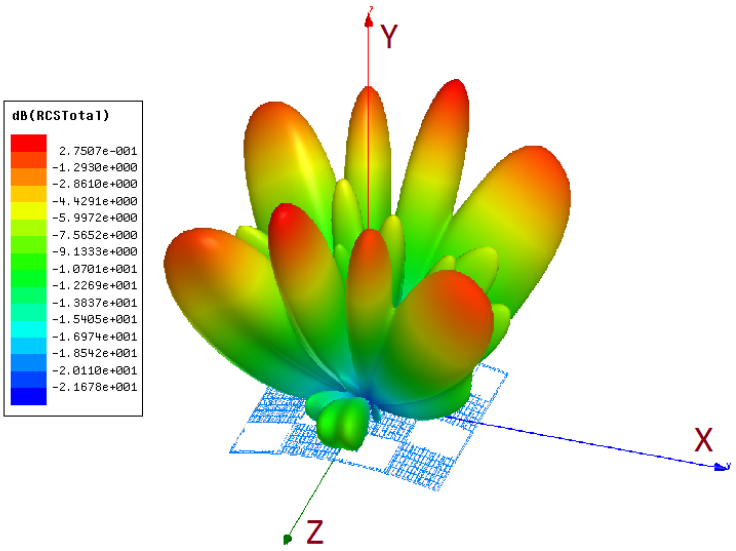

Fig. 7.9. 3-D Bistatic Simulated RCS Pattern at 7.0 GHz for VV Polarization under Normal Incidence. The Radius of Curvature is 10λ. The Separation Angle between the Center Two Lobes along the Plane of Curvature (XY Plane) is 36°.

The next design is the checkerboard surface with a radius of curvature of 5λ (radius = 210 mm), for which comparisons of the measured and simulated monostatic RCS reduction are illustrated in Figs. 7.10 and 7.12, for HH and VV polarizations, respectively. The 10-dB RCS reduction bandwidth is 7%. There is a good agreement for both polarizations. The 3-D bistatic simulated RCS patterns at 7.2 GHz for HH and VV polarizations are illustrated in Figs. 7.11 and 7.13, respectively. The separation angle between the two adjacent inner most lobes along the plane of curvature (XY plane) is 58°, which is larger than that for the checkerboard surface of 10λ curvature. This is expected since, based on geometrical optics, the separation angle is inversely proportional to the radius of curvature.

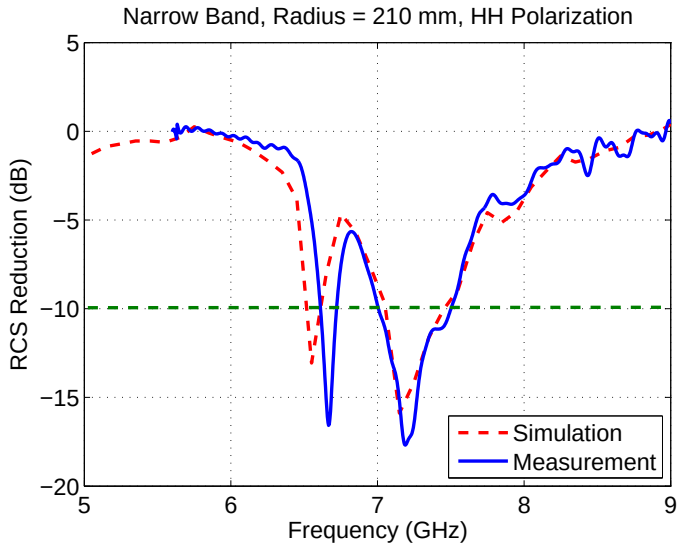

Fig. 7.10. Simulated and Measured Narrow Band RCS Reduction for HH Polarization under Normal Incidence. The Radius of Curvature is 5λ.

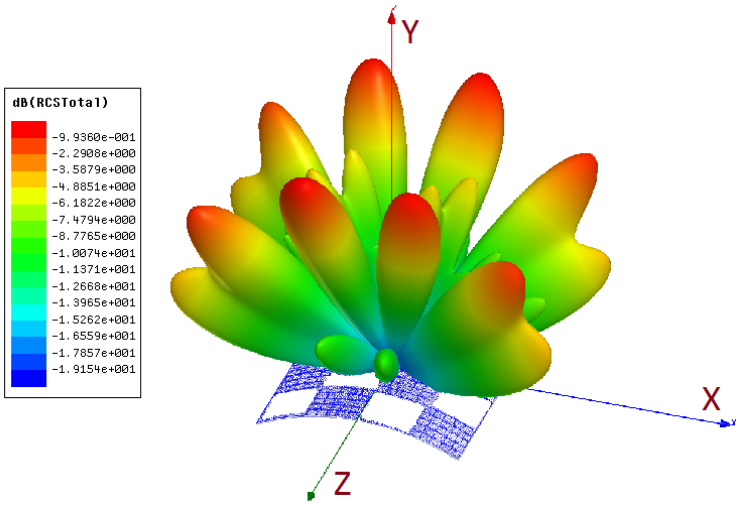

Fig. 7.11. 3-D Bistatic Simulated RCS Pattern at 7.2 GHz for HH Polarization under Normal Incidence. The Radius of Curvature is 5λ. The Separation Angle between the Center Two Lobes along the Plane of Curvature (XY Plane) is 58°.

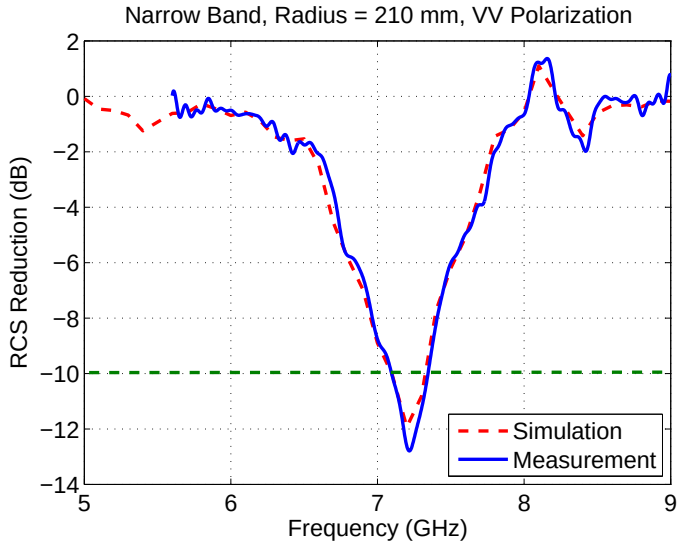

Fig. 7.12. Simulated and Measured Narrow Band RCS Reduction for VV Polarization under Normal Incidence. The Radius of Curvature is 5λ.

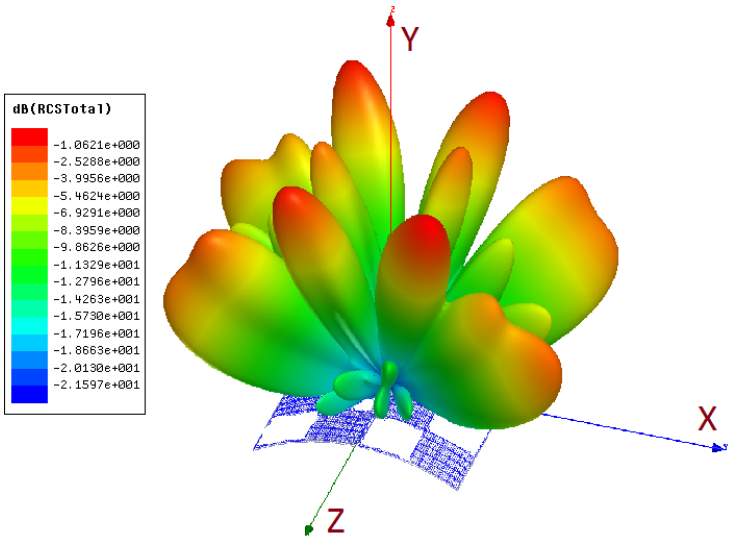

Fig. 7.13. 3-D Bistatic Simulated RCS Pattern at 7.2 GHz for VV Polarization under Normal Incidence. The Radius of Curvature is 5λ. The Separation Angle between the Center Two Lobes along the Plane of Curvature (XY Plane) is 58°.

Comparisons of the measured and simulated monostatic RCS reduction for the curved checkerboard surface with a radius of curvature of 3λ (radius = 126 mm) are illustrated in Figs. 7.14 and 7.16, for HH and VV polarizations, respectively. The agreement between simulated and measured patterns is good. The RCS reduction bandwidth is 8% for VV polarization. However, it is difficult to achieve the 10-dB RCS reduction for HH polarization because a minor lobe is directed along the normal direction, as illustrated in Fig. 7.15. The appearance of the side lobe at the normal direction can be attributed to the effects of the AGSWs. The 3-D bistatic simulated RCS pattern at 7.1 GHz for VV polarization, illustrated in Fig. 7.17, clearly displays four main lobes. The separation angle between the two adjacent inner most lobes is 82°. As expected, due to geometrical optics, the separation angle between the center two lobes increases with decreasing radius.

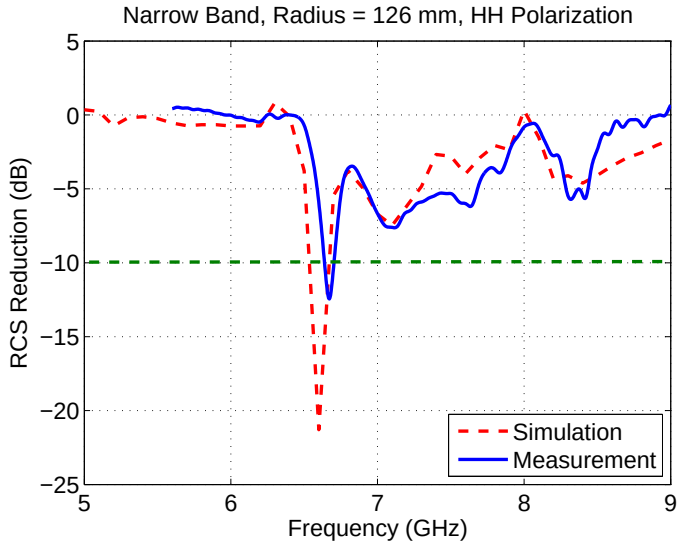

Fig. 7.14. Simulated and Measured Narrow Band RCS Reduction for HH Polarization under Normal Incidence. The Radius of Curvature is 3λ.

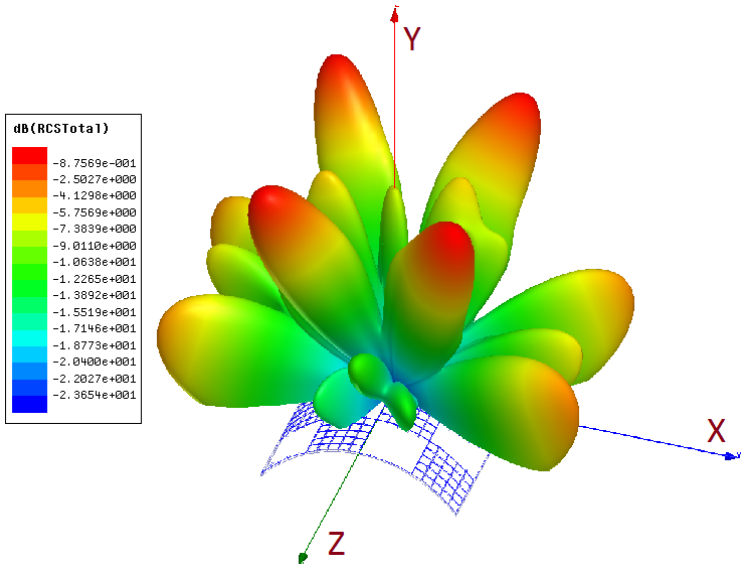

Fig. 7.15. 3-D Bistatic Simulated RCS Pattern at 7.1 GHz for HH Polarization under Normal Incidence. The Radius of Curvature is 3λ. The Separation Angle between the Center Two Lobes along the Plane of Curvature (XY Plane) is 82°.

BW / Angle	10 λ	5 λ	3 λ
Horizontal Polarization	8% / 36°	7% / 58°	0% / 82°
Vertical Polarization	8% / 36°	5% / 58°	8% / 82°

Table 7.1. Summary of Bandwidth and Separation Angle between the Center Two Lobes for the Narrow Band Cylindrically Curved Checkerboard Surface.

A summary of 10-dB RCS reduction bandwidth and separation angle between the center two lobes for the narrow band cylindrically curved checkerboard surface is listed in Table 7.1.

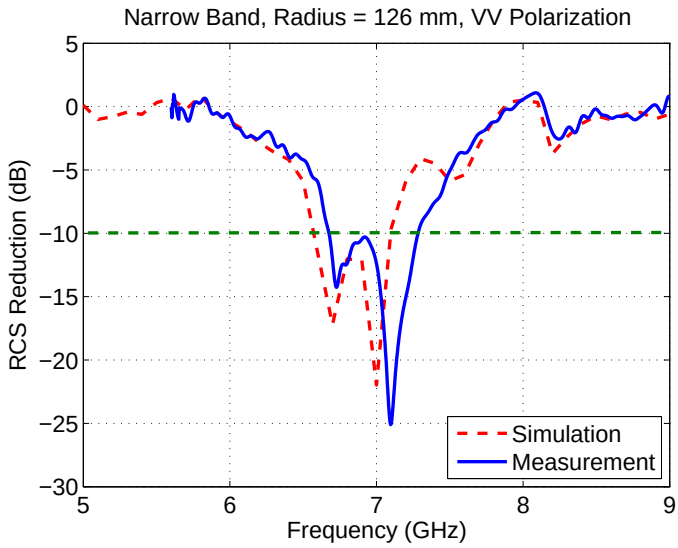

Fig. 7.16. Simulated and Measured Narrow Band RCS Reduction for VV Polarization under Normal Incidence. The Radius of Curvature is 3λ.

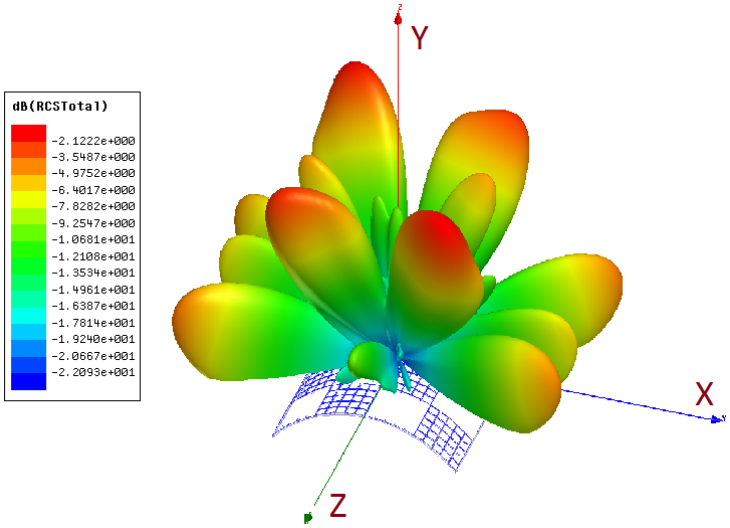

Fig. 7.17. 3-D Bistatic Simulated RCS Pattern at 7.1 GHz for VV Polarization under Normal Incidence. The Radius of Curvature is 3λ. The Separation Angle between the Center Two Lobes along the Plane of Curvature (XY Plane) is 82°.

7.2.2. *Wide Band Design*

The wide band cylindrically curved checkerboard surface with three different radii of curvature are examined and presented in this section. The RCS reduction of the checkerboard design with a radius of curvature of 10λ is simulated, measured, and compared. A prototype of the fabricated wide band design is depicted in Fig. 7.18. The results, illustrated in Figs. 7.19 and 7.21 for HH and VV polarizations, respectively, illustrate that the 10-dB RCS reduction bandwidth is 9%. The 3-D bistatic RCS patterns are simulated at 7.9 GHz for HH and VV polarizations, and they are displayed in Figs. 7.20 and 7.22, respectively. Four main reflected lobes appear at each side of the XY plane. The separation angle between the two adjacent inner most lobes along the plane of curvature is 40°.

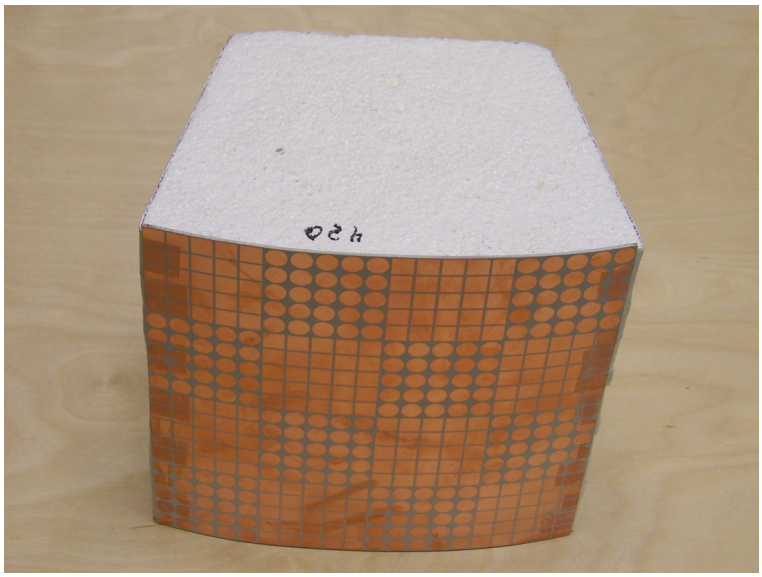

Fig. 7.18. Fabricated Wide Band Cylindrically Curved Checkerboard EBG Surface.

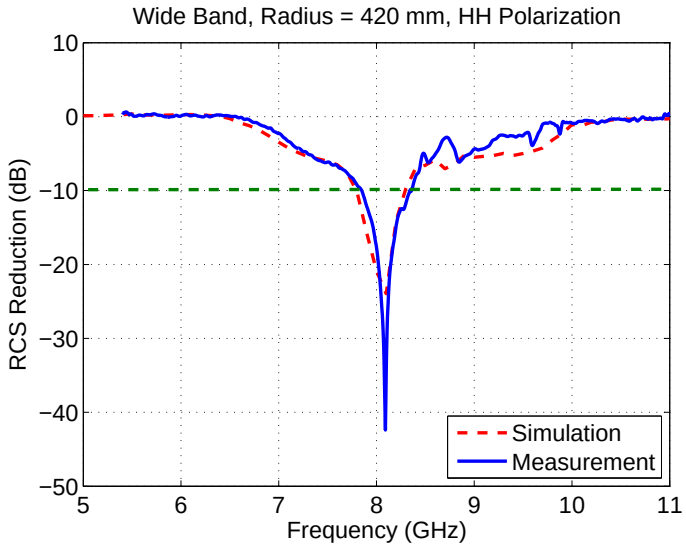

Fig. 7.19. Simulated and Measured Wide Band RCS Reduction for HH Polarization under Normal Incidence. The Radius of Curvature is 10λ.

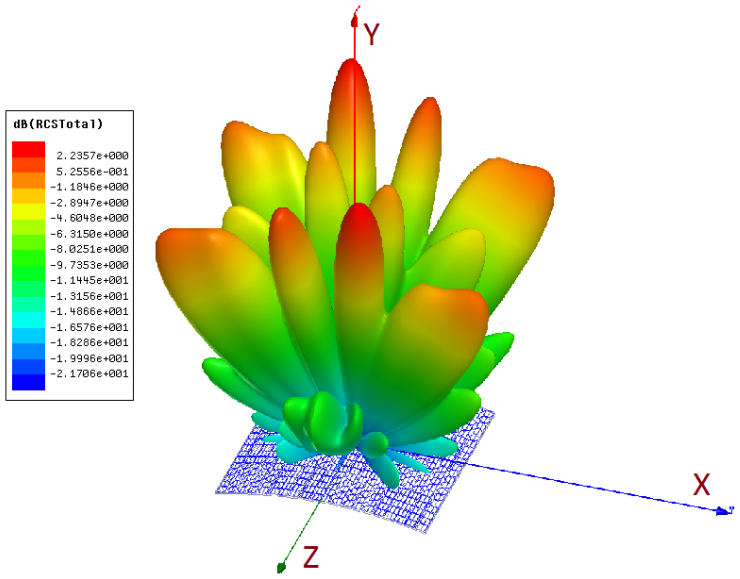

Fig. 7.20. 3-D Bistatic Simulated RCS Pattern at 8.0 GHz for HH Polarization under Normal Incidence. The Radius of Curvature is 10λ. The Separation Angle between the Center Two Lobes along the Plane of Curvature (XY Plane) is 40°.

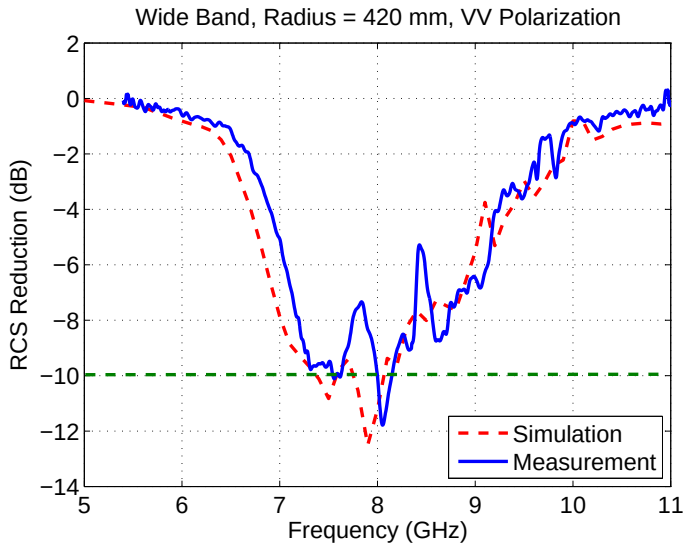

Fig. 7.21. Simulated and Measured Wide Band RCS Reduction for VV Polarization under Normal Incidence. The Radius of Curvature is 10λ.

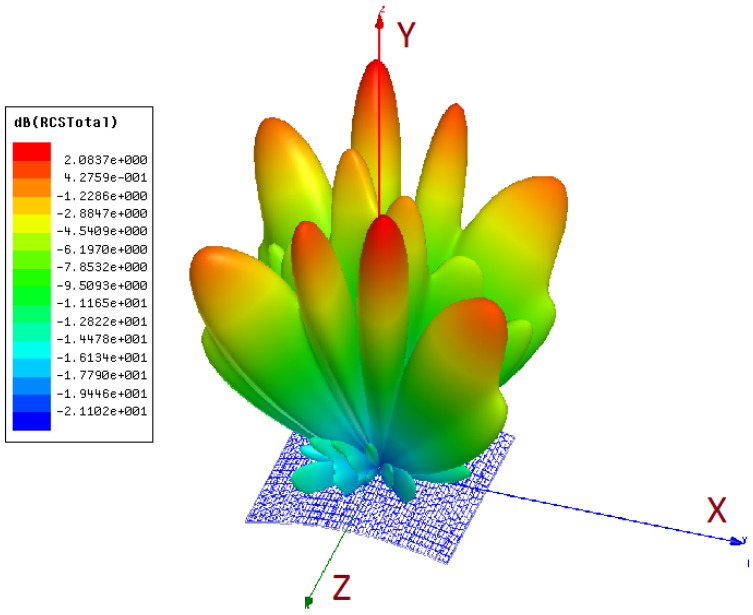

Fig. 7.22. 3-D Bistatic Simulated RCS Pattern at 7.9 GHz for VV Polarization under Normal Incidence. The Radius of Curvature is 10λ. The Separation Angle between the Center Two Lobes along the Plane of Curvature (XY Plane) is 40°.

For the second design, 5λ curvature, the measured and simulated RCS reduction plots are illustrated in Figs. 7.23 and 7.25 for HH and VV polarizations, respectively, and the 10-dB RCS reduction bandwidth is 22%. The 3-D bistatic simulated RCS patterns at 8.2 GHz for HH and VV polarizations are displayed in Figs. 7.24 and 7.26, respectively. As expected, the separation angle between the two adjacent inner most lobes is 52°, and it is larger than that for 10λ curvature.

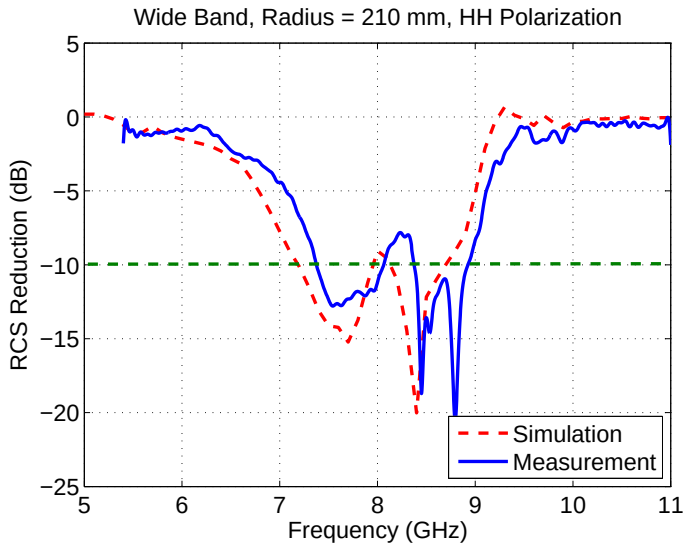

Fig. 7.23. Simulated and Measured Wide Band RCS Reduction for HH Polarization under Normal Incidence. The Radius of Curvature is 5λ.

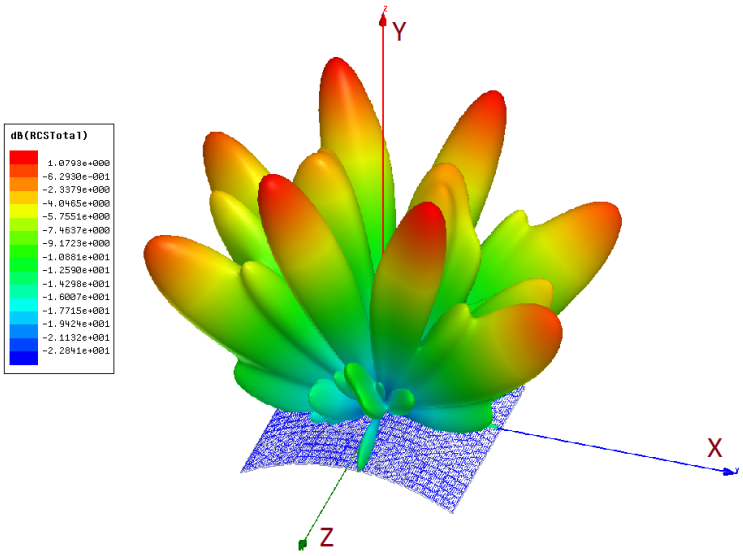

Fig. 7.24. 3-D Bistatic Simulated RCS Pattern at 8.4 GHz for HH Polarization under Normal Incidence. The Radius of Curvature is 5λ. The Separation Angle between the Center Two Lobes along the Plane of Curvature (XY Plane) is 52°.

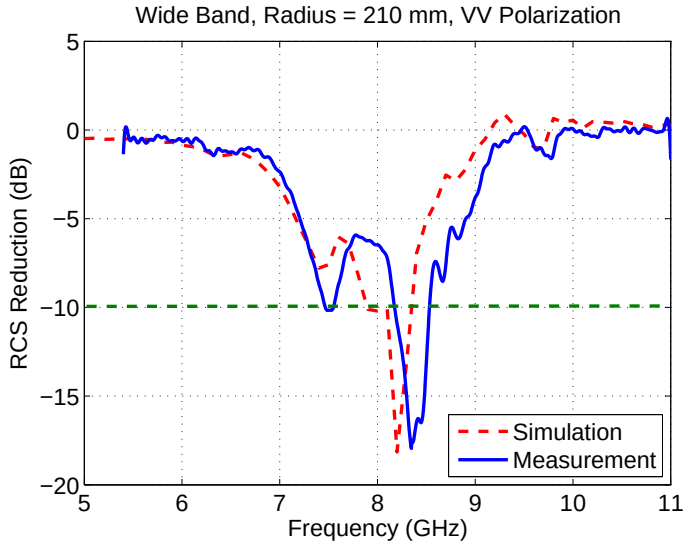

Fig. 7.25. Simulated and Measured Wide Band RCS Reduction for VV Polarization under Normal Incidence. The Radius of Curvature is 5λ.

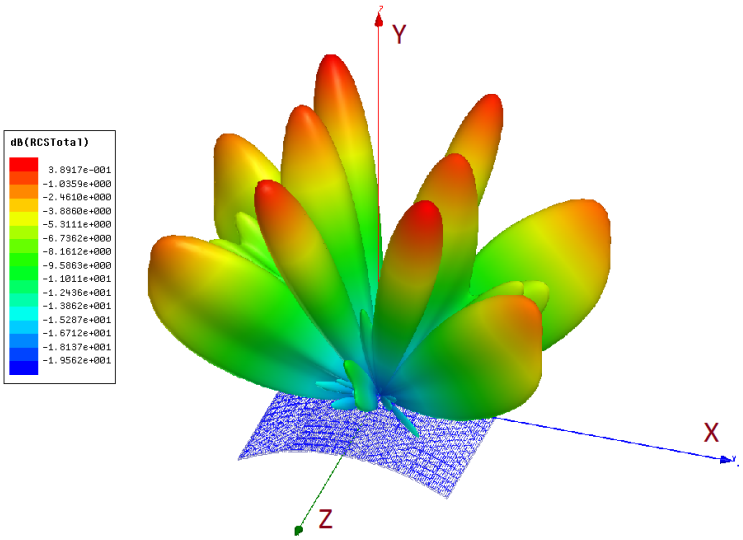

Fig. 7.26. 3-D Bistatic Simulated RCS Pattern at 8.2 GHz for VV Polarization under Normal Incidence. The Radius of Curvature is 5λ. The Separation Angle between the Center Two Lobes along the Plane of Curvature (XY Plane) is 76°.

Figs. 7.27 and 7.29 display the data for the 3λ curved surface, for HH and VV polarizations, respectively, and the monostatic RCS reduction bandwidth is 20% for VV polarization. However, it barely reaches the 10-dB RCS reduction for HH polarization because a minor lobe is directed along the normal direction, due to the presence of AGSWs on the surface, as illustrated in Fig. 7.28. The 3-D bistatic simulated RCS pattern at 8.4 GHz for VV polarization is illustrated in Fig. 7.30. The separation angle between the two lobes along the plane of curvature is 48° for VV polarization, because the minor lobes appear closer to the center.

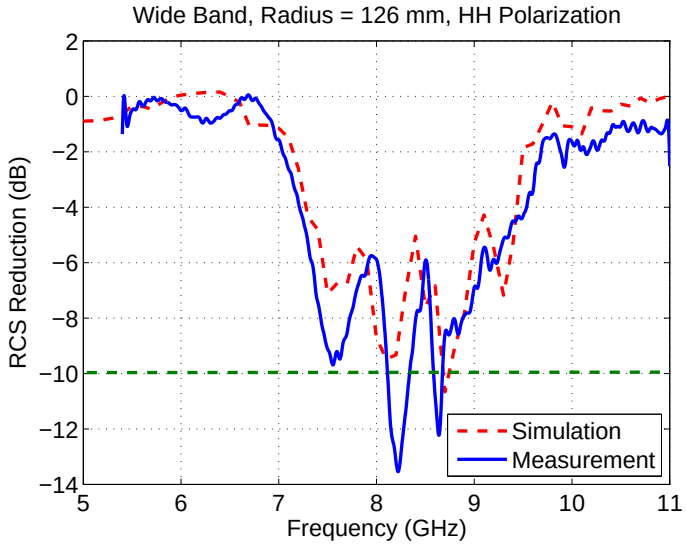

Fig. 7.27. Simulated and Measured Wide Band RCS Reduction for HH Polarization under Normal Incidence. The Radius of Curvature is 3λ.

A summary of 10-dB RCS reduction bandwidth and separation angle between the center two lobes for the wide band cylindrically curved checkerboard surface is listed in Table 7.2.

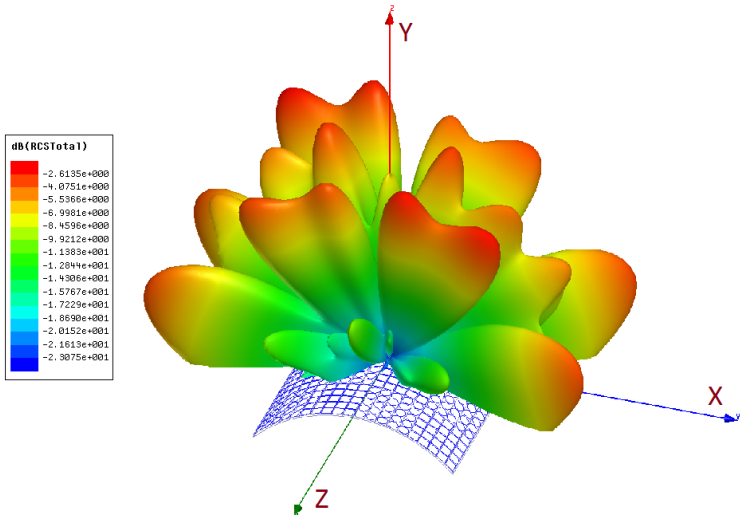

Fig. 7.28. 3-D Bistatic Simulated RCS Pattern at 8.1 GHz for HH Polarization under Normal Incidence. The Radius of Curvature is 3λ. The Separation Angle between the Center Two Lobes along the Plane of Curvature (XY Plane) is 84°.

BW / Angle	10 λ	5 λ	3 λ
Horizontal Polarization	9% / 40°	22% / 52°	0% / 84°
Vertical Polarization	9% / 40°	8% / 52°	20% / 48°

Table 7.2. Summary of Bandwidth and Separation Angle between the Center Two Lobes for the Wide Band Cylindrically Curved Checkerboard Surface.

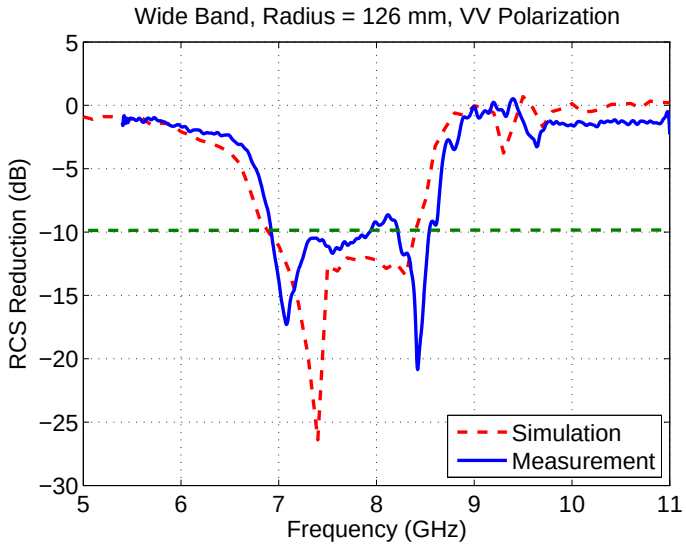

Fig. 7.29. Simulated and Measured Wide Band RCS Reduction for VV Polarization under Normal Incidence. The Radius of Curvature is 3λ.

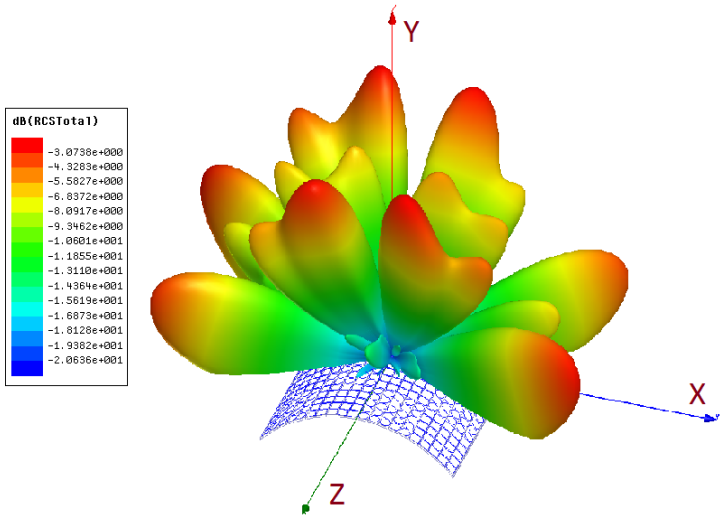

Fig. 7.30. 3-D Bistatic Simulated RCS Pattern at 8.4 GHz for VV Polarization under Normal Incidence. The Radius of Curvature is 3λ. The Separation Angle between the Center Two Lobes along the Plane of Curvature (XY Plane) is 48°.

CHAPTER 8

CONCLUSIONS

To reduce the RCS, PEC and EBG structures are combined together to build checkerboard surfaces, because they are anti-phase in terms of the reflection coefficient at the resonant frequency. Five different designs of checkerboard surfaces are analyzed, designed, simulated with HFSS and measured at the ASU EMAC facility for RCS reduction.

The first checkerboard surface is the combination of the PEC and EBG structures. The RCS reduction is generated by comparing the RCS for the checkerboard surface to the RCS for the PEC plane of the same size. In terms of the scattering fields, the main scattering beams of the square surface are re-directed toward the four quadrants, instead toward the normal direction, in order to realize the RCS reduction. The RCS reduction of 10-dB toward the broadside direction is realized in a narrow frequency band. For oblique wave incidence, the bistatic patterns illustrate that the phase of the EBG structure is dependent on the incident angle and polarization. The reflected lobe appears in the direction where a null was supposed to be. Although the EBGs with vias and without vias perform very similar, it has to be noticed that the resonant frequency is slightly shifted due to the presence/absence of the vias. Also, the presence of the vias affects the scattered fields more for oblique incidence, especially TM^z wave incidence, and increases the complexity of the fabrication. Thus, a reasonable conclusion is that the vias do not appreciably enhance the RCS reduction performance of checkerboard designs.

The second design is the combination of two different kinds of EBG structures on the same ground plane. The checkerboard surfaces, both square and hexagonal designs combining two different designs of EBG structures (EBG1 and EBG2), were designed, sim-

ulated, fabricated and measured. The main scattering beams of the square checkerboard surface are also re-directed toward the four quadrants, instead toward the normal direction. Thus, the RCS reduction of 10-dB toward broadside direction is realized over a wider frequency bandwidth of over 60%. The simulations and measurements are in excellent agreement both in terms of RCS reduction bandwidth and monostatic RCS scattering patterns. The maxima of the bistatic RCS for the hexagonal checkerboard surfaces are reduced more efficiently than that for the square design. The analytical expression of (4.2) provides a good design guideline of 10-dB RCS reduction of a dual EBG checkerboard surface compared to a corresponding PEC surface.

A dual-band checkerboard surface obtained 10-dB dual RCS reduction bandwidths of over 61% and 24% with the combination of the two different designs of dual-band EBG structures. Because the maxima of the scattered fields by the checkerboard EBG surface are re-directed toward four directions along the diagonal $\phi = 45^\circ$ and 135° planes, the RCS along the *xz* and *yz* principal planes is reduced significantly. The maxima of the bistatic RCS patterns are reduced by 5.2 dB and 5.1 dB, from those of the corresponding PEC surface, at 6.5 GHz and 5.2 GHz, respectively. Also, for the checkerboard EBG surface, the measured monostatic scattering patterns at the two frequencies along the principal *xz*, *yz* planes and diagonal $\phi = 45^\circ$, 135° planes were compared with the simulated ones for both TE^z and TM^z polarizations. Excellent agreement is obtained between measurements and simulations, in terms of monostatic RCS scattering patterns and 10-dB RCS reduction bandwidths.

Cylindrically curved checkerboard surfaces, for both narrow and wide bandwidths, were designed for three different radii of curvature. A 10-dB RCS reduction bandwidth of over 8% is obtained for the narrow band checkerboard design, while a 22% bandwidth is realized for the wide band design. While the RCS along the principal planes are reduced significantly, the principal scattered fields are re-directed toward other directions on both sides of the XY plane. For surfaces with a small curvature (e.g., 3λ), the 10-dB RCS reduction for HH polarization at the normal direction is barely achieved because of the presence and impact of AGSWs on the surface. The separation angle between the two adjacent inner most lobes along the plane of curvature (XY plane) increases as the radius of curvature becomes smaller, because the curvature is parallel to the XY plane. Due to geometrical optics, the separation angle between the two adjacent inner most lobes on either side of the XY plane is inversely proportional to the radius of curvature. A good agreement in RCS reduction is obtained between the simulations and measurements for all three (10λ, 5λ and 3λ) radii of curvature for both narrow and wide band cylindrically curved checkerboard surfaces.

Overall, according to the performance of the five different checkerboard surfaces, the most important factor is the phase difference between the two different EBG structures. It is obvious that the 180° phase difference leads to the largest RCS reduction toward the broadside direction. Secondly, the electrical size of each pattern plays a key role for the main scattering beams. The directions of the main lobes can be designed in a specific angle by adjusting the electrical size of each pattern. However, the angles of the maxima of the

main lobes are slightly shifted from the expected directions, and the minor lobes near the broadside direction may constructively add due to the effect of the finite periodicity of the checkerboard surface.

REFERENCES

[1] D. Sievenpiper, High-Impedance Electromagnetic Surfaces, Ph.D. dissertation, Department of Electrical Engineering, UCLA, 1999.

[2] D. Sievenpiper, L. Zhang, R. Broas, N. Alexópolous, and E. Yablonovitch, "High-impedance electromagnetic surfaces with a forbidden frequency band," *IEEE Trans. Microw. Theory Tech.*, vol. 47, no. 11, pp. 2059-2074, Nov. 1999.

[3] F. Yang and Y. Rahmat-Samii, "Reflection phase characterization of an electromagnetic band-gap (EBG) surface," *IEEE Antennas Propagation Soc. Int. Symp. (APSURSI)*, vol. 3, June 2002, pp. 744-747.

[4] A. Aminian, F. Yang, and Y. Rahmat-Samii, "In-phase reflection and EM wave suppression characteristics of electromagnetic band gap ground planes," *IEEE Antennas Propagation Soc. Int. Symp. (APSURSI)*, vol. 4, June 2003, pp. 430-433.

[5] C. A. Balanis, *Advanced Engineering Electromagnetics*, 2^{nd} ed., Hoboken, NJ: John Wiley & Sons, 2012.

[6] F. Yang and Y. Rahmat-Samii, "A low-profile circularly polarized curl antenna over an electromagnetic bandgap (EBG) surface," *IEEE Microw. Optical Tech. Letters*, vol. 31, no. 4, pp. 264-267, Nov. 2001.

[7] F. Yang and Y. Rahmat-Samii, "Reflection phase characterizations of the EBG ground plane for low profile wire antenna applications," *IEEE Trans. Antennas Propag.*, vol. 51, no. 10, pp. 2691-2703, Oct. 2003.

[8] F. Yang and Y. Rahmat-Samii, "Microstrip antennas integrated with electromagnetic band-gap (EBG) structures: a low mutual coupling design for array applications," *IEEE Trans. Antennas Propag.*, vol. 51, pp. 2936-2946, Oct. 2003.

[9] D. Sievenpiper, J. Schaffner, R. Loo, G. Tangonan, S. Ontiveros, and R. Harold, "A tunable impedance surface performing as a reconfigurable beam steering reflector," *IEEE Trans. Antennas Propag.*, vol. 50, no. 3, pp. 384-390, Mar. 2002.

[10] F. Terracher and G. Berginc, "Thin electromagnetic absorber using frequency selective surfaces," *IEEE Antennas Propagation Soc. Int. Symp. (APSURSI)*, vol. 2, July 2000, pp. 846-849.

[11] A. Tennant and B. Chambers, "A single-layer tuneable microwave absorber using an active FSS," *IEEE Microw. Wireless Comp. Letters*, vol. 14, no. 1, pp. 46-47, Jan. 2004.

[12] W. W. Salisbury, "Absorbent body for electromagnetic waves," US Patent 2599944, June 10, 1952.

[13] R. Fante and M. McCormack, "Reflection properties of the Salisbury screen," *IEEE Trans. Antennas Propag.*, vol. 36, no. 10, pp. 1443-1454, Oct. 1988.

[14] D. J. Kern and D. H. Werner, "A genetic algorithm approach to the design of ultra-thin electromagnetic bandgap absorbers," *IEEE Microw. Optical Tech. Letters*, vol. 38, no. 1, pp. 61-64, July 2003.

[15] S. Simms and V. Fusco, "Thin radar absorber using artificial magnetic ground plane," *Electron. Lett.*, vol. 41, no. 24, pp. 1311-1313, Nov. 2005.

[16] A. A. Abdelaziz, "A novel technique for improving the performance of Salisbury screen," *17th National Radio Science Conference*, 2000, pp. C27/1-C27/8.

[17] K. N. Rozanov, "Ultimate thickness to bandwidth ratio of radar absorbers," *IEEE Trans. Antennas Propag.*, vol. 48, no. 8, pp. 1230-1234, Aug. 2000.

[18] H. Mosallaei and Y. Rahmat-Samii, "RCS reduction of canonical targets using genetic algorithm synthesized RAM," *IEEE Trans. Antennas Propag.*, vol. 48, no. 10, pp. 1594-1606, Oct. 2000.

[19] E. F. Knott, M. T. Tuley, and J. F. Shaeffer, *Radar Cross Section*, 2nd ed., Norwood, MA, USA: Artech House, 1993.

[20] M. Paquay, J.-C. Iriarte, I. Ederra, R. Gonzalo, and P. de Maagt, "Thin AMC structure for radar cross-section reduction," *IEEE Trans. Antennas Propag.*, vol. 55, no. 12, pp. 3630-3638, Dec. 2007.

[21] A. Tellechea, J. C. Iriarte, I. Ederra, and R. Gonzalo, "Planar EBG technology chessboard configuration to reduce RCS in W band," *IEEE 7th Europ. Conf. Antennas Propag.*, Apr. 2013, pp. 3935-3938.

[22] J. C. Iriarte Galarregui, A. Tellechea Pereda, J. L. Martinez de Falcon, I. Ederra, R. Gonzalo and P. de Maagt, "Broadband radar cross-section reduction using AMC technology," *IEEE Trans. Antennas Propag.*, vol. 61, no. 12, pp. 6136-6143, Dec. 2013.

[23] Y. Zhang, R. Mittra, B. Z. Wang, and N. T. Huang, "AMCs for ultra-thin and broadband RAM design," *Electron. Lett.*, vol. 45, no. 10, pp. 484-485, May 2009.

[24] W. Chen and C.A. Balanis, "Bandwidth enhancement for RCS reduction using checkerboard EBG surfaces," *IEEE 16th Int. Symp. Antenna Tech. Appl. Electromagn. (ANTEM)*, Victoria, Canada, July 2014, pp. 1-2.

[25] W. Chen, C. A. Balanis and C. R. Birtcher "Checkerboard EBG Surfaces for Wideband Radar Cross Section Reduction," *IEEE Trans. Antennas Propag.*, vol. 63, no. 6, pp. 2636-2645, June 2015.

[26] J. C. Iriarte, I. Ederra, R. Gonzalo, and P. de Maagt, "Dual band RCS reduction using planar technology by combining AMC structures," *IEEE 3rd Europ. Conf. Antennas Propag.*, Mar. 2009, pp. 3708-3709.

[27] W. Chen, C. A. Balanis, and C. R. Birtcher, "Scattering control using square and hexagonal checkerboard surfaces," *IEEE 2015 Int. Conf. Adv. Tech. Commun. (ATC)*, Ho Chi Minh, Vietnam, Oct. 2015, pp. 358-361.

[28] W. Chen, C. A. Balanis and C. R. Birtcher "Dual Wide-Band Checkerboard Surfaces for Radar Cross Section Reduction," *IEEE Trans. Antennas Propag.*, vol. 64, no. 9, pp. 4133-4138, Sept. 2016.

[29] Y. Zhang, R. Mittra, and B. Z. Wang, "Novel design for low-RCS screens using a combination of dual-AMC," *IEEE Antennas Propagation Soc. Int. Symp. (APSURSI)*, June 2009, pp. 1-4.

[30] M. E. de Cos, Y. Alvarez, and F. Las-Heras, "RCS reduction using a combination of artificial magnetic conductors," *IEEE 5th European Conf. Antennas Propag.*, Apr. 2011, pp. 1336-1340.

[31] MKT. Al-Nuaimi, and W. Hong "Monostatic RCS reduction at mmWaves," *IEEE 2015 Asia-Pacific Microw. Conf. (APMC)*, Nanjing, China, Dec. 2015, pp. 1-2.

[32] K. He, J. Zhang, and Y. Lv, "Design of dual band low-RCS coupling slot antenna based on AMC structure," *IEEE 7th Asia-Pacific Conf. on Environment. Electromagn. (CEEM)*, Hangzhou, China, Nov. 2015, pp. 44-46.

[33] Y. Zhao, X. Cao, J. Gao, X. Yao, T. Liu, W. Li, and S. Li, "Broadband low-RCS metasurface and its application on antenna," *IEEE Trans. Antennas Propag.*, vol. 64, no. 7, pp. 2954-2962, May 2016.

[34] A. Vallecchi, J. R. De Luis, F. Capolino and F. De Flaviis, "Low profile fully planar folded dipole antenna on a high impedance surface," *IEEE Trans. Antennas Propag.*, vol. 60, no. 1, pp. 51-62, Jan. 2012.

[35] Y. Zhao, X. Cao, J. Gao, X. Yao, and X. Liu, "A low-RCS and high-gain slot antenna using broadband metasurface," *IEEE Antennas Wireless Propag. Lett.*, vol. 15, pp. 290-293, Feb. 2016.

[36] A. C. Durgun, C. A. Balanis, C. R. Birtcher and D. R. Allee, "Design, simulation, fabrication and testing of flexible bow-tie antennas," *IEEE Trans. Antennas Propag.*, vol. 59, no. 12, pp. 4425-4435, Nov. 2011.

[37] L. Yang, R. Zhang, D. Staiculescu, C. Wong, and M. Tentzeris, "A novel conformal RFID-enabled module utilizing inkjet-printed antennas and carbon nanotubes for gas-detection applications," *IEEE Antennas Wireless Propag. Lett.*, vol. 8, pp. 653-656, May 2009.

[38] S. M. Saeed, C. A. Balanis, and C. R. Birtcher, "Inkjet-printed flexible reconfigurable antenna for conformal WLAN/WiMAX wireless devices," *IEEE Antennas Wireless Propag. Lett.*, pp. 1-4, Mar. 2016.

[39] A. C. Durgun, C. A. Balanis, and C. R. Birtcher, "Reflection phase characterization of curved high impedance surface," *IEEE Trans. Antennas Propag.*, vol. 61, no. 12, pp. 6030-6038, Dec. 2013.

[40] [Online]. Available: http://www.ansys.com

[41] C. A. Balanis, *Antenna Theory: Analysis and Design*, 4^{th} ed., New York, NY, Wiley, 2016.

[42] F. Yang and Y. Rahmat-Samii, *Electromagnetic Band Gap Structures in Antenna Engineering*, Cambridge, UK: Cambridge University Press, 2009.